Ph.D. DISSERTATION

Search for Bosonic Decay Modes of a Charged Higgs Boson in Rare Top Quark Decays

탑 쿼크 희귀 붕괴에서 생성되는 하전 힉스 보존의 보존형 붕괴모드 탐색

BY

변지환

August 2023

DEPARTMENT OF PHYSICS AND ASTRONOMY
COLLEGE OF NATURAL SCIENCE
SEOUL NATIONAL UNIVERSITY

Search for Bosonic Decay Modes of a Charged Higgs Boson in Rare Top Quark Decays

탑 쿼크 희귀 붕괴에서 생성되는 하전 힉스 보존의 보존형 붕괴모드 탐색

지도교수 양 운 기

이 논문을 이학박사 학위논문으로 제출함

2023 년 8 월

서울대학교 대학원

물리천문학부

변 지 환

변지환의 이학박사 학위논문을 인준함

2023 년 8 월

위 원 장	김선기
부위원장	양운기
위 원	정성훈
위 원	최선호
위 원	원은일

Abstract

The thesis consists of a search for bosonic decay modes of charged Higgs bosons (H^+) in rare top quark decays. The analysis is based on the data of proton-proton collisions at a center-of-mass energy of 13 TeV, collected using the Compact Muon Solenoid (CMS) detector at the Large Hadron Collider (LHC) in Conseil Européen pour la Recherche Nucléaire (CERN) in 2016. The integrated luminosity of the used data corresponds to $35.9\,\mathrm{fb}^{-1}$. The analysis looks for the production of H^+ bosons in top quark pair events, the main production channel of top quarks at the LHC, to test the presence of extended Higgs sectors to the standard model of the particle physics. The H^+ boson can decay to a W and CP-odd Higgs (A) boson pair with a large branching fraction, and this decay mode is investigated using a subsequent A decay mode, $A \to \mu^+\mu^-$. Final states with electron-dimuon or trimuon, and at least two jets, including a b-tagged jet, are analyzed to search for the hypothetical process with the mass of A bosons between 15 and 75 GeV, and that of H^+ bosons between 100 and 160 GeV. No statistically significant evidence of the additional Higgs bosons was found, and the first upper limits at 95% confidence level were set on the combined branching fraction for the decay chain, $t \to bH^+ \to bW^+A \to bW^+\mu^+\mu^-$, between 1.9×10^{-6} to 8.6×10^{-6}.

Keywords: charged Higgs boson, CP-odd Higgs boson, top quark, CMS
Student Number: 2015-20329

Contents

List of Figures

List of Tables

"What is a prospector?

Seriously, what is a prospector?

It's someone who believes it's out there.

Who wakes up every morning, again and again, believing it's out there.

And then it's not? He's standing on the edge of the desert,

staring a new day's sunrise right in the eye.

He hears that little voice, a little voice that says,

'Go ahead. Keep walking.'

The sun gets higher and higher, shining down on him.

He's really hot, and he doesn't have any water to drink.

Everybody that came with him wants to turn back.

Eventually they do turn back, and there he is. And he's all alone...

with the belief that it is out there, man. It's out there.

That's a prospector."

- S. Gaghan (director), *Gold* (film) (2016).

Chapter 1

Introduction

1.1 The Standard Model and Necessity for a New Theory

The standard model (SM) of particle physics has been working as the default framework for understanding phenomena of elementary particles. It classifies the elementary particles and explains three kinds of their mutual interactions, the strong, electromagnetic, and weak interactions. The model consists of six quarks, three charged and three neutral leptons, four gauge bosons, and a Higgs boson. Having observed the Higgs boson, consistent with the SM prediction, at the LHC in 2012 [1–3], all particle constituents of the SM were experimentally confirmed. There are still a few predictions of the SM, such as trilinear Higgs couplings, that has not been examined with sufficient precision. Nonetheless, the model has been tremendously successful in description of existing experimental results, and it is often conceived as the 'laws of Newton and Maxwell' of the modern era.

Despite its triumphs in most experiments, there are also numerous observations that the SM cannot explain. Most notable examples include astronomical observations related to the matter-antimatter imbalance and dark matter, and experimental measurements on the muon magnetic dipole moment. As Sakharov pointed out, the formation of matter-antimatter imbalance requires the CP-violation [4]. The only interaction that can accommodate the CP-violation in SM is the weak interaction between the W boson and fermions, yet this contribution to the observed matter dominance of the universe is known to be negligible [5, 6]. Dark matter is another example of failures of the SM. The dark matter, originally proposed to explain velocity distributions in galaxy clusters [7], is now also supported by various different measurements as gravitational lensing [8] and cosmic microwave background (CMB) data [9]. The ever-increasing astronomical evidences reveal that only approximately 15% of matter in the universe can be explained by particles in the SM. Challenges of the SM also arose in the experiments in the precision frontiers. The anomalous magnetic dipole moment of a muon is measured in a precision of 10^{-10} at Fermilab, and have shown to differ from the expected value from the SM by 4.2 standard deviations (s.d.) [10]. These current experimental evidences strongly support the necessity for a new theory of particle physics with extended particle constituents.

Apart from the disagreement with experimental results, the SM includes structures and parameters that are either asymmetric or requiring extreme quantum corrections. These are not necessarily a problem in the sense of predictability of a model, yet it still intrigued many physicists on its origins and led them to propose alternative models resolving such features. The (gauge) hierarchy problem is an example criticizing the smallness of the Higgs mass despite its instability to quantum corrections. In supersymmetric models, the

Higgs mass is protected from large quantum corrections by the cancellation required by symmetry of the models [11, 12]. Smallness of neutrino mass is also a frequently noticed issue motivating studies on hypothetical underlying principles for the feature. Current upper limits on the neutrino mass indicate that these values are smaller than that of the rest of SM fermions by a factor less than 10^{-6} [9]. Various models extending the SM in the Higgs and lepton sectors have been proposed to provide suitable explanations for this distinctive feature of neutrino mass [13–19]. In addition to the smallness of neutrino mass, some models with larger extensions, such as the left-right symmetric models, even restores the chiral symmetry broken in the SM weak interaction [13, 20]. These hypotheses for more profound understanding of the SM structure also motivates searches for beyond-standard-model (BSM) phenomena.

1.2 Charged Higgs Bosons - Quests for the Nature of Mass

The Higgs sector of the SM consists of a single Higgs doublet, yielding a single Higgs physical state after the spontaneous symmetry breaking (SSB). The Higgs boson is responsible for the mass of all other particles, given by interaction with the Higgs boson at vacuum expected value (vev). Hitherto, the measured properties of the Higgs boson have been consistent with the SM [21]. Nevertheless, the Higgs sector larger than the SM is still a viable scenario with the current precision of experimental results [22], and it is possible that multiple Higgs bosons participate in the formation of particle mass. In addition to the precise measurement of the discovered Higgs boson, it is equally important to examine alternative Higgs models to strengthen the foundation of our understanding of mass generation.

Theories with extended Higgs sectors have been proposed for various motivations. Singlet extension can be found in models with a scalar dark matter candidate [23, 24]. Doublet extension is one of the most extensively studied scenarios. The minimal supersymmetric extension of the SM (MSSM) belongs to this category, which is motivated for the hierarchy problem and dark matter [11, 12]. Models in this category can also explain the matter-antimatter imbalance by CP-violation in Higgs sector [25, 26], small neutrino mass by either Yukawa interaction from the additional Higgs boson [27] or loop-induced generation [28], and anomalous muon magnetic moments [29]. Triplet extension arises in models of which a small Majorana mass of a left-handed (LH) neutrinos is formed by Yukawa interaction with the triplet Higgs field [15–17]. More complex scenarios are also possible [30, 31].

In this thesis, experimental investigation on charged Higgs bosons (H^+) in the context of two-Higgs-doublet models (2HDM) is discussed. The 2HDM postulates five physical Higgs states, two charged ($H^\pm$), CP-odd neutral (A), and two CP-even neutral (h, H) Higgs bosons. One of the CP-even Higgs bosons can take a role of the observed Higgs boson, and the H boson is assigned for this throughout the thesis. Charged Higgs bosons are unique scalar particles carrying electric charge, which renders its phenomenology distinguished from that of neutral Higgs bosons. The Yukawa interaction mediated by these bosons can couple quarks of different flavors, and charged and neutral leptons in the same weak doublet. This can have impacts on decay patterns of fermions, most notably a top quark. The top quarks are abundantly produced in pairs at the LHC experiment, and at the same time, it is the heaviest elementary particle observed as of now, providing powerful means of testing the Higgs sector by the large Yukawa coupling proportional to the fermion mass. In the 2HDM, a top quark can decay to a bottom quark and a H^+ boson via the Yukawa interaction,

$t \to bH^+$, and searching for the decays in top quark pair events forms one of the crucial tests for the model with a H^+ boson lighter than the top quark.

The H^+ bosons are expected to decay via either the Yukawa or weak gauge interaction within a short decay length, experimentally not discernible from the production vertex. The Yukawa interaction mediates fermionic decay modes of the boson, among which the largest partial width originates from the final state of either $c\bar{s}$, $\tau\nu$, $c\bar{b}$, or $t\bar{b}$ depending on the Higgs mass and structure of Yukawa couplings [32]. These decay modes have been investigated, using the production channels from top quark Yukawa couplings, at the LHC with the data of pp collisions at 8 and 13 TeV, and no evidence of the extended Higgs sector was found [33–42]. On the contrary, the bosonic decay modes, mediated by the weak interaction, have not yet been studied in the test of top quark decays at the LHC. The H^+ boson can decay to a W and neutral Higgs boson pair, if kinematically allowed. In the alignment limit of the 2HDM, where couplings of the H boson approach those in the SM, strongly supported by the experiment, only the unobserved neutral Higgs bosons can participate in this process as the H^+WH coupling vanishes. In particular, the H^+WA coupling is always unsuppressed and the H^+ boson can dominantly decay to a WA boson pair if the A boson lighter than the H^+ boson exists [43–46]. In order to discard the possibility of missing H^+ bosons in the previous searches because of suppressed fermionic decays, this bosonic decay mode must be studied at the LHC.

The A bosons produced in the decay chain, $t \to bH^+ \to bW^+A$, can decay to fermion pair through the Yukawa interaction, mainly either $b\bar{b}$ or $\tau^+\tau^-$ [32]. Historically, these two decay modes are considered for the study of bosonic decay modes of H^+ bosons at the LEP and Tevatron for its large rate [47–51]. Nevertheless, these soft final states are highly challenging to analyze in experiments, particularly at the LHC because of huge activity from the pile-up, additional pp

interactions in a bunch crossing. In this analysis, these difficulties are circumvented by analyzing a minor decay mode, $A \to \mu^+\mu^-$, for the first time in the bosonic decay mode of H^+ bosons. Prompt trilepton final states produced by W and A bosons evade almost entire $t\bar{t}$ backgrounds except small experimentally mis-identified cases, and they yield a clean signature in the dimuon invariant mass distribution. Despite the small branching fraction, $\mathcal{B}(A \to \mu^+\mu^-)$, the large production rate of top quarks at the LHC and the small background of the final states still makes this decay mode a valuable tool for studying the bosonic decay mode of H^+ boson.

1.3 Overview of the Thesis

The thesis discusses the first experimental investigation of the H^+ boson decaying to the WA boson pair using $A \to \mu\mu$ decays. The top quark decays, $t \to bH^+$, is considered for the H^+ production. The search is based on the data of pp collisions at $\sqrt{s} = 13\,\text{TeV}$, recorded using the CMS detector at the LHC, corresponding to an integrated luminosity of $35.9\,\text{fb}^{-1}$.

The thesis begins with theoretical backgrounds of the search and constraints from existing experimental results in Chapter 2. The Chapter 3 describes experimental details on the operation of pp collision experiments, detection systems for the final states from collisions, triggers for data-acquisition, and the luminosity measurement. Entire procedures of data-analysis is explained in the Chapter 4, including the reconstruction and identification of particles from detector signals, calibration procedures, estimation of background and signal rates, signal extraction method and related uncertainty, and final results.

Chapter 2

Phenomenological Background

2.1 Overview of the Standard Model

The SM is a relativistic quantum field theory of elementary particles based on gauge symmetries and the Higgs mechanism. The SM explains the strong, weak, and electromagnetic interactions between the particles from the gauge structure of $\mathrm{SU}(3) \times \mathrm{SU}(2)_{\mathrm{L}} \times \mathrm{U}(1)$ and provides the unified picture of electroweak interaction in the $\mathrm{SU}(2)_{\mathrm{L}} \times \mathrm{U}(1)$ group [52, 53]. Another pivot of the SM is the Higgs mechanism, also known as the Brout-Englert-Higgs mechanism [54, 55], which explains the mass of gauge bosons from the broken symmetry of the scalar field. The broken symmetry is also responsible for the fermion mass in the model. This section briefly reviews the SM of particle physics.

2.1.1 Particle Spectra in the SM

The particle spectra in the SM consists of twelve kinds of fermions and five kinds of bosons that have been confirmed by experiments. Among the fermions,

only six of them can participate in the strong interaction, and these and remaining fermions are respectively categorized as 'quarks' and 'leptons'. Three of the leptons have the same electric charge and are named as electron (e), muon (μ), and tau (τ) in the ascending order of mass values. The other three leptons called neutrinos are electrically neutral and named as electron- (ν_{e}), muon- (ν_{μ}), and tau-neutrino (ν_{τ}) depending on their main partner in the charged-current weak interaction. Three of the quarks and the others have two thirds and one third of an electron charge, respectively. The former, called up-type quarks, include top (t), charm (c), and up (u) quarks, and the latter, called down-type quarks, include bottom (b), strange (s), and down (d) quarks. The fermions with electric charge are affected by the electromagnetic interaction, and all fermions participate in the weak interaction. The fermions are grouped in pairs with their main partner in the charged-current weak interaction, and these pairs form the three generations of quarks and leptons.

The SM bosons are comprised of four kinds of spin-1 and one kind of spin-0 bosons. The spin-1 bosons arise from the gauge symmetries of the interaction which they are responsible for. The photon and gluon are massless particles which mediate electromagnetic and strong interactions, respectively. The $\mathrm{W}^{\pm}$ and Z bosons are massive particles, of which the mass values are 80.38 and 91.188 GeV, and they mediate the weak interaction. The Higgs boson is the only spin-0 particle in the SM and yield non-zero vev field responsible for mass of gauge bosons and fermions. The scalar boson also mediates the Yukawa interaction. The particles of the SM are summarized in the Table 2.1

2.1.2 Gauge Symmetries in the SM

In the SM, the strong, weak, and electromagnetic interactions occurs in a way preserving the symmetry they represent. More specifically, the Lagrangian

Table 2.1: Summary of SM particles and their properties

Fermions (spin-1/2)							
Category	Generation	Particle	Charge (q_e)	Mass (GeV)	strong	EM	weak
Lepton	First	e	-1	0.000511	-	✓	✓
		ν_{e}	0	$\simeq 0$	-	-	✓
	Second	μ	-1	0.106	-	✓	✓
		ν_{μ}	0	$\simeq 0$	-	-	✓
	Third	τ	-1	1.78	-	✓	✓
		ν_{τ}	0	$\simeq 0$	-	-	✓
Quark	First	u	2/3	0.00216	✓	✓	✓
		d	-1/3	0.00467	✓	✓	✓
	Second	c	2/3	1.27	✓	✓	✓
		s	-1/3	0.093	✓	✓	✓
	Third	t	2/3	173	✓	✓	✓
		b	-1/3	4.18	✓	✓	✓

Bosons					
Category	Spin	Particle	Charge (q_e)	Mass (GeV)	Mediating interaction
Gauge boson	1	γ	0	0	electromagnetic
		g	0	0	strong
		W	1	80.4	weak
		Z	0	91.2	weak
Higgs boson	0	H	0	125	Yukawa

of the model should be invariant under the local gauge transformation,

$$\psi(x) \rightarrow \psi'(x) = \exp[ic\alpha_a(x)\mathrm{T}_a]\psi(x), \tag{2.1}$$

where ψ and $\alpha_a(x)$ are fields of a particle and phases, and T_a are the generators of the symmetry. This can be achieved by replacing space-time derivatives in free particle Lagrangians to covariant derivatives, casting the kinetic term of spin-1 bosons in terms of covariant derivative, and requiring the transformation rule for gauge boson field to cancel the phase shifts,

$$\begin{aligned}
\partial^\mu &\rightarrow D^\mu = \partial^\mu + igV_a^\mu T_a \\
V_a^\mu &\rightarrow V_a^{'\mu} = V_a^\mu - \partial^\mu\alpha_a - gf_{aij}\alpha_j V_j^\mu, \\
-\frac{1}{4}F^{\mu\nu}F_{\mu\nu} &\rightarrow -\frac{1}{4ig}[D^\mu, D^\nu] = -\frac{1}{4}V_a^{\mu\nu}V_{a,\mu\nu}, \\
\text{where } V_a^{\mu\nu} &\equiv \partial^\mu V_a^\nu - \partial^\nu V_a^\mu - gf_{abc}V_b^\mu V_c^\nu.
\end{aligned} \tag{2.2}$$

Here, the V_a^μ is the vector field conserving the local gauge symmetry, and f_{abc} is the structure constant for the symmetry group. The terms with f_{abc} is absent for the U(1) group.

The symmetry group of the strong interaction is SU(3). The symmetry group has eight generators, representable with the eight Gell-Mann matrices, hence eight gluon fields mediate the strong interaction. Each quark exists in three orthogonal states of the group, referred to as the r, g, and b color-charges of the strong interaction. The coupling constant of the strong interaction is close to unity at low energy but decreases to approximately $g_s^2/4\pi = 0.118$ at $q^2 \sim m_Z^2$, permitting perturbative calculations in high energy experiments.

The electromagnetic and weak interactions originate from the same symmetry group, $\mathrm{SU_L}(2)\times\mathrm{U}(1)$. The subscript L in the SU(2) group is written to

imply that this symmetry applies only to left-handed chiral field of the fermions, $\psi_L = \frac{1}{2}(1-\gamma^5)\psi$. The chiral components of fermion fields are basically mathematical entities, yet it converges to helicity eigenstates in the relativistic limit and allows comprehension in terms of kinematic quantities. The SU(2) group has three generators, the Pauli matrices, hence three gauge fields associated with those, W_a for σ_a (a=1–3), arise from this group. The U(1) group yields one gauge boson, B, from a single generator. The physical states of gauge fields of electroweak interaction emerge as a mixture of these fields,

$$\begin{aligned} \mathrm{W}^{\pm} &= \frac{1}{\sqrt{2}}(W_1 \mp W_2), \\ \mathrm{Z} &= \cos(\theta_{\mathrm{W}})W_3 - \sin(\theta_{\mathrm{W}})B, \\ \gamma &= \sin(\theta_{\mathrm{W}})W_3 + \cos(\theta_{\mathrm{W}})B. \end{aligned} \tag{2.3}$$

The θ_{W} is a parameter named as the Weinberg angle, representing the magnitude of mixture of two original gauge fields in the physical states. Due to the composition, the W fields affect only the LH chiral component, while Z and γ fields act on both chiral components. The conserved quantities of this symmetry group are weak isospin (I_{W}), its third component (I^3_{W}), and hypercharge (Y). The latter two quantum numbers are conventionally used to distinguish field properties, and for simplicity, the third component will be referred to as the weak isospin in this thesis unless otherwise mentioned.

Although the electromagnetism is a portion of electroweak interaction, the interaction between fermions and a photon can be cast as an interaction in $\mathrm{U_{em}}(1)$ gauge group. In this picture, the photon is the sole gauge field of the symmetry group, and the conserved quantity of the group is the electric charge (Q). As the electric charge is related to the weak isospin and hypercharge as $Q = I^3_{\mathrm{W}} + \mathrm{Y}/2$, it is still the conserved quantity in the global symmetry group. In

addition, the electromagnetic interaction is the predominant one in a sufficiently long range, and it can be related to low-energy high-precision measurements and common experiences. Therefore the electric charge remains as the important quantum number distinguishing elementary particles after the unification of weak and electromagnetic interactions.

The coupling strengths of the electroweak gauge bosons to the fermions are related as $g_\gamma = g_{\mathrm{W}}\sin\theta_{\mathrm{W}} = g_{\mathrm{Z}}\cos\theta_{\mathrm{Z}} = q_e$. The observed value of the Weinberg angle is approximately 30°, implying that the coupling strength is similar for all electroweak gauge bosons and weakest for the electromagnetic interaction. The suppression of weak interaction in low energy experiments originate purely from the propagator $(q^2 - m_V^2)^{-1} \sim m_V^{-2}$ in the calculation of transition probability.

The summary of charges of particles in each gauge group are summarized in the Table 2.2.

2.1.3 Origin of Mass in the SM

Mass terms of gauge bosons and fermions in the SM originate from the interaction with the vev of the Higgs field. This can be achieved only when the shape of the Higgs field potential develops minima at non-zero field value. In the SM, the potential of the Higgs field is assumed to be a quartic function.

$$V(\phi) \ = \mu^2\phi^\dagger\phi + \lambda(\phi^\dagger\phi)^2 \quad \text{with} \quad \phi = \begin{pmatrix} \phi^+ \\ \phi^0 \end{pmatrix} = \frac{1}{\sqrt{2}} \begin{pmatrix} \phi_1 + i\phi_2 \\ \phi_3 + i\phi_4 \end{pmatrix} \tag{2.4}$$

The coefficient μ^2 is required to be negative to develop non-zero vev. In order to respect the electric charge conservation, the vev should not exist for upper component of the doublet. Thus the Higgs doublet can be expanded around the

Table 2.2: Summary of charges of particles in each gauge symmetries of the SM. The subscripts L and R represent LH and RH chiral components of fermions.

Fermions (spin-1/2)						
Particle	SU(3)	EM (q_e)	$I^3_{\mathrm{W},L}$	$I^3_{\mathrm{W},R}$	Y_L	Y_R
neutrinos (ν_e, ν_μ, ν_τ)	singlet	0	1/2	0	-1	0
charged leptons (e, μ, τ)	singlet	-1	-1/2	0	-1	-2
up-type quarks (u, c, t)	triplet	2/3	1/2	0	1/3	4/3
down-type quarks(d, s, b)	triplet	-1/3	-1/2	0	1/3	-2/3
Bosons						
Particle	SU(3)	EM (q_e)	I^3_W		Y	
γ	singlet	0	0		0	
g	octet	0	0		0	
$\mathrm{W}^\pm$	singlet	±1	±1		0	
Z	singlet	0	0		0	
H	singlet	0	-1/2		1	

vev (v) of the neutral component.

$$\phi = \frac{1}{\sqrt{2}} \begin{pmatrix} \phi_1 + i\phi_2 \\ v + h + i\phi_4 \end{pmatrix} \tag{2.5}$$

Then the vev component of the gauge interaction terms for the Higgs field yields the following quadratic terms of the gauge fields, resulting in the mass terms of gauge bosons.

$$\begin{aligned} \mathcal{L}_{\mathrm{H}} &= (D^\mu \phi)^\dagger (D_\mu \phi) - V(\phi) \\ &= |(\frac{ig_{\mathrm{W}}}{2}\sigma_a \mathrm{W}_a^\mu + \frac{ig'}{2}B^\mu) \begin{pmatrix} 0 \\ v/\sqrt{2} \end{pmatrix}|^2 + ... \\ &= \frac{g_{\mathrm{W}}^2 v^2}{8}[\mathrm{W}_1^2 + \mathrm{W}_2^2 + (\frac{g'}{g_{\mathrm{W}}}B - \mathrm{W}_3)^2] + ... \\ &= \frac{g_{\mathrm{W}}^2 v^2}{8}(\mathrm{W}^+)^2 + \frac{g_{\mathrm{W}}^2 v^2}{8}(\mathrm{W}^-)^2 + \frac{g_{\mathrm{W}}^2 + g'^2}{8}\mathrm{Z}^2 + ... \\ &= \frac{1}{2}m_{\mathrm{W}^+}^2(\mathrm{W}^+)^2 + \frac{1}{2}m_{\mathrm{W}^-}^2(\mathrm{W}^-)^2 + \frac{1}{2}m_{\mathrm{Z}}^2\mathrm{Z}^2 + ... \end{aligned} \tag{2.6}$$

Therefore the gauge boson mass in the SM is related to fundamental parameters of weak couplings, vev, and Weinberg angle as,

$$m_{\mathrm{W}} = \frac{1}{2}gv \text{ and } m_{\mathrm{Z}} = \frac{gv}{2\cos\theta_{\mathrm{W}}}. \tag{2.7}$$

On the other hand, the fermion mass in the SM arises from the Yukawa interaction between the fermions and Higgs boson, given as,

$$\mathcal{L}_{Yukawa} = -Y_{u,ij}\overline{Q}_{L,i}\widetilde{\phi}u_{R,j} - Y_{d,ij}\overline{Q}_{L,i}\phi d_{R,j} + h.c.. \tag{2.8}$$

Here, $Q_{L,i}^T = (\ u_{L,i}\ \ d_{L,i}\ )$ is the weak doublet of LH chiral fermions in the i-th generation, $u_{R,j}$ and $d_{R,j}$ are the RH chiral fields corresponding to LH fermions

in j-th generation with the weak isospin value of 1/2 and -1/2. The $Y_{u,ij}$ and $Y_{d,ij}$ are Yukawa couplings for the combination of fermions, and the conjugate doublet $\widetilde{\phi}$ is defined as $i\sigma_2\phi^*$. From the expansion around the vacuum, the Yukawa interaction terms from Higgs vev field yields,

$$\begin{aligned}\mathcal{L}_{Yukawa} &= -\frac{v}{\sqrt{2}}Y_{u,ij}\overline{u}_{L,i}u_{R,j} - \frac{v}{\sqrt{2}}Y_{d,ij}\overline{d}_{L,i}d_{R,j} + h.c. + ... \\ &= -\frac{v}{\sqrt{2}}(\overline{d}_L Y_d d_R + \overline{u}_L Y_u u_R) + h.c. + ...\end{aligned} \tag{2.9}$$

The last line is formulated in matrices. As the $YY^\dagger$ is Hermitian, the Y can be diagonalized using unitary matrices U and K, which changes the basis for LH and RH fermions. Then the Yukawa interactions can be reformulated to yield the mass terms of fermion Lagrangian,

$$\begin{aligned}\mathcal{L}_{Yukawa} &= -\frac{v}{\sqrt{2}}(\overline{d}_L U_d M_d K_d^\dagger d_R + \overline{u}_L U_u M_u K_u^\dagger u_R) + h.c. + ... \\ &= -\frac{v}{\sqrt{2}}(M_{d,ii}\overline{d'}_{L,i}d'_{R,i} + M_{u,ii}\overline{u'}_{L,i}u'_{R,i}) + h.c. + ... \\ &= -\frac{v}{\sqrt{2}}(M_{d,ii}\overline{d'}_i d'_i + M_{u,ii}\overline{u'}_i u'_i) + ... \\ &= -m_{d,i}\overline{d'}_i d'_i - m_{u,i}\overline{u'}_i u'_i + ...\end{aligned} \tag{2.10}$$

The d' and u' are the mass eigenstates obtained from the unitary transformation of d and u by the matrices U and K, and the $m_{d,i}$ and $m_{u,i}$ corresponds to the mass of i-th generation fermions with the weak isospin -1/2 and 1/2.

The difference between the mass and flavor eigenstates can be observed in the charged-current weak interaction, which requires two different U matrices from the down- and up-type fermions connected at the same vertex. Reformulating the charged-current weak interaction in the SM Lagrangian with the mass-basis yields,

$$
\begin{aligned}
\mathcal{L}_{Wff} &= \frac{g_{\rm W}}{\sqrt{2}}(\mathrm{W}^{+}{}_{\mu}\overline{u}_{L,i}\gamma^{\mu}d_{L,i} + \mathrm{W}^{-}{}_{\mu}\overline{d}_{L,i}\gamma^{\mu}u_{L,i}) \\
&= \frac{g_{\rm W}}{\sqrt{2}}(\mathrm{W}^{+}{}_{\mu}\overline{u'}_{L,j}\gamma^{\mu}U^{\dagger}_{u,ji}U_{d,ik}d'_{L,k} + \mathrm{W}^{-}{}_{\mu}\overline{d'}_{L,j}\gamma^{\mu}U^{\dagger}_{d,ji}U_{u,ik}u'_{L,k}) \quad (2.11) \\
&= \frac{g_{\rm W}}{\sqrt{2}}(\mathrm{W}^{+}{}_{\mu}\overline{u'}_{L,i}\gamma^{\mu}V_{ij}d'_{L,j} + \mathrm{W}^{-}{}_{\mu}\overline{d'}_{L,i}\gamma^{\mu}V^{\dagger}_{ij}u'_{L,j}).
\end{aligned}
$$

The matrix V, defined as $U_u^{\dagger}U_d$, is referred to as the Cabibbo-Kobayashi-Maskawa (CKM) matrix for quarks. In case of leptons, the complex conjugate $U_d^{\dagger}U_u$, called as Pontecorvo–Maki–Nakagawa–Sakata (PMNS) matrix, is conventionally used. These matrices can be parameterized as,

$$
V = \begin{pmatrix} 1 & 0 & 0 \\ 0 & c_{23} & s_{23} \\ 0 & -s_{23} & c_{23} \end{pmatrix}
\begin{pmatrix} c_{13} & 0 & s_{13}e^{-i\delta} \\ 0 & 1 & 0 \\ -s_{13}e^{i\delta} & 0 & c_{13} \end{pmatrix}
\begin{pmatrix} c_{12} & s_{12} & 0 \\ -s_{12} & c_{12} & 0 \\ 0 & 0 & 1 \end{pmatrix}, \quad (2.12)
$$

where c_{ij} and s_{ij} are abbreviation of $\cos(\theta_{ij})$ and $\sin(\theta_{ij})$. The measured value of these parameters in the CKM [56] and PMNS matrices [57] are,

$$
\begin{aligned}
s_{12} = 0.22500 \pm 0.00067,\ s_{13} = 0.00369 \pm 0.00011,\ s_{23} = 0.04182^{+0.00085}_{-0.00074}, \\
\text{and } \delta(rad) = 1.144 \pm 0.027 \text{ (CKM)}, \\
\theta_{12}(^\circ) = 33.44^{+0.77}_{-0.74},\ \theta_{13}(^\circ) = 8.57 \pm 0.12,\ \theta_{23}(^\circ) = 49.2^{+0.9}_{-1.2}, \\
\text{and } \delta(^\circ) = 197^{+27}_{-24} \text{ (PMNS, } (m_{\nu_1} < m_{\nu_2} < m_{\nu_3})), \\
\theta_{12}(^\circ) = 33.45^{+0.78}_{-0.75},\ \theta_{13}(^\circ) = 8.60 \pm 0.12,\ \theta_{23}(^\circ) = 49.3^{+0.9}_{-1.1}, \\
\text{and } \delta(^\circ) = 282^{+26}_{-30} \text{ (PMNS, } (m_{\nu_3} < m_{\nu_1} < m_{\nu_2})).
\end{aligned}
$$

Note that, at the time of writing, the order of neutrino mass eigenstate is not known, and extracted parameters can be different depending on the neutrino

mass hierarchy. In addition, the range of complex phase δ in the PMNS matrix in 3 s.d. include the null phase, hence the it has not yet been conclusively determined if the PMNS matrix is complex.

The non-diagonal form of observed CKM and PMNS matrices confirms the difference between the two basis choices for both leptons and quarks, and it would manifest as the unconserved fermion generations in the charged-current weak interaction. In addition, the observed complex phase of CKM matrix reveals that there is a phase difference between the Yukawa and weak interactions, and this cause the violation of CP-symmetry in the charged-current weak interaction, experimentally confirmed in K and B meson decays [56]. The phase difference between the Yukawa and charged-current weak interaction is the sole source of CP-violation in the SM.

The aforementioned couplings between Higgs boson and other SM particles responsible for the mass generation can be tested using processes that involve the first order terms of neutral Higgs component. Those terms in the SM Lagrangian are given as,

$$\begin{aligned} \mathcal{L}_{\mathrm{H},h} &= \frac{m_{\mathrm{W}}^2}{2v} h(\mathrm{W}^+)^2 + \frac{m_{\mathrm{W}}^2}{2v} h(\mathrm{W}^-)^2 + \frac{m_{\mathrm{Z}}^2}{2v} h\mathrm{Z}^2 \\ \mathcal{L}_{Yukawa,h} &= -\frac{m_{d,i}}{v} h\overline{d'}_i d'_i - \frac{m_{u,i}}{v} h\overline{u'}_i u'_i. \end{aligned} \tag{2.13}$$

These terms contribute to the production rate of Higgs boson from $VV \to \mathrm{H}$, $q\overline{q'} \to V\mathrm{H}$, $\mathrm{gg} \to \mathrm{t\bar{t}H}$, or $\mathrm{gg} \to \mathrm{H}$ at 1-loop level, and its decay rate in $\mathrm{H} \to VV$, $\mathrm{H} \to f\overline{f'}$, and $\mathrm{H} \to \gamma\gamma$ via 1-loop involving these couplings. Global analysis of these production and decay modes at the LHC shows that these couplings for gauge bosons, fermions of the third generation, and the muon are in good agreement with the SM prediction as can be seen in Fig 2.1.

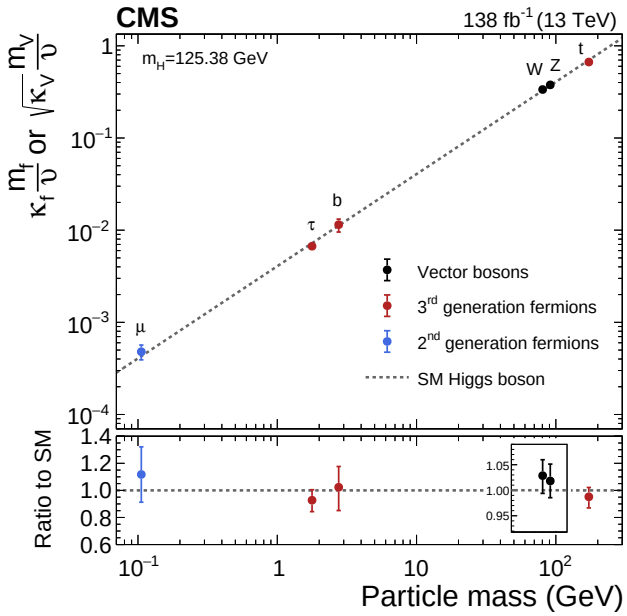

Figure 2.1: The observed couplings of the Higgs boson with gauge bosons, muon, and third-generation fermions from the CMS Collaboration [21]. The κ is defined as the ratio of the observed coupling and the SM expectation.

2.2 Phenomenology of 2HDM

As discussed in the previous section, the SM postulates the generation of particle mass from vev component of Higgs field in the gauge and Yukawa interactions, originating from a single Higgs doublet, and its prediction has been consistent with the experiments. Nevertheless, an enlarged Higgs sector can also be a perfectly viable scenario with measurements on properties of the observed Higgs boson, and multiple Higgs bosons could have formed vev contributing to particle mass. Instead, the extended Higgs models also anticipate phenomena that cannot occur in the SM. The 2HDM is a good example of such scenarios. In this section, a review of 2HDM relevant to the subject of thesis will be discussed.

2.2.1 Scalar Potentials and the Higgs Spectrum

The Higgs sector of 2HDM consists of two $\mathrm{SU(2)_L}$ doublets with the same hypercharge, $Y = 1$, in the same gauge symmetry with the SM. The scalar potential of general 2HDM is structured as [58],

$$\begin{aligned} V = {} & m_{11}^2\Phi_1^\dagger\Phi_1 + m_{22}^2\Phi_2^\dagger\Phi_2 - (m_{12}^2\Phi_1^\dagger\Phi_2 + m_{12}^{*2}\Phi_2^\dagger\Phi_1) + \frac{\lambda_1}{2}(\Phi_1^\dagger\Phi_1)^2 + \frac{\lambda_2}{2}(\Phi_2^\dagger\Phi_2)^2 \\ & + \lambda_3\Phi_1^\dagger\Phi_1\Phi_2^\dagger\Phi_2 + \lambda_4\Phi_1^\dagger\Phi_2\Phi_2^\dagger\Phi_1 + \frac{1}{2}[\lambda_5(\Phi_1^\dagger\Phi_2)^2 + \lambda_5^*(\Phi_2^\dagger\Phi_1)^2] \\ & + \Phi_1^\dagger\Phi_1(\lambda_6\Phi_1^\dagger\Phi_2 + \lambda_6^*\Phi_2^\dagger\Phi_1) + \Phi_2^\dagger\Phi_2(\lambda_7\Phi_1^\dagger\Phi_2 + \lambda_7^*\Phi_2^\dagger\Phi_1), \qquad (2.14) \\ & \text{with } \Phi_i = \begin{pmatrix} \phi_a^+ \\ (v_a + \rho_a + i\eta_a)/\sqrt{2} \end{pmatrix}, \ a = 1, 2. \end{aligned}$$

Here, the v_a is the vev of the a-th doublet, ρ, η are real fields, and parameters m_{ii}, λ_{1-4} are real. As the Yukawa interaction of two doublets need not be simultaneously diagonalized, the general 2HDM can exhibit tree-level flavor-changing

neutral currents (FCNC) mediated by neutral Higgs states of the model. In addition, the scalar potential of the 2HDM contains complex terms, those with m_{12}^2 and λ_{5-7}, which can explicitly break the CP-symmetry. Even if the CP-symmetry is respected in the Higgs potential, it is possible that phase difference in vevs from two doublets after SSB cause complex Yukawa interaction violating CP-symmetry. These features of the 2HDM can affect the decay patterns and mass splittings of neutral mesons, measured in high precision, hence retains strong constraints from the experiments [59]. The latter feature also receives constraints from the measured values of CKM matrix elements [60]. Despite the interesting features of the 2HDM, the subject of the thesis does not require such behaviors of the model, only the parameter regions of 2HDM where these features are absent is considered.

The CP-conserving 2HDM with a Z_2 symmetry is a frequently studied example scenario. The Z_2 transformation changes sign of the field depending on the Z_2 charge, and the symmetry allows only the specific types of Yukawa couplings that will prevent FCNC. The Z_2 charge of fermions and Higgs bosons are summarized in the Table 2.3. Note that the mass and RH chiral fields of neutrinos are ignored in the analysis of 2HDM, as they barely have visible impacts on the collider phenomenology.

Table 2.3: Summary of Z_2 charges of particles in the model

	Φ_1	Φ_2	u_R	d_R	ℓ_R	Q_L, L_L
Type-1	+	-	-	-	-	+
Type-2	+	-	-	+	+	+
Type-X	+	-	-	-	+	+
Type-Y	+	-	-	+	-	+

The Z_2 symmetry requires absence of quartic terms with λ_{6-7} and the quadratic term with m_{12}^2, hence λ_{6-7} is considered to be zero. However, with keeping the Yukawa interactions determined from Z_2 symmetry, the m_{12}^2 term is often included in the Lagrangian for the parameter region consistent with experiments, as it significantly relaxes the theoretical bounds on scalar masses from unitarity limits [58, 61]. Such a model is referred to as the 2HDM with a softly broken Z_2 symmetry, and this term will be considered in this section.

In the remaining terms of the scalar potential, the CP conservation requires m_{12}^2 and λ_5 to be real. Hence the scalar potential considered in this thesis includes only the real parameters and will be written as,

$$\begin{aligned} V \ &= m_{11}^2\Phi_1^\dagger\Phi_1 + m_{22}^2\Phi_2^\dagger\Phi_2 - m_{12}^2(\Phi_1^\dagger\Phi_2 + \Phi_2^\dagger\Phi_1) + \frac{\lambda_1}{2}(\Phi_1^\dagger\Phi_1)^2 + \frac{\lambda_2}{2}(\Phi_2^\dagger\Phi_2)^2 \\ &+ \lambda_3\Phi_1^\dagger\Phi_1\Phi_2^\dagger\Phi_2 + \lambda_4\Phi_1^\dagger\Phi_2\Phi_2^\dagger\Phi_1 + \frac{\lambda_5}{2}[(\Phi_1^\dagger\Phi_2)^2 + (\Phi_2^\dagger\Phi_1)^2]. \end{aligned} \tag{2.15}$$

The two doublets in Eq. 2.14 have eight degrees of freedom, three of which will be reduced to give mass to $W^\pm$ and Z bosons after SSB, hence there will be five Higgs physical states. The Higgs states consists of two charged $H^\pm$, two CP-even (h, H), and a CP-odd (A) scalars.

It is useful to identify the relationship between the physical states and the two doublets in the current basis for Z_2 symmetry. The two doublet can be represented in the Higgs basis, where only one of the doublet has vev. In the basis choice, the component of the doublet corresponds to Goldstone bosons and physical Higgs states,

$$\Phi_1 \ = \ \begin{pmatrix} G^+ \\ (v + \mathrm{H} + iG_0)/\sqrt{2} \end{pmatrix}, \ \Phi_2 = \ \begin{pmatrix} \mathrm{H}^+ \\ (\mathrm{h} + i\mathrm{A})/\sqrt{2} \end{pmatrix}. \tag{2.16}$$

Here, the G^+ and G_0 are Goldstone bosons to be absorbed to gauge bosons.

The component of the doublets in the two bases are related as,

$$\begin{pmatrix} G^+ \\ \mathrm{H}^+ \end{pmatrix} = \begin{pmatrix} \cos\beta & \sin\beta \\ -\sin\beta & \cos\beta \end{pmatrix} \begin{pmatrix} \phi_1^+ \\ \phi_2^+ \end{pmatrix}, \quad \begin{pmatrix} G_0 \\ \mathrm{A} \end{pmatrix} = \begin{pmatrix} \cos\beta & \sin\beta \\ -\sin\beta & \cos\beta \end{pmatrix} \begin{pmatrix} \eta_1 \\ \eta_2 \end{pmatrix},$$
$$\begin{pmatrix} \mathrm{H} \\ \mathrm{h} \end{pmatrix} = \begin{pmatrix} \cos\alpha & \sin\alpha \\ -\sin\alpha & \cos\alpha \end{pmatrix} \begin{pmatrix} \rho_1 \\ \rho_2 \end{pmatrix}, \qquad \text{with} \quad \tan\beta = \frac{v_2}{v_1} \tag{2.17}$$

Hence, the relationship between the doublets in two bases are described by two Higgs mixing angles, α and β.

The mass of physical Higgs states are determined from a curvature of the scalar potential with local extremum conditions at vev,

$$\begin{aligned}
\frac{\partial V}{\partial v_1} =& 0 \;\rightarrow\; m_{11}^2 = m_{12}^2 \tan\beta - \frac{v^2}{2}(\lambda_1 \cos^2\beta + \lambda_{345}\sin^2\beta) \\
\frac{\partial V}{\partial v_2} =& 0 \;\rightarrow\; m_{22}^2 = m_{12}^2 \cot\beta - \frac{v^2}{2}(\lambda_2 \sin^2\beta + \lambda_{345}\cos^2\beta) \\
[m_{\mathrm{H}^+}^2]_{ij} =& \frac{\partial^2 V}{\partial\phi_i^+ \partial\phi_j^-} = (m_{12}^2 - \frac{v^2}{2}(\lambda_4+\lambda_5)\cos\beta\sin\beta) \begin{pmatrix} \tan\beta & -1 \\ -1 & \cot\beta \end{pmatrix} \\
[m_{\mathrm{A}}^2]_{ij} =& \frac{\partial^2 V}{\partial\eta_i \partial\eta_j} = (m_{12}^2 - v^2\lambda_5\cos\beta\sin\beta) \begin{pmatrix} \tan\beta & -1 \\ -1 & \cot\beta \end{pmatrix} \\
[m_{\mathrm{h,H}}^2]_{ij} =& \frac{\partial^2 V}{\partial\rho_i \partial\rho_j} = \begin{pmatrix} m_{12}^2\tan\beta + v^2\lambda_1\cos^2\beta & -m_{12}^2 + v^2\lambda_{345}\sin\beta\cos\beta \\ -m_{12}^2 + v^2\lambda_{345}\sin\beta\cos\beta & m_{12}^2\cot\beta + v^2\lambda_2\sin^2\beta \end{pmatrix},
\end{aligned} \tag{2.18}$$

with $\lambda_{345} \equiv \lambda_3 + \lambda_4 + \lambda_5$

The non-zero eigenvalues of the matrices correspond to the mass of the five scalars. In case of the $\mathrm{H}^+$and A bosons, the mass values are expressed in rather simpler function of the potential parameters,

$$m_{\rm A}^2 = \frac{m_{12}^2}{\cos\beta\sin\beta} - \lambda_5 v^2 \tag{2.19}$$
$$m_{\rm H^+}^2 = \frac{m_{12}^2}{\cos\beta\sin\beta} - \frac{v^2}{2}(\lambda_4+\lambda_5) = m_{\rm A}^2 + \frac{v^2}{2}(\lambda_5-\lambda_4)$$

It is worth to mention the important difference between the MSSM and general 2HDM with a softly broken Z_2 symmetry. The Higgs sector of MSSM consists of two Higgs doublets, and the structure of Yukawa interaction of MSSM is identical to that of the latter model with type-2 Z_2 charges. However, the scalar potential of MSSM is much more restricted compared to the general 2HDM, as it requires conditions [62],

$$\lambda_1 = \lambda_2 = \frac{g_{\rm W}^2 + g'^2}{4}, \quad \lambda_3 = \frac{g_{\rm W}^2 - g'^2}{4}, \quad \lambda_4 = -\frac{g_{\rm W}^2}{2}, \quad \lambda_{5-7} = 0. \tag{2.20}$$

Then the $m_{\rm H^+}$ in Eq.2.19 becomes,

$$m_{\rm H^+}^2 = m_{\rm A}^2 + \frac{1}{4} g_{\rm W}^2 v^2 = m_{\rm A}^2 + m_{\rm W}^2. \tag{2.21}$$

Therefore, the targeted bosonic decay mode of the $\rm H^+$ boson, $\rm H^+ \to W^+ A$, can never occur on-shell at tree-level, and the decay rate is always suppressed in the MSSM. Besides, CP-even Higgs mass in the MSSM is expected to be similar to the $m_{\rm A}$ as can be seen from the trace of CP-even mass matrix in Eq. 2.18,

$$m_{\rm h}^2 + m_{\rm H}^2 = tr[m_{\rm h,H}^2] = \frac{m_{12}^2}{\cos\beta\sin\beta} + v^2\lambda_1 = m_{\rm A}^2 + m_{\rm Z}^2. \tag{2.22}$$

As the observed Higgs mass of 125 GeV is similar to $m_{\rm Z}$, the mass of all unobserved Higgs bosons in the MSSM is typically expected to be similar. Hence, bosonic decay modes of the $\rm H^+$ boson in the MSSM is in general implausible. Such a feature is only because of its unique shape of scalar potential, and the

bosonic decay is unsuppressed in general 2HDM [45, 46] or supersymmetric models with the Higgs sector larger than the 2HDM [43, 44].

2.2.2 Yukawa Interactions in the 2HDM

The Yukawa interaction of 2HDM with the Z_2 symmetry can be written as,

$$\mathcal{L}_{yukawa}^{2HDM} = -Y_{u,ij}\overline{Q}_{L,i}\widetilde{\Phi}_u u_{R,j} - Y_{d,ij}\overline{Q}_{L,i}\Phi_d d_{R,j} - Y_{\ell,ij}\overline{L}_{L,i}\Phi_\ell \ell_{R,j} + h.c.. \quad (2.23)$$

The Q_L and L_L are weak doublets of quarks and leptons, $\Phi_{u,d,\ell}$ are either Φ_1 or Φ_2, and the subscript i and j represents the generation of fermions. From the functional form of the Lagrangian, it is obvious that the tree-level FCNC Yukawa interaction is absent, as each fermion obtains its mass from a single doublet. The Z_2 symmetry and corresponding charges in Table 2.3 permit only the assignments with same Z_2 charges of a Higgs doublet and a RH fermion field. Hence, the $\Phi_{u,d,\ell}$ can be summarized as the Table 2.4.

Table 2.4: Higgs couplings to RH chiral fields in 2HDM

	Type-1	Type-2	Type-X	Type-Y
Φ_u	Φ_2	Φ_2	Φ_2	Φ_2
Φ_d	Φ_2	Φ_1	Φ_2	Φ_1
Φ_ℓ	Φ_2	Φ_1	Φ_1	Φ_2

Using the basis change in Eq. 2.17 and expanding the component Higgs field in Eq. 2.23, the Lagrangian of Yukawa interaction excluding the mass terms after SSB are written in terms of physical Higgs states as [32],

$$\mathcal{L}^{2HDM}_{yukawa} = -\sum_{f=u,d,\ell}\left(\frac{m_f}{v}\xi_{\mathrm{h},f}\bar{f}f\mathrm{h} + \frac{m_f}{v}\xi_{\mathrm{H},f}\bar{f}f\mathrm{H} - i\frac{m_f}{v}\xi_{\mathrm{A},f}\bar{f}\gamma_5 f\mathrm{A}\right) \tag{2.24}$$
$$-\left[\frac{\sqrt{2}V_{ud}}{v}\overline{u}(m_u\xi_{\mathrm{A},u}P_L + m_d\xi_{\mathrm{A},d}P_R)d\mathrm{H}^+ + \frac{\sqrt{2}m_\ell\xi_{\mathrm{A},\ell}}{v}\overline{\nu}_L\ell_R\mathrm{H}^+ + h.c.\right],$$

where the Higgs mixing factors, $\xi_{a,b}$, are summarized in the Table 2.5.

Table 2.5: Higgs mixing factors in the Yukawa interaction in 2HDM. The c_θ, s_θ, and t_θ are abbreviations of $\cos\theta$, $\sin\theta$, and $\tan\theta$.

	$\xi_{\mathrm{H},u}$	$\xi_{\mathrm{H},d}$	$\xi_{\mathrm{H},\ell}$	$\xi_{\mathrm{h},u}$	$\xi_{\mathrm{h},d}$	$\xi_{\mathrm{h}\ell}$	$\xi_{\mathrm{A},u}$	$\xi_{\mathrm{A},d}$	$\xi_{\mathrm{A},\ell}$
Type-1	c_α/s_β	c_α/s_β	c_α/s_β	s_α/s_β	s_α/s_β	s_α/s_β	t_β^{-1}	$-t_\beta^{-1}$	$-t_\beta^{-1}$
Type-2	c_α/s_β	$-s_\alpha/c_\beta$	$-s_\alpha/c_\beta$	s_α/s_β	c_α/c_β	c_α/c_β	t_β^{-1}	t_β	t_β
Type-X	c_α/s_β	c_α/s_β	$-s_\alpha/c_\beta$	s_α/s_β	s_α/s_β	c_α/c_β	t_β^{-1}	$-t_\beta^{-1}$	t_β
Type-Y	c_α/s_β	$-s_\alpha/c_\beta$	c_α/s_β	s_α/s_β	c_α/c_β	s_α/s_β	t_β^{-1}	t_β	$-t_\beta^{-1}$

It is worth to mention the couplings in the parameter region, $\beta - \alpha \to \frac{\pi}{2}$, referred to as the alignment limit. The Higgs mixing factors in the Table 2.5 reduces to the following values in the Table 2.6. The couplings of the CP-even Higgs boson H in this limit is identical to those of the SM Higgs boson. As seen in the Fig. 2.1, coupling properties of the observed Higgs boson are very close to the SM prediction. This significantly constrains permitted Higgs mixing angles in the 2HDM, as can be seen in the Fig. 2.2. The constraints in the figure were obtained using partial data set available until 2016, yet it already excludes majority of the mixing angles distant from the alignment limit. Having not observed non-SM behaviors of the observed Higgs couplings in subsequent analyses with much larger data set, it is expected that the Higgs structure will be close to the alignment limit, if it is comprised of two doublets.

Table 2.6: Higgs mixing factors in the Yukawa interaction of 2HDM in the alignment limit. The t_θ is an abbreviation of $\tan\theta$.

	$\xi_{\mathrm{H},u}$	$\xi_{\mathrm{H},d}$	$\xi_{\mathrm{H},\ell}$	$\xi_{\mathrm{h},u}$	$\xi_{\mathrm{h},d}$	$\xi_{\mathrm{h},\ell}$	$\xi_{\mathrm{A},u}$	$\xi_{\mathrm{A},d}$	$\xi_{\mathrm{A},\ell}$
Type-1	1	1	1	$-t_\beta^{-1}$	$-t_\beta^{-1}$	$-t_\beta^{-1}$	t_β^{-1}	$-t_\beta^{-1}$	$-t_\beta^{-1}$
Type-2	1	1	1	$-t_\beta^{-1}$	t_β	t_β	t_β^{-1}	t_β	t_β
Type-X	1	1	1	$-t_\beta^{-1}$	$-t_\beta^{-1}$	t_β	t_β^{-1}	$-t_\beta^{-1}$	t_β
Type-Y	1	1	1	$-t_\beta^{-1}$	t_β	$-t_\beta^{-1}$	t_β^{-1}	t_β	$-t_\beta^{-1}$

Figure 2.2: Constraints on the Higgs mixing angles, α and β, of 2HDM from the observed H boson couplings by the CMS Collaboration [22] ($\mathcal{L} = 35.9\,\mathrm{fb}^{-1}$).

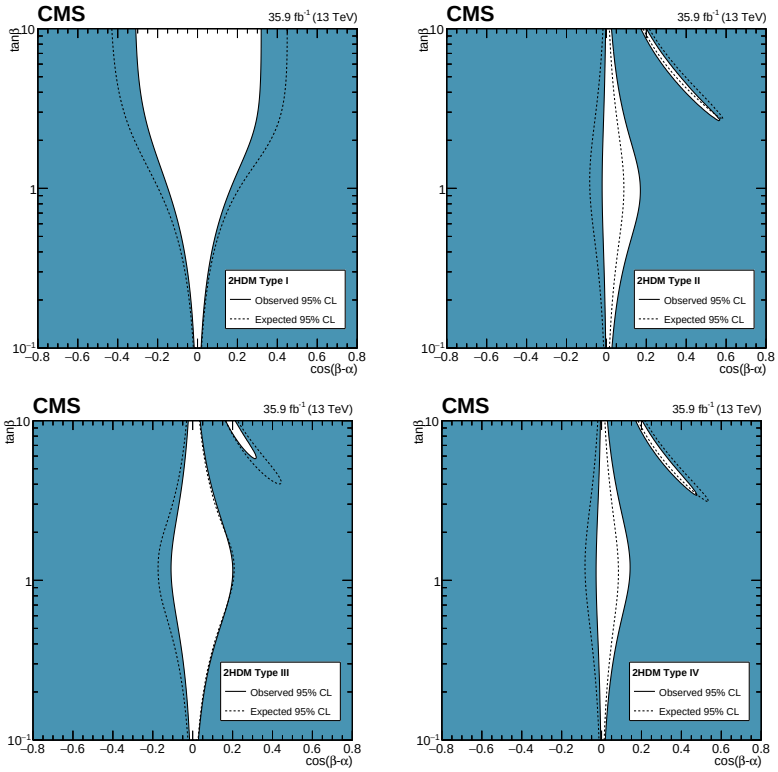

2.2.3 Gauge interactions of Higgs bosons in the 2HDM

The Higgs doublets interact with electroweak gauge bosons, as they are charged in both $SU_L(2)$ and $U_Y(1)$ groups. The interaction terms can be acquired by expanding the covariant kinetic terms of Higgs bosons in the Lagrangian, $(D^\mu \Phi_i)^\dagger (D_\mu \Phi_i)$. An important feature in the gauge interaction of the 2HDM is that the terms linear in CP-even Higgs field are dependent on either $\cos(\beta-\alpha)$ or $\sin(\beta-\alpha)$, hence the three-point and four-point couplings from the gauge interaction can be categorized using their dependence on Higgs mixing angles, as summarized in Table 2.7. The full expansion of the gauge interaction terms can be found in Ref. [58].

Table 2.7: Couplings from gauge interactions of Higgs bosons in 2HDM [63]

$\cos(\beta-\alpha)$	$\sin(\beta-\alpha)$	angle-independent
hW^+W^-	HW^+W^-	–
hZZ	HZZ	–
ZAH	ZAh	ZH^+H^-, γH^+H^-
$W^\pm H^\mp H$	$W^\pm H^\mp h$	$W^\pm H^\mp A$
$ZW^\pm H^\mp H$	$ZW^\pm H^\mp h$	$ZW^\pm H^\mp A$
$\gamma W^\pm H^\mp H$	$\gamma W^\pm H^\mp h$	$\gamma W^\pm H^\mp A$
–	–	W^+W^-HH, ZZHH, W^+W^-hh, ZZhh, W^+W^-AA, ZZAA
–	–	$W^+W^-H^+H^-$, ZZH^+H^-, $\gamma\gamma H^+H^-$, γZH^+H^-

There are important points to be addressed regarding the summarized couplings in the table. In the alignment limit, $\beta - \alpha = \frac{\pi}{2}$, the HW^+W^- and HZZ couplings converge to those of the SM Higgs boson. Hence, parameter regions in this limit will be consistent with the LHC results on the VVH couplings. This

fact, along with the discussed feature of Yukawa couplings of H boson, implies that it can be very difficult to exclude 2HDM in this limit from the study of observed Higgs boson, and escalates the necessity for direct searches. On the other hand, there is no AZZ and AW^+W^- coupling regardless of Higgs mixings, and hZZ and hW^+W^- couplings vanish in the alignment limit. Therefore these unobserved neutral Higgs bosons cannot be produced in a vector boson fusion or decay to a vector boson pair.

The CP-odd Higgs boson does not couple to the SM-like Higgs boson via gauge interaction in the aligned limit, as the ZAH coupling vanishes. On the contrary, the ZAh coupling is maximized in this case. To be consistent with the null results from searches for $e^+e^- \to Z^{(*)} \to Ah$ at LEP, at least one of the unobserved neutral Higgs boson is likely to be heavy, $m_A + m_h > 209\,\text{GeV}$.

The $ZH^+H^-/\gamma H^+H^-$ couplings are always unsuppressed and independent of Higgs mixings. Thus the pair production channel, $f\bar{f} \to \gamma^{(*)}/Z^{(*)} \to H^+H^-$, forms one of the main H^+ production channels in 2HDM. This channel was used for H^+ boson searches at LEP, where top quark production was kinematically forbidden. However, for a given H^+ boson mass, this channel may require higher collision energy compared to production channels using Yukawa couplings, $\bar{u}dH^+$, because of the two H^+ bosons in the final state.

Finally, three-point gauge interactions of the H^+ boson has the form of $W^-H^+\phi$, where ϕ are neutral Higgs bosons, and there is no H^+W^-Z couplings, which can be found in Higgs Triplet Models. In the alignment limit, the W^-H^+H coupling vanishes, hence the H^+ boson cannot decay to a W^+H boson pair. If bosonic decay modes of the H^+ boson is kinematically permitted, then it must be a pair of W^+ and unobserved neutral Higgs bosons. The Lagrangian terms responsible for this decay has the form [58],

$$\mathcal{L}_{\mathrm{H^+WA}} = -\frac{g_{\mathrm{W}}}{2}[\mathrm{W}^+_\mu(\mathrm{H}^-\partial^\mu\mathrm{A} - \mathrm{A}\partial^\mu\mathrm{H}^-) + \mathrm{W}^-_\mu(\mathrm{H}^+\partial^\mu\mathrm{A} - \mathrm{A}\partial^\mu\mathrm{H}^+)] \quad (2.25)$$

$$\mathcal{L}_{\mathrm{H^+Wh}} = i\frac{g_{\mathrm{W}}}{2}\sin(\beta-\alpha)[\mathrm{W}^+_\mu(\mathrm{H}^-\partial^\mu\mathrm{h} - \mathrm{h}\partial^\mu\mathrm{H}^-) + \mathrm{W}^-_\mu(\mathrm{H}^+\partial^\mu\mathrm{h} - \mathrm{h}\partial^\mu\mathrm{H}^+)],$$

implying that the coupling strength is at weak interaction scale without additional suppression factors.

2.2.4 Production and Decay Rates of Higgs Bosons

Each of Higgs bosons in the 2HDM has its own production and decay modes determined by the couplings of the Yukawa, scalar, and weak interactions. Feasibility of these processes can be highly dependent on details of experiments and considered parameter regions. In this section, the production and decay of charged and CP-odd Higgs bosons are discussed.

Production of H^+ bosons

The H^+ boson with an electroweak scale mass can be produced in pair-production ($\mathrm{H}^+\mathrm{H}^-$) or Yukawa production channels ($\bar{u}d\mathrm{H}^+$). Pair-production of $\mathrm{e}^+\mathrm{e}^- \to \gamma^{(*)}/\mathrm{Z}^{(*)} \to \mathrm{H}^+\mathrm{H}^-$ was considered the main production channel at LEP experiments. The Yukawa production, $\mathrm{e}^+\mathrm{e}^- \to \gamma^{(*)}/\mathrm{Z}^{(*)} \to \mathrm{b\bar{c}H}^+$, was in general expected to be suppressed, as top quark productions were kinematically inaccessible and production rate from lighter quarks are suppressed by $(m_q/v)^2$, of which order is less than 10^{-4}. On the contrary, as discussed in the previous section, the pair-production from $\mathrm{ZH}^+\mathrm{H}^-/\gamma\mathrm{H}^+\mathrm{H}^-$ couplings are independent of Higgs mixings and always unsuppressed.

The production conditions at high energy hadron collider experiments as the Tevatron and LHC are drastically different from the lepton collision experiments. Hadrons are bound states of quarks, hence various constituent quarks,

called 'valence quarks', and virtual particles mediating the inter-quark interaction in the hadrons, referred to as 'sea partons', can be candidates for the incoming elementary particle in the collision. As the quarks participate in all known gauge and Yukawa interactions, entire SM particles can be included in the incoming particles if the energy scale of collision is sufficiently high. This feature often complicates and impose a model-dependency on searches for extended Higgs sectors.

The H^+H^- pair production is among the examples with such a feature. Pair-production of H^+ boson at LHC are mainly initiated from $q\bar{q}$, yet it can be mediated by exchange of a vector boson, $q\bar{q} \to \gamma^{(*)}/Z^{(*)} \to H^+H^-$, neutral Higgs boson ($b\bar{b} \to H/h \to H^+H^-$), and various vector boson fusion modes involving scalar-scalar, gauge, and Yukawa interactions, $qq \to qqH^+H^-$. The gluon-initiated processes, $gg \to H^+H^-$, are also required to be considered for the pair-production at LHC. These processes are mediated by rectangular quark loops connecting effective vertex of ggH^+H^-, triangular quark loops forming effective vertices of gH^+H^-, ggH, ggh, and scalar-scalar interactions, HH^+H^- and hH^+H^-. The gluon-initiated processes contribute approximately less than O(10%) of the quark-initiated production rates [64]. The total cross section of H^+H^- pair-production is at the order of 100 fb for m_{H^+} lower than m_t and $\sqrt{s} = 14\,\text{TeV}$. However, if the gluon-initiated processes can be mediated by resonant neutral Higgs bosons, $gg \to \phi \to H^+H^-$, the production rate can reach a few pb and exceed the quark-initiated contribution [65].

In contrast with the e^+e^- collision experiments at LEP, single production of a H^+ boson is possible in pp collisions at the LHC. For a H^+ boson lighter than a top quark, this can proceed via top quark decays in $t\bar{t}$ productions, $gg \to t\bar{t} \to b\bar{b}W^-H^+$, direct productions, $c\bar{s} \to H^+$, and weak decays of neutral Higgs bosons, $gg \to \phi \to W^-H^+$. In the m_{H^+} scale and LHC conditions, the

production from top quark decays dominate and the two latter channels are ignorable. The production rate is approximately a few hundred pb and fb for the top and other channels, respectively [32, 65].

The partial widths of top quarks decays, $t \to W^+b/H^+b$, are given as [66],

$$\begin{aligned} \Gamma(t \to W^+b) &= \frac{G_F m_t^3}{8\sqrt{2}\pi}(1 + 2x_{Wt})(1 - x_{Wt})^2 \\ \Gamma(t \to H^+b) &= \frac{G_F m_t^3}{8\sqrt{2}\pi}(\xi_{A,u}^2 + x_{bt}\xi_{A,d}^2)(1 - x_{H^+t})^2, \end{aligned} \tag{2.26}$$

where x_{ab} is defined as m_a^2/m_b^2, G_F is the Fermi constant, and the CKM matrix element $|V_{tb}|$ is approximated to be one. As can be seen in the Table. 2.5, the Higgs mixing factor for up-type quark, $\xi_{A,u}$, is $\cot\beta$ for all 2HDM models with Z_2 symmetry, the H^+ production from a top quark decay is the most prominent at a low $\tan\beta$ region. The Yukawa interaction of H^+ bosons involve both up- and down-type quarks, hence in couplings scenarios where the Higgs mixing factor for down-type quarks, $\xi_{A,d}$ increase with $\tan\beta$, the H^+ production can be large at high $\tan\beta$ region as well. The type-2 and -Y Yukawa couplings correspond to this scenario. On the contrary, the H^+ production in top quark decay is suppressed in the high $\tan\beta$ region of type-1 and -X coupling scenarios. These behavior of top quark decays can be seen in Fig. 2.3.

Decay of H^+ bosons

The H^+ bosons can decay via Yukawa and weak interactions. Bosonic decays mediated by gauge interaction can result in transition to $W\phi$ final states. As mentioned in the previous section, the LEP searches on the ZAh coupling constrains the scenario of two unobserved neutral Higgs bosons with simultaneously light mass values, single neutral Higgs boson is considered for the bosonic decay mode in this thesis. Light CP-odd Higgs boson scenario, $m_A < 100\,\text{GeV}$,

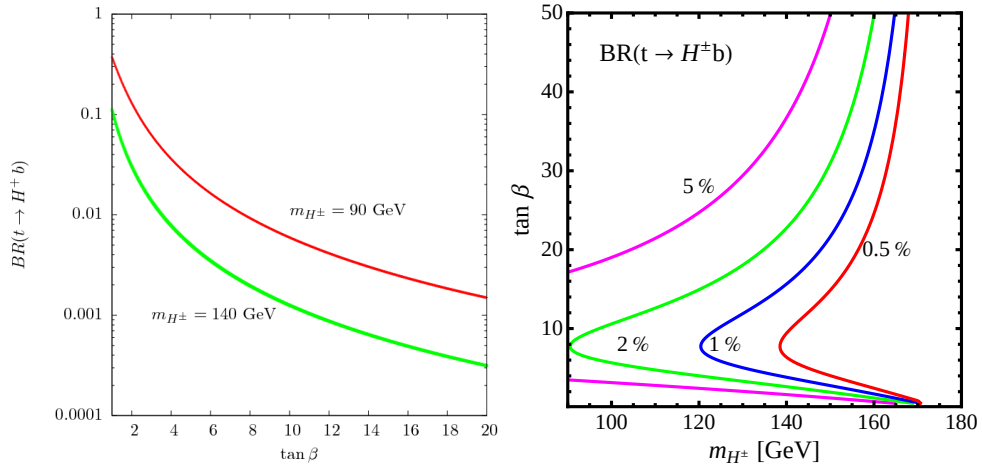

Figure 2.3: Branching fraction, $\mathcal{B}(\mathrm{t} \to \mathrm{bH}^+)$, in type-1 and -X (left), and type-2 and -Y (right) 2HDM [45, 65].

is favored in the context of the g-2 anomaly [29], and the CP-odd Higgs boson has less dependence on Higgs mixing angles when compared to the CP-even Higgs boson. For these reasons, WA decay mode is considered for the bosonic decay mode. However, kinematics and model prediction of the Wh mode for a given neutral Higgs mass is expected to be similar to WA, hence it is anticipated that the result of this analysis can be easily re-interpretable in the opposite scenario of light h and heavy A bosons.

The mass of H^+ boson between $(m_\mathrm{A} + 85)$ and 160 GeV is considered in the thesis. The mass range is determined from kinematically permitted region of the considered decays, $\mathrm{t} \to \mathrm{bH}^+$ and $\mathrm{H}^+ \to \mathrm{W}^+\mathrm{A}$. The decay rate vanishes at the mass thresholds, $m_\mathrm{t} = m_{\mathrm{H}^+} + m_\mathrm{b}$ and $m_{\mathrm{H}^+} = m_\mathrm{W} + m_\mathrm{A}$. In order to avoid vector meson backgrounds, the A boson mass is considered from 15 GeV. The maximal m_A value is determined to be 75 GeV from the H^+ boson mass boundaries.

The partial decay width of the bosonic decay mode can be calculated as [44],

$$\Gamma(\mathrm{H}^+ \to \mathrm{W}^+\mathrm{A}) \;=\; \frac{G_F m_{\mathrm{H}^+}^3}{8\sqrt{2}\pi}\lambda^{3/2}(1, x_{\mathrm{AH}^+}, x_{\mathrm{WH}^+}). \tag{2.27}$$

Here, the definition of x_{ab} is the same as before, and $\lambda(x, y, z)$ is the Källén function, defined as $\lambda(x, y, z) \equiv x^2 + y^2 + z^2 - 2xy - 2yz - 2zx$. As explained previously, the partial width have dependence on neither Higgs mixing angles nor Yukawa coupling structures, but only on the mass of the H^+ and A bosons. The calculated width values in the considered mass region are approximately a few hundred MeV, and increases with mass splittings between the H^+ and A bosons, as shown in Fig. 2.4.

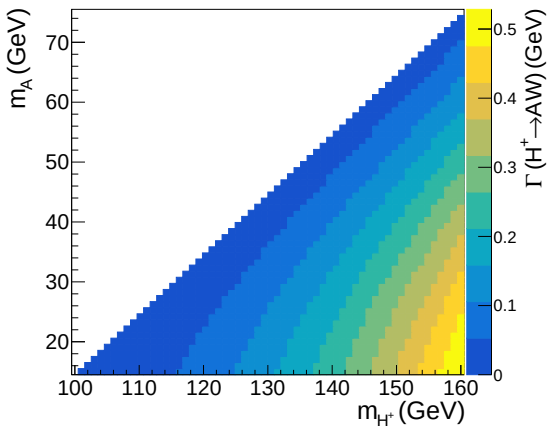

Figure 2.4: Partial width values of the decay, $\mathrm{H}^+ \to \mathrm{W}^+\mathrm{A}$, in the unit of GeV at the m_{H^+} and m_{A} values considered in the thesis.

On the other hand, fermionic decay modes of H^+ bosons are mediated by the Yukawa interaction. These interactions are highly dependent on the Higgs mixing angles connecting the basis for the Yukawa interaction and Higgs mass eigenstates. The partial decay widths in this category can be calculated as [67],

$$\Gamma(\phi^{+,0} \to f_1\overline{f_2}) = \frac{N_C m_\phi}{8\pi}\{[1-(x_{f_1\phi}^{1/2}+x_{f_2\phi}^{1/2})^2]|C_S|^2 + [1-(x_{f_1\phi}^{1/2}-x_{f_2\phi}^{1/2})^2]|C_P|^2\} \times \lambda^{1/2}(1, x_{f_1\phi}, x_{f_2\phi}). \quad (2.28)$$

Here, the $\phi^{+,0}$ are neutral or charged Higgs boson, N_C is the color factor, which is respectively 3 and 1 for quarks and leptons. The $C_{S,P}$ are coefficient of scalar and pseudoscalar interaction terms in the Eq. 2.24. For the A and H^+ bosons considered in the analysis, these coefficients can be summarized as,

$$\begin{aligned} &\text{A boson} : C_S = 0 \ , \ C_P = -i\frac{m_f}{v}\xi_{A,f} \quad (2.29)\\ &H^+ \text{ boson} : C_S = \frac{V_{ud}}{\sqrt{2}v}(m_u\xi_{A,u} + m_d\xi_{A,d}) \ , \ C_P = -\frac{V_{ud}}{\sqrt{2}v}(m_u\xi_{A,u} - m_d\xi_{A,d}) \\ &\qquad \text{or} \ \ C_S = \frac{m_\ell \xi_{A,\ell}}{\sqrt{2}v} \ , \ C_P = \frac{m_\ell \xi_{A,\ell}}{\sqrt{2}v}, \end{aligned}$$

with the same convention as the Eq. 2.24 and Table 2.5 for the mixing factors.

Total fermionic decay widths can be calculated by accumulation of partial widths for all fermion pairs, as shown in the Fig 2.5. Major contribution to the fermionic decay width originate from the heaviest fermion pairs, $t\bar{b}$, $c\bar{b}$, $c\bar{s}$, and $\tau\nu$. Relative dominance is determined by magnitudes of their mass, Higgs mixing, and CKM matrix elements. Total fermionic H^+ decay width is suppressed at m_{H^+} values below m_t threshold due to small Yukawa couplings of lighter quarks, $(m_q/v)^2$, and it is less than a few hundred MeV in this m_{H^+} region. Especially, for $\tan\beta$ range between 1 and 10, in which $\mathcal{B}(t \to bH^+)$ is large, the total fermionic decay width is below 20 MeV in all Yukawa coupling types of the 2HDM.

Comparison of these total bosonic and fermionic decay widths of the H^+ boson reveals that, if a light neutral Higgs boson exists with a mass splitting

$m_{H^+} - m_A$ larger than the m_W value, the bosonic decay mode is expected to be a predominant H^+ decay mode for Higgs mixing values with unsuppressed $t \to bH^+$ decays. This elucidates the importance of probing bosonic decay modes of the H^+ boson at the LHC experiments.

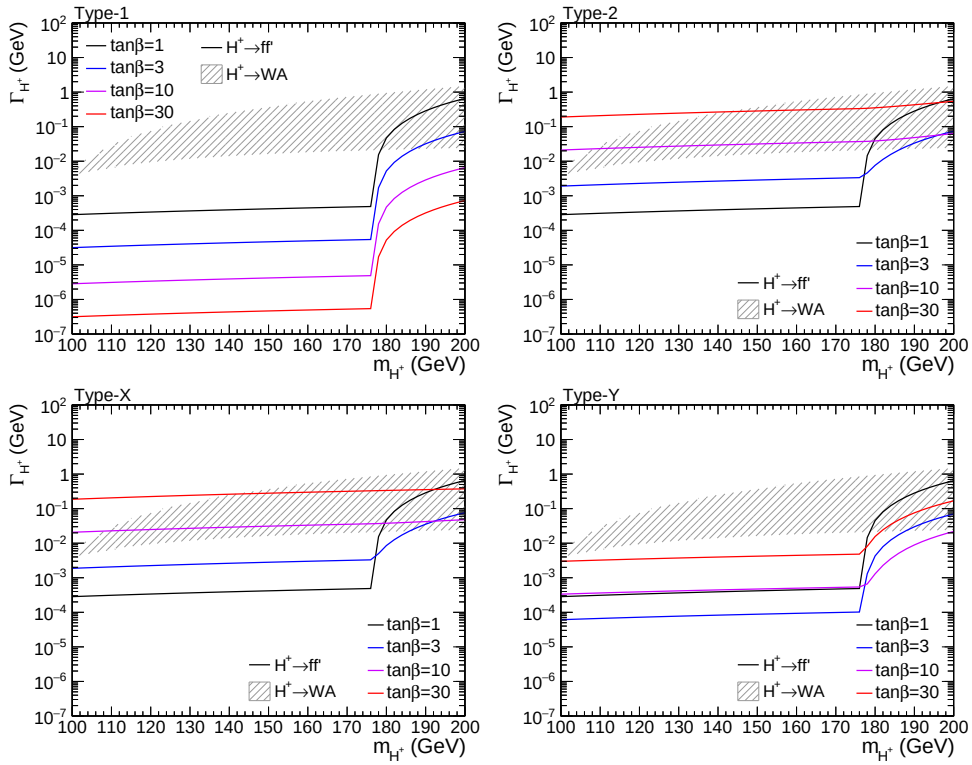

Figure 2.5: Fermionic (solid line) and bosonic (shaded) decay widths of the H^+ boson at various scalar mass and $\tan\beta$ values in type-1, -2, -X, and -Y 2HDM. The bosonic width bands are obtained for $15 \leq m_A \leq (m_{H^+} - 85)$ GeV.

Decay of A bosons

The A boson, produced in the H^+ decays, can decay to fermions and bosons. Fermionic decay modes, $A \to f\bar{f}$, are mediated by the Yukawa interaction

and described by the same formula with the H^+ boson, Eq. 2.28, yet with the different scalar and pseudoscalar amplitudes as described in Eq. 2.29. The A boson can decay to all fermions with mass, and main contribution to the total fermionic decay width comes from $b\bar{b}$, $\tau\tau$, and $t\bar{t}$, for $m_A > 2m_t$. For bosonic decay modes, the A boson can decay to a vector boson pair with a mass value lighter than $m_A/2$. As the A boson does not couple to a gauge boson pair, these decay modes are mediated at loop levels, hence decay modes for electroweak gauge bosons are highly suppressed by a factor α^2. In contrast, the gg decay modes may form a significant decay width through the large values of α_S and Yukawa couplings of top quarks. The partial A decay width for the gg mode can be calculated as [32],

$$\begin{aligned}
\Gamma(A \to gg) &= \frac{G_F \alpha_S^2 m_A^3}{16\sqrt{2}\pi^3} \left| \sum_q \xi_{A,q} \left(\frac{2m_q}{m_A}\right)^2 f\left(\left(\frac{2m_q}{m_A}\right)^2\right) \right|^2 \qquad (2.30)\\
\text{with} \quad f(x) &= \left(\arcsin\left(\sqrt{1/x}\right)\right)^2 \qquad \text{for } x \geq 1,\\
&= -\frac{1}{4}\left(\ln\left(\frac{1+\sqrt{1-x}}{1-\sqrt{1-x}}\right) - i\pi\right)^2 \qquad \text{for } x < 1.
\end{aligned}$$

In the calculation of decay widths of Higgs bosons, higher order corrections in quantum chromodynamics (QCD) is known up-to NLO and NNLO for gluon-pair [68] and quark-pair decay modes [69–71]. These corrections are considered in the hadronic decay widths of H^+ and A bosons.

$$\begin{aligned}
\Gamma_{qq,\mathrm{NNLO}} &= \Gamma_{qq,\mathrm{LO}}\left(1 + 5.67\frac{\alpha_S(m_\phi)}{\pi} + (35.94 - 1.36n_f)\left(\frac{\alpha_S(m_\phi)}{\pi}\right)^2\right)\\
\Gamma_{gg,\mathrm{NLO}} &= \Gamma_{gg,\mathrm{LO}}\left(1 + (24.25 - 1.17n_f)\frac{\alpha_S(m_\phi)}{\pi}\right) \qquad (2.31)
\end{aligned}$$

Here, the n_f is the number of active quark flavors, and α_S is evaluated at the scale $\mu = m_\phi$ in $\overline{\mathrm{MS}}$ scheme and at 4-loop order [72]. Running Yukawa couplings

from quark masses are calculated at the same scale, loop-order, and scheme [73].

The total decay width of the A boson is shown in the Fig. 2.6. The decay width values are below a few hundred MeV in the region of Higgs mixing angles, $\tan\beta \lesssim 20$, important for this search. For the m_{A} range considered in this thesis, main contribution to the decay width originate from $\mathrm{b\bar{b}}$ and $\tau^+\tau^-$ decay modes, as shown in the figure for $m_{\mathrm{A}} = 45\,\mathrm{GeV}$. The branching fraction to the gg decay mode is approximately a few percent when couplings to up-type quarks are unsuppressed. The branching fraction for the $\mu^+\mu^-$ decay mode is approximately 0.35% for type-X Yukawa couplings and 0.03% for type-1 and -2 Yukawa couplings at plateaus. The $\mu^+\mu^-$ decay mode is in general suppressed in type-Y Yukawa couplings except a small marginal region around $\tan\beta \sim 1$.

2.2.5 Experimental Constraints

The 2HDM has a long history of experimental investigation, since the proposal of the first version of the model by T. D. Lee in 1973 [74]. In this section, the experimental results relevant for the subject of this thesis will be discussed.

Searches for the H^+ boson

The earliest direct search results for the electroweak scale H^+ boson were obtained at the LEP experiments [49, 75–79]. The pair production of H^+ boson from $\mathrm{e^+e^-}$ collisions at $\sqrt{s}$ between 183 and 209 GeV were investigated for the H^+ boson mass between 40 and 100 GeV. The H^+ boson mass lower than 40 GeV was not considered, as it was already excluded by the limits on the non-SM contribution to the Z width measured in LEP1 era. All major decay modes of H^+ bosons, $\tau\nu$, $\mathrm{c\bar{s}}$, and WA, were considered in the search. For the bosonic H^+ decay mode, the main decay mode, $\mathrm{b\bar{b}}$, of the A boson was considered, and this motivates the m_{A} range between 12 and 70 GeV, close to $2m_{\mathrm{b}}$ and $m_{\mathrm{H^+}}$.

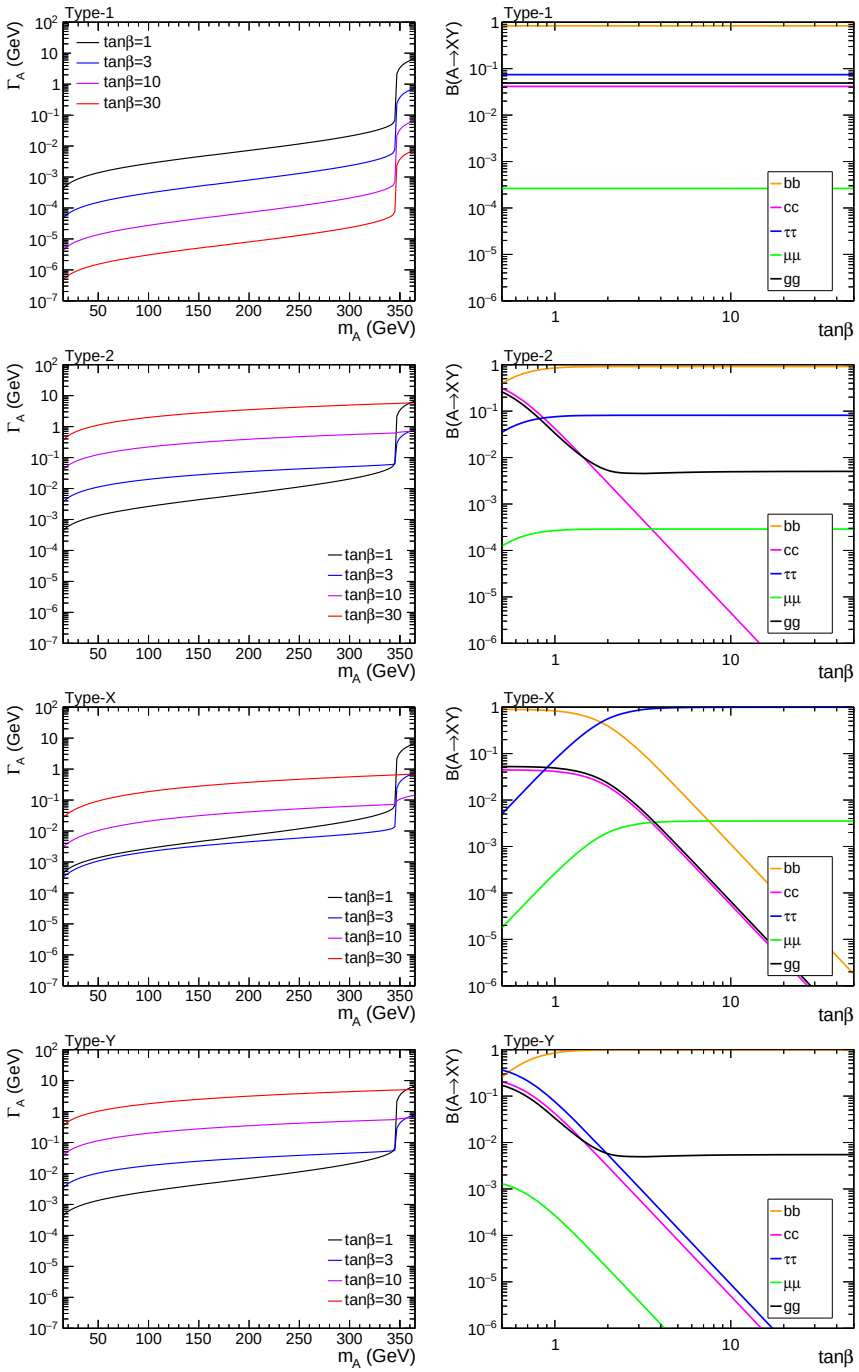

Figure 2.6: Total decay widths (left) and branching fractions (right, m_{A}=45 GeV) for each decay modes of the A boson in type-1, -2, -X, and -Y 2HDM.

It is worth to mention that the on-shell WA decay mode is closed in most of the mass region available at the LEP. Hence, the WA decay mode at the LEP refers to three body decays of the H^+ boson mediated by a virtual W* field, $H^+ \to A f f'$. Such an off-shell decay mode is in general suppressed, hence it is meaningful only when the total fermionic decay width is negligible as the type-1 2HDM (Fig. 2.5), where the fermionic decay width can be smaller than the bosonic width by a factor less than 10^{-5}. Therefore, the WA decay mode is considered only for the type-1 2HDM with the subsequent $A \to b\bar{b}$ decays, which is predominant for all Higgs mixing angles in the model. The combination of LEP results in all decay channels excluded the H^+ mass below 72.5 and 80 GeV at 95% CL for type-1 and -2 2HDM, respectively [51]. Although the type-X and -Y 2HDM were not considered in the global combination, yet decay patterns of the H^+ boson in type-X and -Y are similar to those in the type-2 2HDM. Main H^+ decay mode of the type-X 2HDM is identical to the type-2 2HDM, and those of the type-Y 2HDM is $\tau\nu$ and $c\bar{b}$ modes, experimentally identical to type-2 2HDM as inclusive di-jet final states. Therefore, similar level of constraint as the type-2 2HDM is expected for type-X and -Y 2HDM from this result.

The next direct search results for the H^+ bosons comes from the Tevatron experiments [47, 48, 80–82]. The CDF and D0 Collaborations looked for the H^+ boson produced in decay of top quarks in $t\bar{t}$ events, produced from $p\bar{p}$ collisions at $\sqrt{s} = 1.96$ TeV. The decay modes, $c\bar{s}$, $\tau\nu$, $t^*\bar{b}$, Wh, and WA, are considered for the H^+ boson. Upper limits at 95% CL were set on the $\mathcal{B}(t \to bH^+)\mathcal{B}(H^+ \to c\bar{s})$ between approximately 0.1 and 0.2, and on the $\mathcal{B}(t \to bH^+)\mathcal{B}(H^+ \to \tau\nu)$ at approximately 0.2 for the m_{H^+} values between 80 and 155 GeV. The $t^*\bar{b}$, Wh, and WA with $h/A \to b\bar{b}$ modes were considered in the earliest analysis with highly limited statistics, therefore the search barely excluded parameter regions

of the considered model. The WA decay mode was also considered in the context of NMSSM, in which a very light CP-odd Higgs boson is expected. The search set the upper limits (95% CL) on the $\mathcal{B}(t \to bH^+)\mathcal{B}(H^+ \to WA)\mathcal{B}(A \to \tau\tau)$ between approximately 0.1 and 0.5 for the m_{H^+} values between 85 and 160 GeV and m_A values between 4 and 9 GeV. The D0 Collaboration also looked for the H^+ production beyond the m_t threshold, using the direct s-channel production, and set upper limits (95% CL) on the $\sigma(q\bar{q} \to H^+)\mathcal{B}(H^+ \to t\bar{b})$ at a few pb.

The last direct search results for the H^+ bosons were obtained by the LHC experiments in Run-1 [33–42]. The CMS and ATLAS Collaborations searched for the H^+ bosons produced in pp collisions at $\sqrt{s} = 7$ and 8 TeV. The main fermionic decay modes, $c\bar{s}$, $c\bar{b}$, and $\tau\nu$, are considered for $m_{H^+} < m_t$, and the $\tau\nu$ and $t\bar{b}$ decay modes are considered for m_{H^+} values beyond m_t.[1] The light H^+ bosons are considered to be produced in top quark decays in $t\bar{t}$ events in both Collaborations, yet the associated production, $\bar{t}bH^+$, is considered by the CMS Collaboration and s-channel production is considered by the ATLAS Collaboration. For the m_{H^+} values between 80 and 160 GeV, upper limits (95% CL) are set on the $\mathcal{B}(t \to bH^+)\mathcal{B}(H^+ \to XY)$ between 1.2 and 6.5% for the $c\bar{s}$ mode, between 0.3 and 1.4% for the $c\bar{b}$ mode, and between 0.15 and 1.2% for the $\tau\nu$ mode. For heavier m_{H^+} values, upper limits (95% CL) are set on the $\sigma_{H^+}\mathcal{B}(H^+ \to XY)$ between a few hundred to a few fb for the $\tau\nu$ mode, between 0.13 and 1.99 pb for the $t\bar{b}$ decay mode with the associated production channel.

Note that only the results based on LHC Run-1 were available when the contents of this thesis was studied, hence the results published since then cannot be considered as the background knowledge for this thesis and are not introduced

[1] There was also an analysis looking for H^+ in cascade decays of a heavier scalar boson, using $H^+ \to W^+H$ decays, yet the H^+W^+H coupling vanishes in the alignment limit and it does not exclude any parameter region near the limit, as explicitly mentioned in the paper [83]. The search is considered irrelevant in the context of the 2HDM.

in this section.

These limits on the direct search for the H^+ boson implies that it must be heavier than approximately the m_W value, and either fermionic H^+ decay rates or the top quark Yukawa coupling is suppressed, if a light H^+ boson exists. The bosonic H^+ decay mode is strongly related to both cases, and it needs to be investigated for the main production channel at the LHC. However, this requires the existence of a light unobserved neutral Higgs boson, which also receives constraints from preceding experiments.

Searches for the A boson

As explained earlier, the OPAL Collaboration at the LEP searched for the pair production of the CP-odd and -even Higgs bosons, $e^+e^- \to Z^* \to hA$, with $\sqrt{s}$ values between 191.6 and 209 GeV [84–86]. In the context of the type-2 2HDM, the $h/A \to q\bar{q}/gg/\tau\tau$ and $h \to AA$ decay modes were investigated. Exclusion limits at 95% CL were set on the two Higgs boson masses in various parameter regions, and the mass region, $1 \lesssim m_h \lesssim 55$ and $3 \lesssim m_A \lesssim 63$ (GeV), was excluded for all $\tan\beta$ values of the model. This result imposes strong constraints on the parameter region of simultaneously light unobserved neutral Higgs bosons, within $m_A + m_h < 209$ GeV.

The m_A region below $2m_b$ thresholds is strongly restricted by the B factory results [87–92]. Babar and CLEO Collaborations investigated the production of A bosons from the radiative $\Upsilon(nS)$ decays, $\Upsilon(nS) \to \gamma A$ ($n = 1, 2, 3$). The $\tau\tau$, $\mu\mu$, hadronic, and invisible decay modes of the A boson were investigated for m_A values between the mass of $\Upsilon(nS)$ and its daughter particles, depending on the decay modes. The invisible decay mode assumes extension of the particle spectra larger than the 2HDM to be permitted. These searches set upper limits (90% CL) on the product of branching fractions, $\mathcal{B}(\Upsilon(nS) \to \gamma A)\mathcal{B}(A \to XY)$,

between 2.8×10^{-7} and 1.3×10^{-4}, depending on the decay mode and m_{A} values. These results impose stringent constraints on the 2HDM with a light m_{A} scenario below the Upsilon mass. For instance, the $\tau\tau$ decay channel alone exclude entire region of $\tan\beta \gtrsim 1$ for the m_{A} range in the type-2 2HDM [93].

The last important direct limits on the light A bosons arise from the LHC searches [94–96]. The CMS Collaboration searched for the gluon fusion production of A boson with subsequent muonic decays, $\mathrm{gg} \to \mathrm{A} \to \mu\mu$, and the Yukawa production channel from bottom quark with subsequent tauonic and muonic decays, $\mathrm{gg} \to \mathrm{b\bar{b}A} \to \mathrm{b\bar{b}}\tau\tau/\mathrm{b\bar{b}}\mu\mu$. The searches are based on the pp collision experiments at $\sqrt{s}$ value of 7 TeV for the gluon fusion channel and 8 TeV for the Yukawa production channels. The gluon fusion channel search investigated m_{A} values between 5.5 and 14 GeV, and set upper limits (95% CL) on the product, $\sigma_{\mathrm{A}}\mathcal{B}(\mathrm{A} \to \mu\mu)$ at approximately a few pb. The model-independent limit is translated into the Higgs mixings in the NMSSM, and have shown that the result imposes similar level of constraints as the B factories for the considered m_{A} values.

The Yukawa production channels considered m_{A} values between 25 and 80 GeV, and upper limits (95% CL) has been set on the product, $\sigma_{\mathrm{A}}\mathcal{B}(\mathrm{A} \to \mathrm{XY})$, between 7 and 39 pb for the tau channel, and at a few hundred fb for the muon channel. When the model-independent limits are translated to 2HDM+S models, the limit values from these channels are much higher than the gluon fusion channel in relatively low $\tan\beta$ scenarios. This is an expected feature as the Yukawa production channel of A boson is minor compared to the gluon fusion case except an extreme parameter region where Higgs mixing factor highly suppresses the top Yukawa coupling and enhances the bottom quark coupling at the same time [97]. Therefore the constraints from the production of A boson from gluon fusion and Yukawa production channels were relatively

relaxed for the $m_{\rm A}$ values larger than 14 GeV.

Finally, the light neutral Higgs boson with $m_\phi < m_{\rm H}/2$ can potentially open the Higgs-pair decay modes of the observed Higgs boson, H $\to$ AA/hh, through the scalar-scalar interactions in the scalar potential of the Lagrangian. The partial decay width for the A-pair decay mode in the alignment limit can be calculated as [98–100],

$$\Gamma(\mathrm{H} \to \mathrm{AA}) = \frac{(4m_{12}^2/\sin 2\beta - m_{\rm H}^2 - 2m_{\rm A}^2)^2}{32\pi v^2 m_{\rm H}} \lambda^{1/2}(1, x_{\rm AH}, x_{\rm AH}), \qquad (2.32)$$

where the m_{12} is the coefficient of the soft Z_2-breaking term of the Higgs potential in Eq. 2.14. As can be seen from the formula, this process can be the leading Higgs decay mode, if it is kinematically allowed and the splitting between the m_{12} and mass of Higgs bosons is large.

The scalar decay modes of the observed Higgs bosons was extensively investigated at the LHC, mainly in the context of the NMSSM. The CMS and ATLAS Collaborations inspected if the observed Higgs boson, produced in pp collision at $\sqrt{s} = 8$ TeV, decays to a lighter neutral Higgs bosons with a mass value between 0.25 and 62.5 GeV [101–105]. The decay modes of the two A bosons were considered for $\mu\mu\mu\mu$, $\tau\tau\tau\tau$, $\mu\mu$bb, $\mu\mu\tau\tau$, and $\gamma\gamma\gamma\gamma$ final states, and the scalar decay mode was not observed. Upper limits (95% CL) were set on $\frac{\sigma_{\rm H}}{\sigma_{\rm H,SM}}\mathcal{B}(\mathrm{H} \to \mathrm{AA})$ values, identical to $\mathcal{B}(\mathrm{H} \to \mathrm{AA})$ in the alignment limit, at approximately 10^{-2} below the J/ψ mass, at 1 for below 9 GeV and beyond 25 GeV, and at $\sim$50 for else regions, with $\tan\beta = 1$. Reinterpretation of this limit in other Yukawa coupling types and various $\tan\beta$ scenario was also introduced. The constraints for $m_{\rm A}$ values beyond the Upsilon mass was not restrictive except the type-X 2HDM with $\tan\beta \gtrsim 1$ and type-Y 2HDM with $\tan\beta \lesssim 1$. Therefore, the light A boson is expected to be compatible with

this constraint for a large parameter region of the 2HDM. Nevertheless, for the m_{12} values close to $\frac{1}{2}\sqrt{\sin 2\beta(m_{\rm H}^2 + 2m_{\rm A}^2)}$, the scalar decay mode is highly suppressed and the A boson lighter than $m_{\rm H}/2$ can still be a viable scenario for all other parameters of the 2HDM. The parameter regions for the bosonic decays of a $\rm H^+$ boson also includes $m_{\rm A}$ bosons heavier than $m_{\rm H}/2$, and in this case, the light A boson scenarios are free from the constraints from scalar decay modes, regardless of the soft Z_2-breaking term.

The experimental results on direct searches for the A bosons imply that the A boson with a mass value below 14 GeV in the 2HDM is difficult to be compatible with the results. Constraints on the $m_{\rm A}$ values between 15 and 80 GeV are relatively loose, and moderate Higgs mixing scenario is compatible with the results for this range. Constraints from the scalar decay modes of the observed Higgs boson until Run-1 are loose for the $m_{\rm A}$ beyond the Upsilon mass. Unless observing the scalar decay modes in the accumulated data from the consecutive data-takings, this will imply that either the $m_{\rm A}$ value is larger than $m_{\rm H}/2$ or the soft Z_2-breaking term is close to $\frac{1}{2}\sqrt{\sin 2\beta(m_{\rm H}^2 + 2m_{\rm A}^2)}$. The bosonic decays of a light $\rm H^+$ occurs in both $m_{\rm A}$ regions, hence this $\rm H^+$ decay mode must be checked at the LHC to complete the 2HDM searches.

Chapter 3

Experiment

3.1 Large Hadron Collider

The Large Hadron Collider (LHC) [106–108] is a hadron collider, which accelerates and collides protons and heavy ions, located in Geneva, Switzerland. The LHC provides two hadron beams with high energy and high luminosity, colliding at four interaction points on its circumference. The LHC hosts five experimental facilities at the interaction points, the CMS and ATLAS experiments for the study of central activities from pp collisions, the LHCb experiment for the study of B-physics with forward activities from pp collisions, the ALICE experiment for the study of heavy-ion collisions, and the TOTEM experiment for the study of elastic and diffractive scattering of protons at an extreme forward region. In this section, experimental details on the acceleration and collision of protons at the LHC, related to the subject of the thesis, will be briefly described.

3.1.1 Design

The LHC is a synchrotron-type circular collider with the circumference length of 26.7 km. The machine is installed in the tunnel between 45 and 170 m below the surface, inclined with a sloping of 1.4% towards the Leman lake. The tunnel is comprised of 8 arcs and 8 straight sections, as shown in the Fig. 3.1.

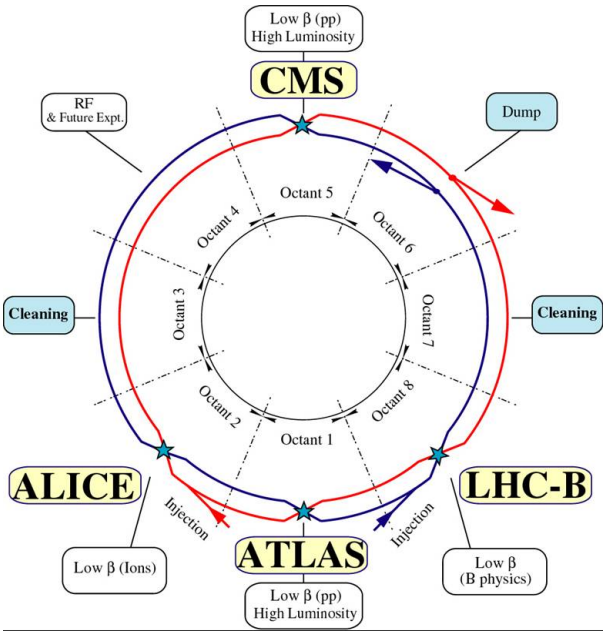

Figure 3.1: The schematic figure of the LHC machine [108].

Each straight section is approximately 528m long and equipped with an experimental facility for either maintenance or data-taking. The straight section at Octant 1, 2, 5, and 8 houses the detectors for the previously described experiments, and Octant 3, 4, 6, and 7 contains equipments for beam cleaning, radio-frequency (RF) cavity for the acceleration, and aborting beams.

The arcs between the straight sections consist of 106m long 23 cells, made of 46 half cells. Each half cell is made up of 5.355 m cold mass and a short

straight section assembly, and three 14.3 m long dipole magnets. In between arcs and straight sections, a series of quadruple magnets referred to as dispersion suppressors are located to minimize dispersion of beams produced in the arc.

The two proton beams enter the tunnel from the long straight section 2 and 8, and transported along the tunnel. As the LHC is a particle-particle collider, the direction of magnetic field to bend the beam trajectory must be opposite for the two beams. The LHC adopted the twin-bore magnet design, shown in Fig. 3.2, in order to satisfy the space limitations on the existing tunnel built for the previous LEP experiment. The two beams are delivered along separate hollows in magnets. The two proton beams are separated by 192 mm in the arc, but it can be larger in straight sections depending on the requirements from the equipments used in the sections.

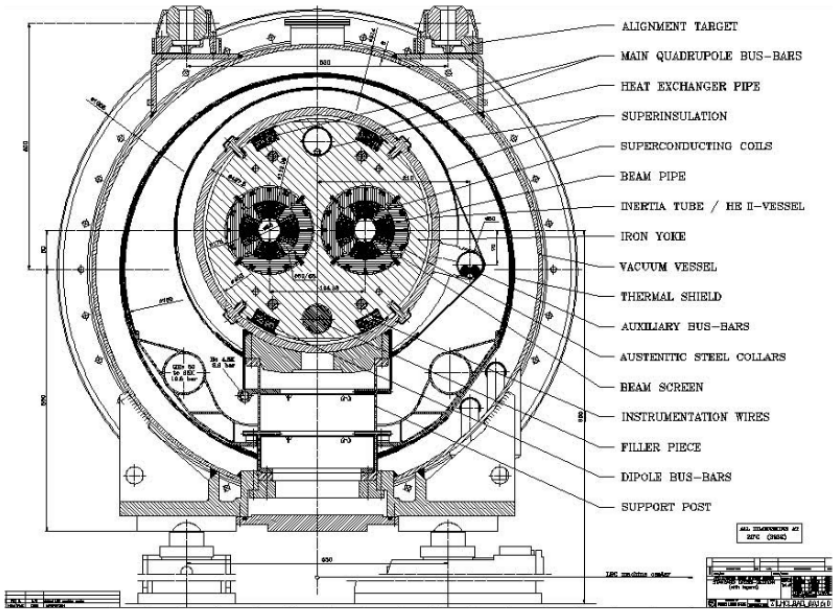

Figure 3.2: The schematic figure of the LHC dipole magnet [108].

The trajectory of the proton beams and their dispersion quality is controlled by magnets. The magnets are made of superconducting NbTi wires, of which the critical temperature and magnetic field are 9.2 K and 15 T. Most of the magnets are operated at 1.9 K to generate 8.33 T of magnetic field required for bending the trajectory of high energy proton beams along the arcs and focusing them at interaction points. The temperature setup also aims at utilizing high thermal conductivity of superfluid helium and temperature margins for stabler operation against a magnet quenching. Some components in the straight sections that do not require high field strength and cooling requirements are operated at 4.5 K.

Maintenance of high quality vacuum in the beam pipe is immensely important for the experiment. Collision between the protons in the beam and residual gas in the beam pipe produces cascades of secondary particle production, which not only reduces the beam intensity but also causes quenching of magnets due to energy deposits from them. The quenching of a magnet refers to the failure of magnet functions because of a phase transition to normal state from the superconductor state. The magnet quenching is dangerous for the machine because of both large magnetic energy stored and the energy of proton beam, hence it can result in dumping the entire beams. The gas density in the beam pipe is maintained below 10^{15} $H_2 m^{-3}$, when converted to corresponding hydrogen density considering the collision cross section, and even below 10^{13} $H_2 m^{-3}$ at the interaction regions.

Various precautions against the magnet quenching have been placed in the design of the machine. The beam screen is applied to intercept heat loads on the magnets from synchrotron radiation, image current, and nuclear scattering from the proton beam, and this shielding reduces the probability of quenching. In case of a quenching, it is important to protect the machine from a severe damage. To prevent localized damages from energy concentrated on the initial

quenching region, electric heaters are activated on the quenched magnet in order to artificially quench the entire magnet cell and limit the maximum increase in the temperature of magnet coils. In addition, cold diodes are installed in magnets, which provide bypass routes to external dump resistors when a quench occurs. The increase in the temperature of magnets lowers the turn-on voltage of diodes and activates the bypass route.

The proton beams, accelerated to a targeted energy at the RF cavities in the Octant 4, are made to cross at interaction regions for collision experiments. The delivered beams are oriented towards the interaction point using a dipole magnet and collimated using triple-low β quadruple magnets. These procedure reduce the RMS transverse beam size from 300 μm to 16.7 μm, for a β-function value of 0.55 m, at the interaction point where the two beams cross at an angle of approximately 285 μrad. Then the beam pass through a series of dipole and quadruple magnets to match the beam pipe on the opposite side and continues the cycle.

The beam intensity continuously decreases via various mechanisms and this determines the lifetime of the beam, defined as the time required for reduction of the intensity by a factor 1/e. The primary source of a beam loss is the proton-proton scatterings. Considering the total pp cross section of approximately 100 mb, this source contributes 29.1 h of the lifetime for a nominal luminosity of $10^{34}\mathrm{cm}^{-2}\mathrm{s}^{-1}$. The loss of a beam via scattering with residual gas in the beam pipe causes 100 h of the life time. Other sources arise from Touscheck effect and slow emittance blow-up from intra-beam scattering, non-linear beam-beam interaction, RF noise, scattering with residual gas, which add up to approximately 80 h of the life time. When combining these sources, the lifetime of a proton beam is expected to be approximately 14.9 h for an initial instant luminosity of $10^{34}\mathrm{cm}^{-2}\mathrm{s}^{-1}$.

When the beam intensity is decreased significantly, the beam is aborted to an external absorber at Octant 6. The protons pass through a series of magnets which deflect the beam horizontally and vertically to remove from the cycle. Then the proton beam is defocused by dilution magnets to avoid overheating the absorber. The beam ends on a carbon rod in a stainless steel jacket, surrounded by radiation shielding blocks.

3.1.2 Injection Chain

The protons used for the experiment are produced from the duoplasmatron at the Linear Accelerator 2 (LINAC2), which disassociates Hydrogen gas using thermal electrons. The resulting protons are accelerated to a kinetic energy of 50 MeV in bunches by a radio-frequency quadruple accelerator and passed to the Proton Synchrotron Booster (PSB), as shown in the Fig. 3.3.

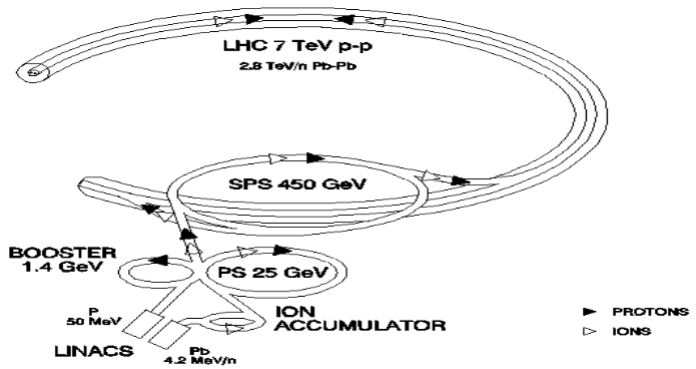

Figure 3.3: The schematic figure of the LHC injection chain [108].

The proton beams are accelerated to 1.4 GeV and stored at four rings of the PSB, each of which is operated at RF harmonic number (h) value of 1. The RF harmonic number (h), defined as the ratio of the RF voltage and the revolving frequency, determines the maximum number of bunches running in a circular

accelerator.

The next accelerator, Proton Synchrotron (PS), is operated at h=7, yet one slot is kept empty. Hence, six proton bunches are filled from the PSB in two batches, either 4+2 or 3+3 bunches. The empty space is intended for stable transfer of bunches to the next accelerator during the rise time of the ejection kickers. Such a mixture of filled and empty bunches on the harmonics are called the multiple splitting technique, and this scheme is used throughout the entire injection chain. Once the transfer from the PSB ends, the RF harmonic number of the PS is increased to 21, which divides the proton bunches in the six harmonic locations into 18 bunches. The proton beam energy is then increased to 25 GeV in the PS, and the RF harmonic number is increased by a factor of four. As a result of these procedure, 72 bunches will run on 84 harmonics on the PS, leaving the 12 consecutive empty slots, providing the enough time for stabilizing the ejector for the next accelerator, Super Proton Synchrotron (SPS).

The next accelerators of SPS and LHC do not divide the bunches again, yet only fills the beam line with the provided proton bunches with varying number of empty positions. Three or four batches of bunch trains from the PS fills the SPS, and the proton beam energy is boosted to 450 GeV. The proton bunches in the SPS then fills the LHC, with either 38, 39, or 119 empty bunches. The filling scheme of the LHC can be summarized as,

$$\begin{aligned} 3564 \; &= \{[(72b+8e)\times 3+30e]\times 2+[(72b+8e)\times 4+31e]\}\times 3 \\ &\quad +\{[(72b+8e)\times 3+30e]+81e\}, \end{aligned} \tag{3.1}$$

where b and e represent filled and empty bunches. Among the 3564 available bunch locations, 2808 locations are filled in the beam line of the LHC. The

proton bunches are spaced by 25 ns, each of which is 7.55 cm long (RMS) and contains 1.15×10^{11} protons, yielding the instant luminosity of 10^{34} cm^{-2}s^{-1} at the interaction points for the CMS and ATLAS Collaborations.

3.1.3 Performance

The thesis is based on data of pp collisions collected using the CMS detector at the interaction point 5 of the LHC during 2016. The proton energy was 6.5 TeV per a beam, hence, $\sqrt{s} = 13$ TeV. Due to the vacuum leak in the SPS dumping section, number of bunches were limited to 96 per a SPS batch, resulting in smaller number of bunches, 2220, in the LHC in 2016. On the other hand, when compared to the design, smaller β and emittance were achieved, and this lead to the higher peak instant luminosity of 1.5×10^{34} cm^{-2}s^{-1}. The integrated luminosity delivered by the LHC beam optics was 41.6 fb^{-1}, of which 38.3 fb^{-1} was recorded by the CMS detector. The difference between these two luminosity values originate from the deadtime of the CMS DAQ system, in which the trigger system is not ready to examine a new event.

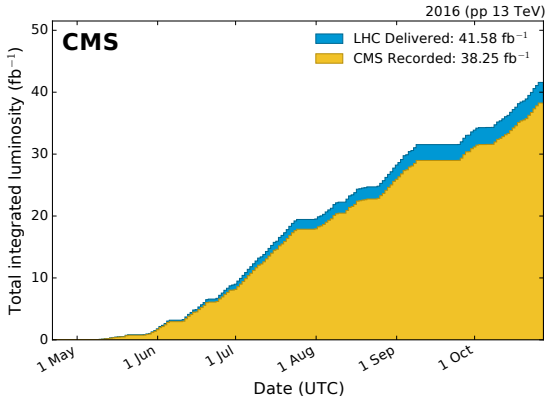

Figure 3.4: The integrated luminosity delivered by the LHC and the fraction recorded by the CMS detector [109].

3.2 Compact Muon Solenoid Detector

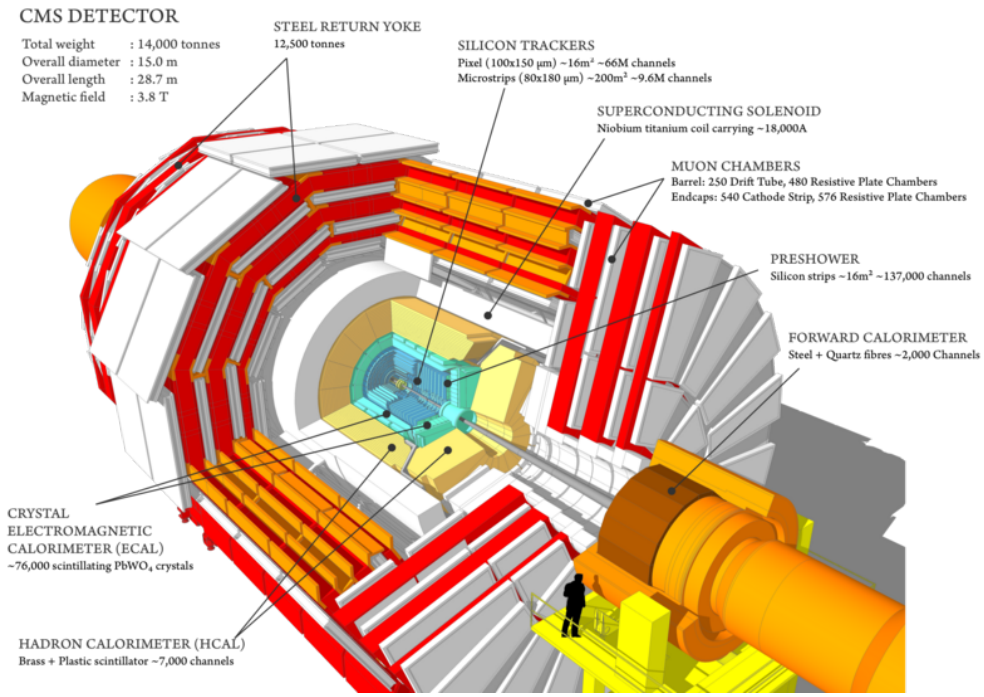

Figure 3.5: A schematic figure of the CMS detector [110].

The LHC is designed for collisions of proton bunches at a center-of-mass energy of 14 TeV, instant luminosity $10^{34}\text{cm}^{-2}\text{s}^{-1}$ with a 25 ns spacing. At this condition, approximately 1000 particles arise from 20 pp collisions at every bunch crossings occurring at 40 MHz. The experimental condition requires efficient and precise measurement of particles with transverse momentum (p_{T}) between a few GeV and TeV. At the same time, it should be robust against the additional pp collisions in the same bunch crossing and be able to operate sufficiently fast to cope with the bunch crossing rate.

The pp collision events performed at the interaction point 5 of the LHC

are studied with the Compact Muon Solenoid (CMS) detector. The detector is comprised of a inner tracking system, electromagnetic (ECAL) and hadronic calorimeter (HCAL) systems, a magnet, and a muon detection system, as shown in the Fig. 3.5. The detector is designed to identify charged leptons, photons, and hadrons with good efficiency and momentum resolution. The position resolution of inner tracking system is small enough to distinguish origins of charged particle tracks, for instance, such as additional pp collisions, decay vertices of B hadrons and τ leptons. In addition, precision and large coverage of the detector system allows the measurement of missing momentum via undetected particles which does not interact via electromagnetic or strong interactions. Optimal extraction of these information requires analysis of data from the entire detection system. In this section, the experimental apparatus and measurement from each detection component is explained.

3.2.1 Magnet

The CMS detector contains a solenoidal superconductor magnet, which lies between the HCAL and muon detector, approximately 3 m distant from the beam line. The magnet is 12.5 m long, 6 m wide in diameter, and 31.2 cm in thickness. It is made of 4-layer windings of NbTi coils in pure aluminum thermal conductor, mechanically reinforced with welding on aluminum alloys. The magnet is operated at 4.6 K, with approximately 1.8 K of a temperature margin from the critical temperature, to exploit its superconductivity. It produces magnetic field with a strength of 4 T at its center. The iron yokes inserted between muon detection system works not only as a hadron absorber, but also as a return route of magnetic field lines. Hence, despite a smaller strength when compared to the center, the magnet yields a significant field strength between 0.6–2.4 T at the muon detection system located on its outside as well. The map

of magnetic fields inside the CMS detector can be seen in Ref. [111]. In 2016, the magnet is operated at a central field strength of 3.8 T. The magnetic field plays one of the critical roles in the CMS detection system. The magnetic field bends trajectories of charged particles, and resulting curvatures provide precise information on their transverse momenta. The momentum of muons and charged hadrons are mainly determined in this approach.

3.2.2 Inner Tracking System

The inner tracking system is the first detectors that particles traverse in the CMS detection system, which lies between 0.044–1.1 m distant from the beam line. It is composed of a pixel detector in the innermost region and silicon strip tracker on its outside. They measure positions of charged particles in a number of detection layers, which is used to reconstruct the trajectory in the later stage. The layout of tracking system is shown in the Fig. 3.6.

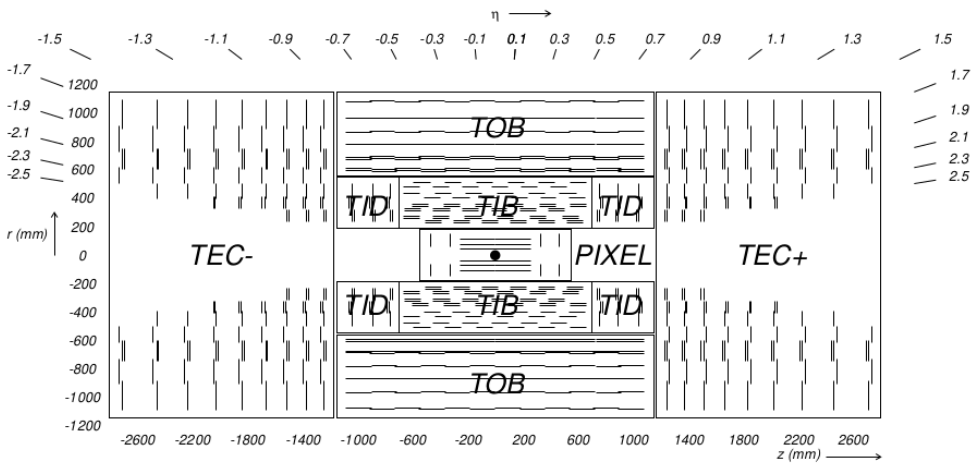

Figure 3.6: A schematic figure of the CMS inner tracking system [112].

Pixel Detector

The pixel detector consists of 3 layers at radii of 4.4, 7.3, and 10.2 cm for the barrel and 2 disks at $z = \pm 34.5$ and ± 46.5 cm on each sides of endcaps. The detector covers the pseudorapidity η between -2.5 and 2.5. The η is defined as $-\ln(\tan(\frac{\theta}{2}))$, where θ is the polar angle. The detector provides at least 3 hit positions in most of the detector coverage. Each layer of the detector is comprised of pixels with a size of $100 \times 150\,\mu$m, and there are 48 and 18 million pixels in the barrel and endcap layers, respectively. Because of the fine granularity, the detector occupancy is kept as small as 10^{-4} for the designed peak luminosity. The pixels provide 3 dimensional hit coordinates with a resolution of approximately $15\,\mu$m in each direction.

The high radiation dose at the inner tracking system causes damages increasing with the total exposure for an integrated luminosity. The main mechanism is the bulk damage on the silicon material by modification of the crystal lattice and band structures. This leads to a leakage current and gradual reduction of signals roughly by 10% for $500\,\mathrm{fb}^{-1}$ running. The leakage current can lead to self heating with a positive feedback, known to exponentially dependent on the temperature. To minimize such effects, the entire tracking system is operated at $-10°$C using the coolant of C_6F_{14}.

Silicon Strip Tracker

Outside the pixel detector, silicon strip trackers are located at radii between 20 and 116 cm and axial distance below 282 cm. The barrel region between radii 20 and 55 cm are covered by Tracker Inner Barrel and Disks (TIB/TID). The TIB and TID consists of 4 coaxial and 3 disk layers of silicon strips. From the radii 55 cm, Tracker Outer Barrel (TOB), 6 coaxial layers of silicon strips, is

located. From the axial distance between 124 and 282 cm, Tracker EndCaps (TEC), 9 disk layers of silicon strips, are located on each side. The size of strips vary between 11.7 and 20.2 cm for the length and between 80 and 205 μm for the pitch. These layers of silicon strips provide roughly 10 hit positions along the particle trajectory, of which four and six positions are 3- and 2-dimensional measurement, respectively. The hit positions are measured with a resolution of 23–53 μm for the 2-dimensional locations and 230–530 μm for the third dimension. From the measured track hits, a track can be reconstructed with approximate resolutions of 1%, 15 μm, and 30 μm for p_{T}, transverse, and longitudinal impact parameters, for a muon in a p_{T} range of 10–100 GeV.

The locations of tracker components can be changed during the experiment because of thermal contraction from cooling and mechanical stress from magnetic fields. The shifts are constantly monitored for a selected number of layers using a laser alignment system during both the runs for calibrations and the runs for the physics analysis. In addition, a cosmic muon data is used for the calibration of entire tracking system. The relative location of detector components are constrained with an uncertainty of roughly 60 μm and 80μrad.

The material budget of the inner tracking system corresponds to 0.4–2 radiation lengths (X_0) and 0.12–0.56 nuclear interaction lengths (λ_I), varying with η values. Approximately 35% of electrons lose more than 70% of their energy by bremsstrahlung in the tracker, thus changes in track parameters due to electromagnetic radiation must be considered in the track reconstruction of electrons and the momentum measurement is complemented with the calorimetric measurements. On the other hand, the bremsstrahlung of muons or charged hadrons are negligible in the tracker and their tracks can be reconstructed with simpler methods. In case of hadrons, the nuclear interaction length is not completely ignorable and causes roughly 10% of inefficiency in a track reconstruction.

3.2.3 Electromagnetic Calorimeter

On the exterior of the inner tracking system, electromagnetic calorimeters (ECAL) are placed. It measures the lost energy of charged particles via scintillation lights in the system. Lead tungstate ($PbWO_4$) crystals are used for the scintillator. The ECAL barrel (EB) includes 61200 crystals with a size of approximately 0.0174×0.0174 in η-ϕ or $22 \times 22\,\mathrm{mm}^2$, and a length of 23 cm ($25.8\,X_0$), covering $|\eta|$ values below 1.479. For $|\eta|$ value from 1.479 to 3, the ECAL Endcaps (EE) cover with 3662×2 crystals with a size of $28.62 \times 28.62\,\mathrm{mm}^2$ and a length of 22 cm ($24.7\,X_0$). Electrons and photons develop 90% of their shower in scintillators within a lateral length of 2.2 cm (Moliere radius), and the granularity of crystals is sufficiently fine for analyzing the shower shape. The scintillation decay time in the lead tungstate is 10 ns, and 80% of scintillation light is emitted within 25 ns. The wavelength of the scintillation light varies in 350–600 nm, with a peak at around 430 nm. The ECAL system is operated at a constant temperature of 18 °C using water cooling system to maintain the energy resolution.

The scintillation lights are detected with avalanche photodiodes (APD) in EB and vacuum phototriodes (VPT) in EE. The different types of photodetectors in EB and EE are motivated from difficulties with high magnetic fields for vacuum-based devices in EB and high expected radiation damages for solid-state devices in EE. Each APD in EB has a sensor area of $5 \times 5\,\mathrm{mm}^2$, and they are operated at a gain of 50 and a quantum efficiency of 75% for a wavelength of 430 nm. On the other hand, each VPT has a diameter of 25 mm with an active area of roughly $280\,\mathrm{mm}^2$. They operate at a gain of roughly 10 with a quantum efficiency of 22%. The quantum efficiency of VPT is lower compared to the APD, yet the difference is largely compensated by its larger active area.

For the η range in 1.653–2.6, a preshower detector is located to achieve a better resolution in early shower developments and distinguish a collimated pion decay, $\pi^0 \rightarrow \gamma\gamma$, from a single photon. The preshower consists of two layers of lead radiators with a thickness corresponding to $2X_0$ and X_0, and two layers of silicon strip sensors located behind each of the lead radiator with mutually orthogonal strip directions. Each preshower unit measures an area of $61 \times 61\,\mathrm{mm}^2$ with 32 strips on each layer. Within the first lead radiator, 95% of photons start showering and the charge-weighted-average location of energy deposits in strip sensors provide a position resolution of $\approx 300\,\mu\mathrm{m}$.

Optical properties of crystals change with the exposed radiation dose. Radiation causes vacancies and impurities in the crystal lattice, resulting in development of color centers and absorption bands. This reduces the transparency of crystals by wavelength-dependent magnitudes. Hence, the transparency of crystals are regularly monitored and calibrated using a laser monitoring system during beam gaps of the experiment. In addition, using the energy deposit of cosmic muons on crystals, $\approx 250\,\mathrm{MeV}$ for maximal traversing, calorimetric measurements are calibrated using the cosmic muon data set. Finally, in-situ calibrations are also applied using the portion of data set with $\pi^0/\eta \rightarrow \gamma\gamma$, $\mathrm{W} \rightarrow \mathrm{e}\nu$, and $\mathrm{Z} \rightarrow \mathrm{ee}$.

The resolution of calorimetric measurements can be parameterized as [112],

$$(\frac{\sigma_E}{E})^2 = (\frac{S}{\sqrt{E\,/\,\mathrm{GeV}}})^2 + (\frac{N}{E\,/\,\mathrm{GeV}})^2 + C^2, \tag{3.2}$$

where σ_E, S, N, and C are the absolute E resolution, the stochastic term, the noise term, and the constant term, respectively. For the stochastic term of ECAL, $S \approx 2.8\%$, fluctuations in number of emitted photoelectrons in the photodetectors typically gives the largest contribution, $\approx 2.1\%$, but fluctuations in the difference between energy loss in the preshower and measured value from

silicon sensors can be the leading source for a few GeV scale energy deposits in endcaps. The noise term, $N \approx 12\%$, originates from electronics and digitization procedure, with a magnitude of roughly 40 MeV/channel. The constant term, $C \approx 0.30\%$, is attributed to non-uniform light collection and calibration error. This leads to the energy resolution of roughly 1% at 20 GeV and 0.4% beyond 50 GeV.

3.2.4 Hadronic Calorimeter

Hadronic Calorimeter (HCAL), located outside the ECAL, aims to measure energy of hadrons lost in the calorimeter via hadronic shower. The HCAL system consists of HCAL Barrel (HB), HCAL Endcap (HE), HCAL Outer Barrel (HO), and HCAL Forward (HF). The HB and HO covers the hadron flux in a $|\eta|$ region below 1.3, where HB stretches from ECAL (R=1.77 m) to the magnet (R=2.95 m) and HO is placed between the magnet and muon detection system (R=4.07 m). The HE and HF span the $|\eta|$ region of 1.3–3.0 and 3.0–5.0, respectively.

The HB, HE, and HO are typical sampling calorimeters. The HB consists of 16 absorber layers of brass plates, except 2 steel plates at the innermost and outermost layers, and 17 scintillator layers of plastic plates. The first scintillator layer is placed between EB and HB to detect a hadronic shower developed before the HCAL. The thickness of HB varies in 5.82–$10.6\lambda_I$, increasing with $|\eta|$, and that of ECAL is about $1.1\lambda_I$. The containment of hadronic shower in HB is not sufficient, hence HO is placed outside the magnet to complement this. The HO uses magnet materials and the first layer of iron yokes in the muon system as absorbers, and two layers of scintillators are placed on both side of the first iron yoke layer. By inclusion of the HO, the depth of total calorimetric system increases to values larger than $11.8\lambda_I$. The HE structure is similar to HB, which

is made of 17 layers of brass absorber and plastic scintillator plates. The depth of total calorimetric system in the HE is around $10\lambda_I$. The size of calorimetric tiles in η-ϕ, corresponding to the HCAL granularity, is 0.087×0.087 in HB and HO, and it varies between 0.087×0.087 and 0.178×0.178 in HE.

The scintillation lights in the HB, HE, and HO are sampled using wavelength shifting (WLS) fibers, which are connected to optical fibers at the lateral surfaces of trigger towers, and the optical fibers deliver the sampled scintillation lights to the photodetectors. Hybrid photodiodes (HPD) are used for the photodetectors, operated with a gain of ≈ 2000.

The design of HF is different from other HCAL components because of extreme particle flux and weaker magnetic fields. The HF consist of cylindrical steel absorbers with inserted quartz fibers. Charged hadrons produced from a hadronic shower in the absorber yield Cherenkov lights in the quartz fibers. Cherenkov lights, produced with an angle larger than the critical angle of total internal reflection, are transmitted to the end of the fiber and eventually guided to photodetectors using subsequent optical fibers. Half of the quartz fiber penetrate the full length of the absorber, and the other half starts 22 cm distant from the front face of the absorber to distinguish later development of shower. Thickness of the absorber is 165 cm, corresponding to roughly $10\lambda_I$. As the particle fluence after the absorber is not ignorable, the photodetectors are put in read-out box shielded with 42.5 cm of steel, lead, and polyethylene layers. The fibers are bundled to form a tower with a size of 0.175×0.175 in η-ϕ, the designed granularity in HF.

The relative resolution of energy measurement from HCAL can be parameterized with the same formula in the ECAL (Eq. 3.2). The stochastic coefficient S is approximately 100% for HB+HO and HE, and 200% for HF [113]. The constant term C is approximately 5% for HB+HO and HE, and 3% for HF.

The magnitude of stochastic uncertainty is naturally much larger in the case of HCAL, when compared to that of ECAL, as the calorimeter samples only a portion of the hadronic shower and the energy of an original hadron is inferred from it. Depending on the fraction of electromagnetic components in each hadronic shower and also the fraction of energy released or arrived in the scintillator, the estimation error increases especially in cases of low energy hadrons.

3.2.5 Muon Detection System

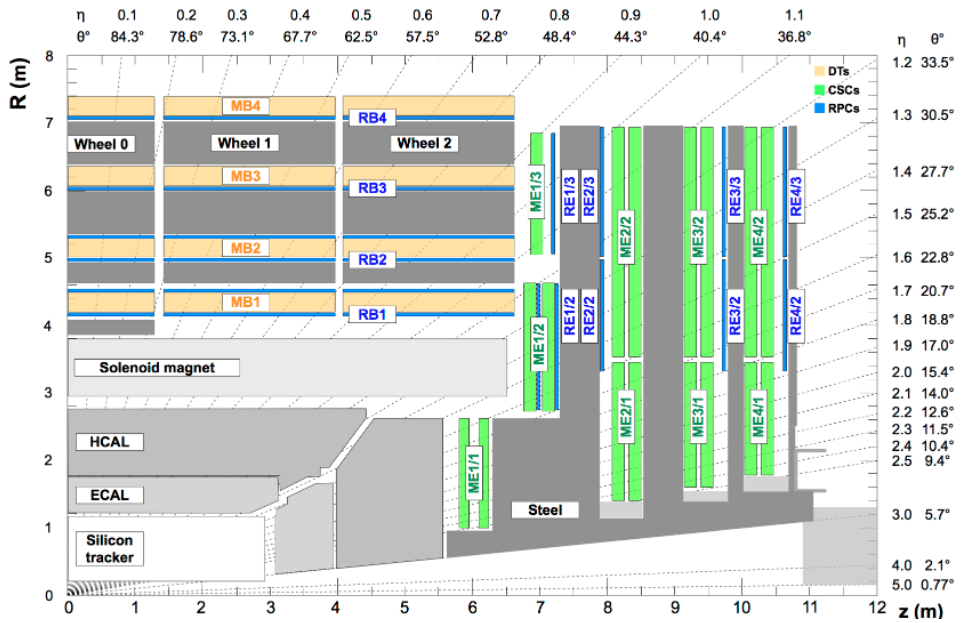

Figure 3.7: A schematic figure of the CMS muon system [114].

The muon detection system is located outside the magnet and HCAL. It is comprised of 3 gaseous detectors of drift tube chambers (DT), cathode strip chambers (CSC), and resistive plate chambers (RPC). These detectors have layered structures, in between which are filled with iron yokes. The iron yokes provide a return route for magnetic fields, yielding 0.6–2.4 T of field strengths

outside the solenoid, bending muon trajectories. In addition, the iron yokes have a role of hadron absorber and form a low-background environment for the muon system. Thickness of materials inside the muon system is 11-15λ_I and 20–27λ_I for the first and last detection layer, respectively. Each layer of muon detection system measures segments of muon tracks, location and direction of them, and combination of these segments produces reconstructed muon tracks in the muon system. The layout of muon detection system is shown in Fig. 3.7.

The DT consists of 4 layers of chamber groups, called stations, and covers $|\eta|$ range of 0–1.2. Each of the stations is made of 2 or 3 superlayers (SL), each of which is formed by 4 consecutive layers of drift cells. The drift cells, the smallest unit, is made of 5 electrodes, 1 anode wire, 2 field shaping strips, 2 cathode strips, and filled with Ar/CO_2 gas (Ar:85%+CO_2:15%). Wires of two SL are parallel to the beam line and they are used for reconstructing track segment in the r-ϕ plane. Those of the third SL, if exists, is placed orthogonal to the others and measures the z-component of tracks. As the fourth station does not have the third SL, the z-component is not measured in the last DT station. Each DT station reconstruct muon track segments with a time and spatial resolution of 2 ns and 100 μm.

Muons in the high $|\eta|$ regions are detected with CSC, which stretches across $|\eta|$ region of 0.9–2.4. The $|\eta|$ range 0.9–1.2 is an overlapping region between DT and CSC, and both detector are used for measurement. The CSC is made of trapezoidal multiwire chambers, each of which consists of 6 anode wire planes and 7 cathode strip planes, filled with a mixture of Ar+CO_2+CF_4 gas. Wires run in azimuthal direction, and the strips stretches radially. Hence, the wires provide information on radial coordinates of the hit positions and the strips provide their azimuthal coordinates. Each CSC station reconstructs muon track segments with a time and spatial resolution of 3 ns and 50–140 μm.

The last component of the muon system, RPC, is installed in the $|\eta|$ range of 0–1.9 in 2016. The RPC is made of two parallel-plate chambers, each of which are made of two electrodes of bakelite-graphite plates and filled with a mixture of $C_2H_2F_4$+C_4H_{10}+SF_6 gas. Between the two chambers, copper strips are placed for the read-out. Six layers of RPC are installed in DT, 2 and 1 layers per a station for the first and last two stations, respectively. In CSC, each station includes only one RPC layer, up-to the designed $|\eta|$ value. Additional RPC layers in the first two barrel stations were intended for increasing hit information for the trigger on low-p_{T} muon tracks, which may not reach the last station. The RPC system provides information on the hits with a spatial and time resolution of 0.8–1.3 cm and 1.5 ns. Despite the significantly worse spatial resolution, RPC exhibits the best time resolution of tracks, hence it is installed mainly for purposes of precise timing and fast triggering.

Track segments detected in the muon system can be combined to reconstruct muon tracks. The relative resolution of muon p_{T} is approximately 10 and 20% in the barrel and endcaps, respectively, for the p_{T} between 10 GeV and 1 TeV. In offline analysis, the muon tracks are reconstructed using the both track hits in the inner tracking system and the track segments in the muon system. The same resolution of a track from inner tracking system is about 1–2% for p_{T} below ≈ 100 GeV and increases to $\approx 10\%$ at 1 TeV. Hence, the p_{T} resolution is mainly determined by inner tracking system for low p_{T} values below 200 GeV, and the information from the muon system significantly improves the track parameter resolutions for high p_{T} region beyond the 200 GeV. The muon p_{T} resolution is better than 5 and 10% for the barrel and endcap regions for the combined track fit from the inner tracker and muon systems.

3.3 Trigger

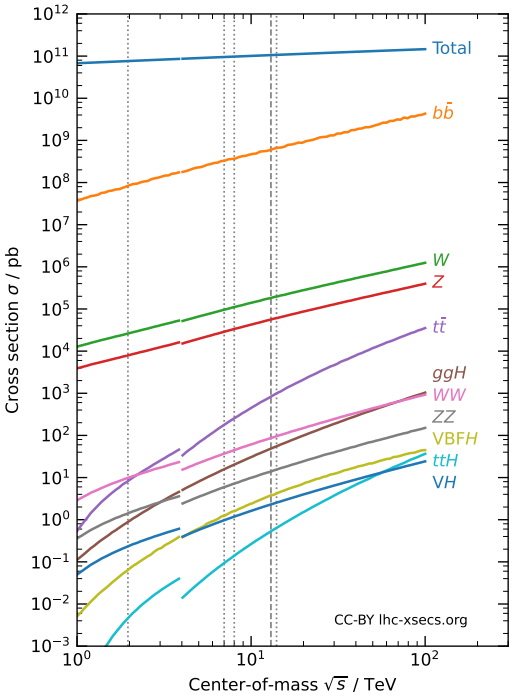

Figure 3.8: pp cross section for various processes [115]. For $\sqrt{s} < 4\,\text{TeV}$, $p\overline{p}$ cross section is shown. Dotted lines are placed at 1.96, 7, 8, and 14 TeV, and a dashed line is place at 13 TeV.

Total pp cross section is approximately 100 mb, however that of processes of interests in the LHC program, electroweak bosons, $t\bar{t}$, and Higgs bosons, are smaller by a factor of $10^{-6} - 10^{-10}$, as can be seen in Fig. 3.8. It would be extremely inefficient to allocate storage and computing resources on processing entire collision events. Thus, a tiered trigger system is adopted to populate the events in the DAQ output with a high likelihood of processes of interests. Hardware-based Level-1 (L1) trigger operates in a latency of 4 μs and reduces output rate from 40 MHz to approximately 100 kHz. Then the software-based

High Level Trigger (HLT) in a computing facility in CERN examines the events selected by the L1 trigger and further reduces the output rate to around 1 kHz. Each event includes approximately 1.5 MB of data, and the CMS produces and records pp collision data at a rate of $\approx$ 1.5 GB/s. The trigger system allows 4×10^4 times faster acquisition of target physics data within a limited rate of processing and storage.

3.3.1 Level-1 Trigger

Most of the L1 trigger algorithms are based on simple detector signatures, such as p_{T} and η of calorimeter deposits. Due to the tight time budget, only the calorimeter and muon system is used in the L1 trigger system. The trigger consists of local, regional, and global components. Local components, called trigger primitives (TP), are energy deposits in a region of calorimeters or track segments in stations of muon chambers. Regional components collect TPs sent from the on-detector electronics and combine them to reconstruct objects or variables of interests, such as muon, e/γ, jet, and the imbalance of transverse energy. The global component collects and combines the information from regional components, and makes decisions to accept the event. The architecture of the L1 system is shown in Fig 3.9.

A muon track is reconstructed with different algorithms for barrel and endcaps. In the barrel region, RPC hits are merged into DT TPs in the same layer. Using the predefined patterns in look-up tables (LUT), an acceptance window of segments in the adjacent chambers or layers from a same track is defined for each segments. Such segments are grouped to form a muon track, being one of the patterns in the LUT. The p_{T} value is determined to the LUT value corresponding to the internal bending angle and azimuthal angle difference between the nearby segments. Muon tracks in other detector region are

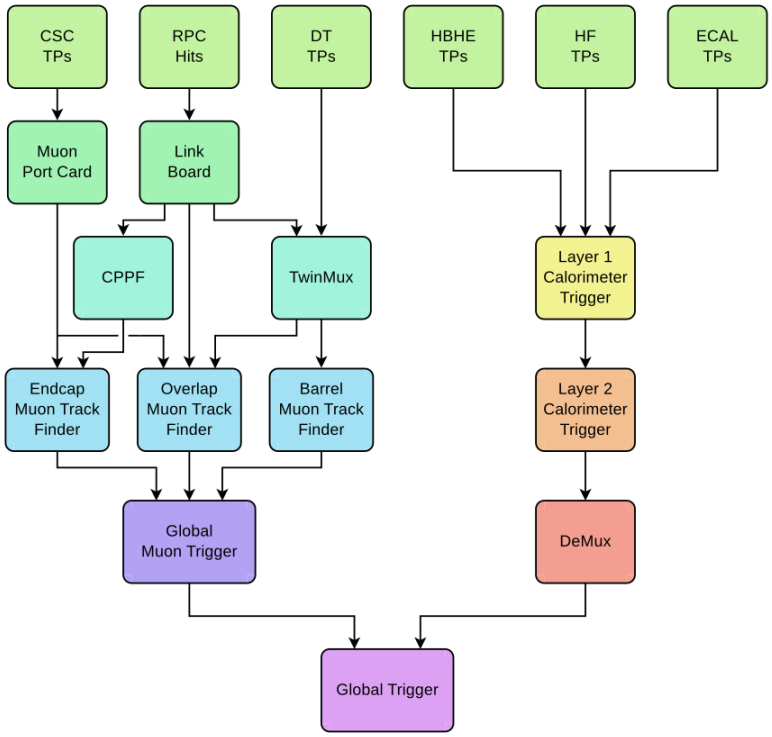

Figure 3.9: A schematic figure of the architecture of L1 triggers [116].

also reconstructed using LUT, but with different input measurements. Muons in the overlap region between the DT and CSC, 18 total measurements from 3 DT TP + 5 RPC hits in the barrel and 4 CSC TP + 3 RPC hits in the endcap are used to build tracks. In endcap region, at most one TP per station, either CSC or RPC TP, is used to build a muon track. The p_{T} assignment is different in endcaps, because of much larger changes in the magnetic field in the endcap region, when compared to the barrel region. A boosted decision tree (BDT) regression technique is used to estimate p_{T} value of a track. The p_{T} value estimated by a BDT regressor for each track pattern is stored in LUT, and these values are used by the trigger algorithms. The muons are assigned a value for its quality, based on the hit patterns, such as number of hits in a track with a larger weight to an inner detection layers. Up-to 36 muon candidates per each of barrel, overlap, and endcap regions are sent to the global muon trigger. The global muon trigger identifies and removes duplicate candidates among these. Then it first sorts out 8, 4, and 4 tracks with a best quality from barrel, overlap, and endcap regions, respectively. Among these up to 8 best muon candidates are sent to the global trigger.

Rest of L1 trigger algorithms are based on calorimeter deposits. The smallest unit of calorimeters in the trigger algorithm is a trigger tower (TT), comprised of 5×5 ECAL crystals in EB and HCAL plates behind them, covering 0.087×0.087 in η-ϕ. In endcap, each TT approximately corresponds to an area of 0.17×0.17 in the η-ϕ plane. These TTs form TPs for the calorimeter-based algorithms. The TT energy is corrected for the changes of calorimeter response over time and average energy loss in the tracker material.

The e/γ object in the L1 trigger is reconstructed by summing up energy deposits around a seed TT with E_{T} larger than 2 GeV, as shown in the Fig. 3.10. For the e/γ object with E_{T} below 128 GeV, they are distinguished from back-

grounds using additional criteria, such as the compactness of energy deposits in each crystal in the seed TT and the H/E ratio of the seed TT. The isolation variable, the energy deposit in the region surrounding the object (Fig. 3.10), is also calculated to reject background. The isolation is corrected for the pile-up contribution estimated using the number of TT with E_{T} larger than 0.5 GeV.

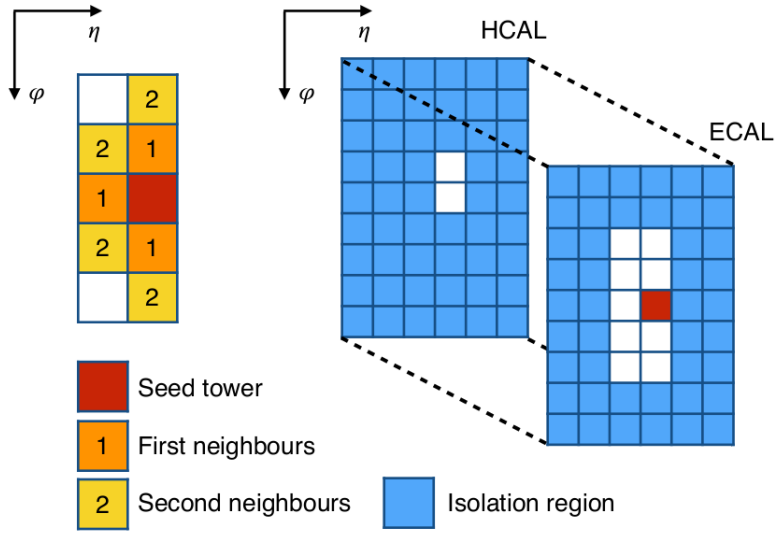

Figure 3.10: The clusters of TTs in the L1 e/γ object and the isolation region [116].

Jets in the L1 trigger is defined as the energy deposits in a 9×9 TT cluster centered at a seed TT with $E_{\mathrm{T}} > 4$ GeV. The size of clusters approximately matches the cone size of jets in offline analysis. Expected pile-up contributions are subtracted using the sideband TT, four 3×9 TTs in each of η and ϕ directions. There are also many other algorithms targeting different signatures, such as hadronic tau leptons and imbalance in the transverse energy, and more details on these can be found in Ref. [116].

The global trigger makes decisions using the information sent from the re-

gional triggers. The decisions are based on cuts on p_{T}, η, and quality codes. The trigger algorithms used for the analysis require two muon or electron-muon objects. Dimuon algorithms accept events if p_{T} values of two muons are larger than 11-4, 12-5, or 13-6 GeV for the first-second muons. On the other hands, electron-muon algorithms accept events if trigger objects include a muon with p_{T} larger than 5 GeV and any electron with p_{T} larger than 20 or 23 GeV or an isolated electron with p_{T} larger than 18 or 20 GeV. The thresholds vary with the period and the instant luminosity.

3.3.2 High Level Trigger

The HLT receives the fragmented data of various detectors sent from the DAQ and combine them to a complete event. These are used for event reconstruction and trigger decisions. The HLT uses full granularity of detector components, and its selection criteria is comparable to those of offline analysis. As many of descriptions overlap with the offline analysis, only a brief overview of algorithms related to the thesis is introduced in this section, and the details will be explained in the next chapter.

In addition to the increased detector granularity and complexity of variables, HLT uses inner tracking information to reconstruct tracks and vertices. The primary vertex (PV) in the HLT is reconstructed using only the pixel tracks, comprised of 3 hits in pixel layers, and a fast PV finding algorithm is used to satisfy the limited time budget. In this faster algorithm, a jet collection with $E_{\mathrm{T}} > 40$ GeV is searched, and pixel tracks associated with these jets are projected on to the beam line and clustered along z-axis to form vertices. If such a vertex is not found, then all pixel tracks in the detector are analyzed by clustering their beamline projection. With this approach, vertices can be found with efficiency smaller by $\approx 8\%$ than offline reconstruction efficiency.

Electron algorithms begins with reconstruction of ECAL deposits from the EM showering, called the supercluster (SC), around L1 electrons. Superclusters are required to satisfy certain criteria on the quality. For the isolated electron algorithm used in the thesis, energy-weighted s.d. of η locations of crystals in superclusters should be less than 0.013 (0.035) in EB (EE). HCAL deposits relative to SC E_{T} within $\Delta R = \sqrt{(\Delta\eta)^2 + (\Delta\phi)^2} < 0.15$ from the SC center should be less than 0.13. ECAL and HCAL deposits relative to SC E_{T} within $\Delta R < 0.3$ from the SC center are required to be less than 0.5 and 0.3, respectively, after subtracting the SC E_{T} and mean expected pile-up contribution.

If a SC satisfying the quality criteria is found, then inner tracking data is examined. From the SC position and energy, compatible pixel hits are searched. If such hits are found, then a full electron track is reconstructed using the silicon tracker with considering energy loss via bremstrahluing using Gaussian Sum Filter (GSF) algorithm. The track is examined if it satisfies quality criteria of the algorithm. For the electron-muon trigger used in the analysis, spatial difference between the SC and extrapolation from the innermost track position is required to be less than 0.01 (0.015) for η and 0.07 (0.1) for ϕ in EB (EE). In addition, the scalar p_{T} sum of other tracks within $\Delta R < 0.3$ from the SC is required to be less than 20% of the SC E_{T}.

On the other hand, muon algorithms consist of Level-2 (L2), using only the muon system, and Level-3 (L3) stages, using inner tracking systems as well. The L2 step starts from reconstructing muons in the muon system around the L1 muons. If quality criteria of algorithms are met, then these muons are used as seeds for the next step. In the L3 step, hits in the inner tracking system compatible with the L2 muon is searched and a track is reconstructed. If the track reconstructed from the inner tracking system is compatible with the L2 muon at their boundary, the inner most layer of the muon system, all mea-

surements from the muon and inner tracking systems are refit to construct a L3 muon track. In addition, for dimuon triggers, a different reconstruction is also used for lower-p_{T} muons, considering their smaller number of hits in the muon system. In this case, a track in the silicon tracker with one or more compatible segments in the muon system is also reconstructed as a L3 muon. The dimuon trigger algorithm used in the analysis requires presence of at least one L2 muon with $p_{\mathrm{T}} > 10\,\mathrm{GeV}$, and two L3 muons with p_{T} larger than 17 and 8 GeV. The electron-muon trigger algorithm in the thesis requires a L3 muon with $p_{\mathrm{T}} > 8\,\mathrm{GeV}$, yet this L3 muon should be seeded by a L2 muon with $p_{\mathrm{T}} > 5\,\mathrm{GeV}$, in contrast with absence of a p_{T} cut for the subleading muon in the former case. For both algorithms, the scalar p_{T} sum of tracks surrounding the L3 muon within $\Delta R < 0.3$ should be less than 40% of the muon p_{T}, and the closest distance between the two leptons in the z-coordinate is required to be less than 0.2 cm in later runs of 2016.

3.4 Luminosity Measurement

The integrated luminosity delivered to and recorded by the CMS detector is measured using 7 detector systems [117]. Each measurement is based on either the rate-scaling or zero-counting method. The former method measures detector activity and infers the luminosity from it. The average instant luminosity for a single bunch, L_b, can be written as,

$$L_b = \overline{N}_{int}\frac{f_{rev}}{\sigma} = (\frac{\overline{N}_{obs}}{\overline{N}_{obs/int}})\frac{f_{rev}}{\sigma} \equiv \overline{N}_{obs}\frac{f_{rev}}{\sigma_{vis}}, \tag{3.3}$$

where $\overline{N}_{int}$, $\overline{N}_{obs}$, and $\overline{N}_{obs/int}$ are respectively the mean number of pp collisions, observables, and observables per single pp collision. The f_{rev} and σ are the LHC revolution frequency and the pp cross section. The σ_{vis} absorbs the

acceptance factor for the detector coverage and dead cells, and it is measured by a separate experiment. With known values of σ_{vis} and f_{rev}, the L_b can be calculated from a measurement of detector observables, and accumulation of single bunch luminosity for the whole runs yield the integrated luminosity value.

On the other hand, the zero-counting method estimates the L_b from the fraction of events without any detector signal. This method avoids systematic uncertainty from multiple particles falling in the same detector cell. Assuming the Poisson probability distribution, this fraction $\bar{f}_0$ can be represented as,

$$\bar{f}_0 = \sum_{k=0}^{\infty} \frac{e^{-\mu}\mu^k}{k!} p^k = e^{-\mu(1-p)}, \tag{3.4}$$

where p is the probability of absent detector signals for a pp collision, μ is the mean number of pp collisions, and the summation runs over number of pp collisions. Then the L_b can be related to the $\bar{f}_0$ by,

$$L_b = \frac{\mu f_{rev}}{\sigma} = -\frac{\ln \bar{f}_0}{(1-p)} \frac{f_{rev}}{\sigma} = -\frac{f_{rev} \ln \bar{f}_0}{\sigma_{vis}}. \tag{3.5}$$

Hence, the L_b can be estimated from counting number of events with and without detector signals in this approach.

The fiducial total inelastic pp cross section σ_{vis} is measured during the van der Meer (vdM) scan [118, 119]. For numbers of protons n_1 and n_2 in two incoming bunches and their effective overlapping area A_{eff}, the single bunch luminosity L_b can be formulated as,

$$L_b = \frac{f_{rev} n_1 n_2}{A_{eff}} = f_{rev} n_1 n_2 \iint \rho_1(x,y)\rho_2(x,y)\, dx\, dy, \tag{3.6}$$

where ρ_i is the 2-dimensional density function. Assuming the factorizability, $\rho_i(x,y) = f_i(x)g_i(y)$, the A_{eff} can be expressed as $A_{eff} = W_{eff}H_{eff}$, where

the effective width and height, W_{eff} and H_{eff}, are defined as,

$$\frac{1}{W_{eff}} \equiv \int f_1(x) f_2(x)\, dx\,, \; \frac{1}{H_{eff}} \equiv \int g_1(y) g_2(y)\, dy. \tag{3.7}$$

These can be reformulated as,

$$\begin{aligned} W_{eff} &= \frac{\iint f_1(x) f_2(x-w) dx dw}{\int f_1(x) f_2(x) dx} = \frac{\int L_b(w,0) dw}{L_b(0,0)} \\ H_{eff} &= \frac{\iint g_1(y) g_2(y-h) dy dh}{\int g_1(y) g_2(y) dy} = \frac{\int L_b(0,h) dh}{L_b(0,0)}, \end{aligned} \tag{3.8}$$

where $L_b(w,h)$ is the luminosity for two beams displaced by w and h in x and y directions. The luminosity profile can be obtained from fitting event rates with different bunch displacement in x-y directions. Integration of these functions yields the two length scales, i.e. the effective area A_{eff}. On the other hand, the number of protons n_1 and n_2 are extracted from a beam current measurement using the DC current transformer and fast beam current transformer [120, 121]. Then, by relating the Eq. 3.6 with Eq. 3.3 or 3.5, the σ_{vis} value can be obtained.

In the CMS experiment, the σ_{vis} is measured in separate runs with lower instant luminosity to minimize uncertainty. During the runs for the vdM scanning, the mean pile-up number was approximately 0.6 with a number of bunch per beam of 30–50 and transverse beam size of 100 μm. The large bunch spacing is intended to minimize afterglows and the larger bunch size dilutes the impact of vertex reconstruction resolution from the tracker, which is about 10 μm. The scanning is performed for beam separations up-to 600 μm ($\approx 6\sigma_b$) in 25 steps of 30 seconds for both x and y directions.

In the vdM scanning, various observables from different detectors sensitive to the luminosity are monitored. Using the inner tracking system, the number of pixel hit clusters (PCC), composed of 5 pixel hits, and number of reconstructed primary vertices (PVC) from the inner tracking system, requiring at

least 11 tracks per a vertex, are analyzed. For the HF calorimeter, the detector occupancy, HFOC, of outer two rings ($\Delta\eta \approx 0.5$) is used for the scanning. In addition, two luminometers of pixel luminosity telescope (PLT) and beam condition monitor (BCM1F), located at $|\eta| \approx 4.2$, are also used to measure the luminosity. The PLT consists of 48 silicon pixel sensors in 3 layers and counts the triple coincidence in these layers. The BCM1F consists of 24 single crystal diamond sensors and have time resolution of 6.25 ns, enough to distinguish collision and beam-induced signals. During the vdM scanning, the PCC and PVC data is analyzed with the rate-scaling method, and the HFOC, PLT, and BCM1F data is interpreted with the zero-counting method. The results from several luminometers were observed to be consistent, and the σ_{vis} value of several detectors are determined with an uncertainty of 1%.

Using the measured σ_{vis} values, the same kinds of detector activities as in the vdM scanning are also used in determination of integrated luminosity of physics runs. In addition, the DT and RAMSES systems are deployed to test linearity against luminosity and stability over time in the data-taking period. RAMSES, an abbreviation for the RAdiation Monitoring System for the Environment and Safety, consists of 10 ionization chambers filled with air at 1 atm. It was originally installed for ensuring the safety of personnel working at the cavern, but its data has shown good linearity for the beam luminosity and stability over time, hence it was determined to be used as an additional measurement to constrain uncertainty in the integration of bunch luminosity values. The stability is tested by monitoring data during regular detector calibrations and cross-detector comparison in entire data set. As a result, the integrated luminosity is determined to be $41.6\,\mathrm{fb}^{-1}$ for the delivered value, $38.3\,\mathrm{fb}^{-1}$ for the amount recorded by the CMS detector, and $35.9\,\mathrm{fb}^{-1}$ for the recorded amount in which all detector conditions were checked to be normal.

Chapter 4

Data Analysis

4.1 Data Sets and Simulation

4.1.1 Data Sets

The thesis is based on the analysis of pp collision data collected with the CMS detector in 2016. The data collected with a list of unprescaled dilepton triggers in Table 4.1 are used for the search. To avoid double counting, events with electrons passing identification criteria of the analysis are selected with electron-muon triggers, and events with only muons passing identification criteria of the analysis are selected with dimuon triggers. Dilepton triggers without DZ filters are used for earlier runs, and those with DZ filters are used for the later runs. Among the collected data, only the good quality events with all detectors flagged normal are used, in which corresponding integrated luminosity is $35.9\,\mathrm{fb}^{-1}$.

For the measurements of parameters required for estimation of jet-induced fake lepton background, prescaled single lepton triggers with similar sequences

and filter requirements to those in dilepton triggers for the analysis are used. Normalization for these paths are obtained from a sample enriched with W boson events and double checked in a sample enriched with Z boson events. Details are described in Section 4.6.1 on the background estimation. For the measurement of identification and trigger efficiencies of prompt leptons in real data, unprescaled or partially unprescaled single lepton triggers and dilepton triggers without DZ filters listed in Table 4.1 are used.

Table 4.1: Summary of triggers used in the thesis

Usage	HLT Name	L(fb^{-1})
Analysis	HLT_Mu17_TrkIsoVVL_Mu8_TrkIsoVVL_v*	27.3
	HLT_Mu17_TrkIsoVVL_TkMu8_TrkIsoVVL_v*	27.3
	HLT_Mu17_TrkIsoVVL_Mu8_TrkIsoVVL_DZ_v*	8.6
	HLT_Mu17_TrkIsoVVL_TkMu8_TrkIsoVVL_DZ_v*	8.6
	HLT_Mu8_TrkIsoVVL_Ele23_CaloIdL_TrackIdL_IsoVL_v*	27.3
	HLT_Mu8_TrkIsoVVL_Ele23_CaloIdL_TrackIdL_IsoVL_DZ_v*	8.6
Fake Rate	HLT_Mu17_TrkIsoVVL_v*	Norm. to data[1]
	HLT_Mu8_TrkIsoVVL_v*	
	HLT_Ele23_CaloIdL_TrackIdL_IsoVL_PFJet30_v*	
ID, Trigger Efficiency	HLT_IsoMu24_v*	35.9
	HLT_Ele27_WPTight_Gsf_v*	35.9
	HLT_Ele27_eta2p1_WPTight_Gsf_v*	35.9
	HLT_Mu17_TrkIsoVVL_Mu8_TrkIsoVVL_v*	7.5
	HLT_Mu17_TrkIsoVVL_TkMu8_TrkIsoVVL_v*	7.5
	HLT_Mu8_TrkIsoVVL_Ele23_CaloIdL_TrackIdL_IsoVL_v*	7.5

4.1.2 Modeling of Simulated Processes

In the background estimation, processes with prompt leptons and electrons from conversions are estimated using simulated data sets. In this note, prompt leptons refer to electrons and muons from gauge or Higgs boson decays, including those from τ leptons from these bosons. The simulated background

[1]MC normalization for theses paths are obtained from control regions.

processes include W and Z boson processes, diboson processes, a vector boson or a SM Higgs boson produced with a top quark pair, $t\bar{t}$ production, single top quark production with W or Z bosons, triboson processes, and SM Higgs boson production from gluon fusion and vector boson fusion channels. In case of jet-induced nonprompt lepton background, it is not estimated with simulation, but with a data-driven method. This is mainly because of required sample size for the estimation. Because of a very small rate of jets producing nonprompt leptons passing identification, estimation of jet-induced nonprompt lepton production in $t\bar{t}$, QCD multijet, and V+jets processes require billions of MC events to be produced, and it is practically not feasible. In addition, theoretical modeling of fake lepton background is highly challenging, as it requires precise knowledge on interactions between jet constituents and detector materials, and formation of fake objects from those hits.

The set of MC samples used for SM backgrounds to the search are listed in Table 4.2. Samples for WZ and ZZ processes are simulated at the next-to-leading order (NLO) with the POWHEG V2 generator [122–125] for the mass of an opposite-sign-same-flavor lepton pair larger than 4 GeV at the matrix element level. The ratio of cross sections, k-factor, at the next-to-next-to-leading order (NNLO) to NLO, which is calculated in Ref. [126, 127], is applied for these processes. Events with W or Z bosons associated with $t\bar{t}$ processes are simulated with the MADGRAPH5_aMC@NLO v2.2.2 generator [128]. The MC sample for $t\bar{t}W$ processes is produced at LO with up to two additional partons with the MLM matching algorithm [129], and the sample for $t\bar{t}Z$ processes is produced at the LO with up to one additional parton with the MLM matching. $t\bar{t}H$ processes are produced at the NLO with the POWHEG V2 generator. The mass of top quarks is assumed to be 172.5 GeV in the simulation. Samples for conversion backgrounds ($Z\gamma$, $t\bar{t}\gamma$) are produced at the NLO with the

MadGraph5_aMC@NLO generator [128]. Both samples ($Z\gamma$, $t\bar{t}\gamma$) are produced at the NLO with up to one additional parton and merged with the FXFX algorithm [130]. In the $t\bar{t}\gamma$ sample, decays of top quarks and subsequent W bosons are treated with the Madspin program [131, 132]. Triboson processes are produced at the NLO with the MadGraph5_aMC@NLO generator. The SM Higgs boson production from gluon fusion and vector boson fusion channels are produced with the POWHEG V2, and its decay into four charged leptons, mediated by two Z bosons, is simulated with the JHUGEN generator [133].

Table 4.2: MC samples for estimation of backgrounds in the search

Process	$\sigma\mathcal{B}$*k-factor (pb)	N_{events}
WZ (WZ→3lν)	$4.42965 * 1.109$	1993200
ZZ (ZZ→4l)	$1.212 * 1.16$	6669988
ttW (inclusive)	0.6008	6880577
ttZ (inclusive)	0.8393	10882500
ttH (SM Higgs boson, exclude H→bb)	0.2151	3981250
tZ (Z→2l)	0.0758	2973639
Zγ (Z→2l)	117.864	14372682
ttγ (inclusive)	3.697	9728932
WWW (inclusive)	0.2086	240000
WWZ (inclusive)	0.1651	250000
WZZ (inclusive)	0.05565	246800
ZZZ (inclusive)	0.01398	249237
SM Higgs boson (vector boson fusion, H→4l)	0.00103	500000
SM Higgs boson (gluon fusion, H→4l)	0.01181	999800

The signal process, $pp \to t\bar{t} \to b\bar{b}H^+W$ with $H^+ \to WA \to W\mu^-\mu^+$, is simulated at the LO in the five-flavor scheme with the MadGraph5_aMC@NLO v2.4.2 generator. Charge-conjugated processes are implied throughout the chapter. Decays of top quarks, W, H^+, and A bosons are modeled with the same generator, and all possible decays of the two W bosons are considered except fully hadronic decay modes. Simulation of signal processes are performed for m_A values from 15 to 75 GeV with a mass step of 10 GeV, and for m_{H^+} values

Table 4.3: MC samples used for the control regions or studies on uncertainties

Process	$\sigma\mathcal{B}$(pb)$*$ k-factor	N_{events}
Background samples for prompt subtraction in fake rate measurement		
W boson (W$\to$lν)	61526.7	235575856
Z/γ boson (M-10to50, dilepton)	18610	40381392
Z/γ boson (M-50, dilepton)	5765.4	122055416
tt (inclusive)	831.76	76375312
single top (t-channel-top, inclusive)	136.02	67240808
single top (t-channel-antitop, inclusive)	80.9699	38811008
single top (s-channel, t$\to$blν)	3.36	1000000
single top (tW-antitop, exclude tW$\to$5q)	19.5545	5425134
single top (tW-top, exclude tW$\to$5q)	19.5545	5372991
WW (inclusive)	118.7	994012
WZ (inclusive)	47.13	1000000
ZZ (inclusive)	16.523	990064
Samples for MC study of fake objects		
tt (inclusive)	831.76	76375312
QCD (Pt-15to20, b/c$\to$e+X)	254596	2685602
QCD (Pt-20to30, b/c$\to$e+X)	328999.93	10987947
QCD (Pt-30to80, b/c$\to$e+X)	405623.4	15328096
QCD (Pt-80to170 , b/c$\to$e+X)	38104.43	14895274
QCD (Pt-170to250, b/c$\to$e+X)	2635.81332	9720760
QCD (Pt-250toInf, b/c$\to$e+X)	711.92588	9773617
QCD (Pt-20to30, EMEnriched)	557600000	9195339
QCD (Pt-30to50, EMEnriched)	136000000	6768384
QCD (Pt-50to80, EMEnriched)	19800000	23474166
QCD (Pt-80to120, EMEnriched)	2800000	41853500
QCD (Pt-120to170, EMEnriched)	477000	35817276
QCD (Pt-170to300, EMEnriched)	114000	11540163
QCD (Pt-300toInf, EMEnriched)	9000	7373633
QCD (Pt-15to20, MuEnrichedPt5)	1273190000	4141251
QCD (Pt-20to30, MuEnrichedPt5)	558528000	31475154
QCD (Pt-30to50, MuEnrichedPt5)	139803000	29824936
QCD (Pt-50to80, MuEnrichedPt5)	19222500	19806920
QCD (Pt-80to120, MuEnrichedPt5)	2758420	13669116
QCD (Pt-120to170, MuEnrichedPt5)	469797	11938140
QCD (Pt-170to300, MuEnrichedPt5)	117989	7947159
QCD (Pt-300to470, MuEnrichedPt5)	7820.25	16452588
QCD (Pt-470to600, MuEnrichedPt5)	645.528	5663755
QCD (Pt-600to800, MuEnrichedPt5)	187.109	5971175
QCD (Pt-800to1000, MuEnrichedPt5)	32.3486	5838541
QCD (Pt-1000toInf, MuEnrichedPt5)	10.4305	9609821

from $(m_{\mathrm{A}} + 85)$ to 160 GeV with a mass step of 10 GeV. The mass range of H^+ bosons is motivated from mass thresholds for the $\mathrm{H}^+ \to \mathrm{W}^+\mathrm{A}$ and $\mathrm{t} \to \mathrm{bH}^+$ decays. The upper boundary of the m_{A} range is determined from the crossing point of the two m_{H^+} thresholds, and the lower boundary is determined to avoid low-mass vector meson backgrounds. In addition, parameter regions with m_{A} values below 15 GeV receive strong constraints from existing search results, as explained in the Chapter 2. The top quark mass is set to be 172.5 GeV in accordance with the value used for SM MC samples.

Width values of H^+ and A bosons are chosen to be 1 MeV, which is similar to the A boson width at $\tan\beta = 1$ in the 2HDM. As can be seen in the Fig. 2.6, the A boson width in most of the 2HDM parameter regions for the m_{A} range is much smaller than the resolution of reconstructed dimuon invariant mass, which is approximately 1% of the m_{A} value, and it is experimentally indistinguishable. Hence, this Γ_{A} setting is sensible in the context of the 2HDM-like models, and the analysis focuses on the scenarios, in which the A boson width is smaller than the experimental resolution. On the other hand, the H^+ boson width is as small as a few hundred MeV for m_{H^+} values below the top mass threshold, as can be seen in the Fig. 2.5, and the signal extraction method used in the thesis is insensitive to the H^+ width value. Hence, the exact setting on the H^+ width does not have any noticeable impact on the final result.

In this chapter on the data analysis, the signal branching fraction, $\mathcal{B}_{\mathrm{sig}}$, and signal cross section, σ_{sig}, refer to the following expression,

$$\mathcal{B}_{\mathrm{sig}} = \mathcal{B}(\mathrm{t} \to \mathrm{bH}^+)\mathcal{B}(\mathrm{H}^+ \to \mathrm{W}^+\mathrm{A})\mathcal{B}(\mathrm{A} \to \mu^+\mu^-) \tag{4.1}$$
$$\sigma_{sig} = 2\sigma(\mathrm{pp} \to \mathrm{t\bar{t}})\mathcal{B}(\mathrm{t} \to \mathrm{bW}^+)\mathcal{B}(\mathrm{t} \to \mathrm{bH}^+)\mathcal{B}(\mathrm{H}^+ \to \mathrm{W}^+\mathrm{A})\mathcal{B}(\mathrm{A} \to \mu^+\mu^-).$$

The branching fraction of decay modes of the two W bosons in the signal decay

chain is assumed to be the observed value [134], which are respectively 0.1086, per lepton flavor, and 0.6742 for $W \to \ell\nu$ and $W \to$ hadrons decay modes.

All MC samples are produced with NNPDF3.0 parton distribution function (PDF) sets [135]. Parton shower and hadronization process are simulated with the PYTHIA 8 [136], and simulation of underlying events is tuned with the CUETP8M1 setting [137]. Then all the simulated events are subject to the GEANT4-based CMS detector simulation [138]. Pile-up interactions in events are also considered in simulation using the same program and tuning conditions. The additional pp collision events are separately simulated up to detector hits with varying number of pile-up events, and these are overlaid on the simulated detector hits from the hard physics process of interests. These combined simulated detector hits are used for simulation of responses from detector electronics to yield simulated raw data. The simulated raw data are processed with the same software programs as the real data. The pre-determined profile of number of pile-up events can be different from what was obtained in the experiment. Hence, the number distribution of true pile-up interactions in the simulated samples is reweighted to the profile at a fiducial inelastic pp cross section, also known as the min-bias cross section, that matches the observed distributions of variables sensitive to the pile-up multiplicity. Important variables among those include the multiplicity of reconstructed primary vertices and median p_T density from pile-up. As a result, the fiducial inelastic pp cross section is assumed to be 69.2 mb in the analysis.

4.2 Event Reconstruction

4.2.1 Vertex and Track

Reconstruction of interaction vertices and tracks is an important process in an offline analysis. A particle track provides information on its electric charge, spatial origin, and momentum with a high precision. Reconstructed vertices also provide information on the number of pile-up interactions in an event, instant luminosity, and minimizes the impact of pile-up interactions in an analysis. Reconstruction of tracks and vertices are mutually related and processed together, yet proceeds from a simpler method with the pixel detector to more complex algorithms with the entire tracking system [139].

The location of a beam spot, a 3-dimensional profile of interaction points in a bunch crossing, is needed for constraints in the reconstruction of primary vertices and tracks. During the reconstruction of primary vertices and tracks, it is estimated by two methods. The first method fits coordinates of reconstructed primary vertices to extract the information, and the second method analyzes the correlation of track coordinates from a shifted origin in global coordinates. The information is extracted from the events recorded in one lumisection (LS), 23 s, and those from up to 60 LS in a single run is combined as a weighted average. For a bunch crossing with 1000 tracks, the center of beam spots can be determined with a statistical precision of 5 μm.

A particle track is reconstructed using the Combinatorial Track Finder (CTF) software, an extension of Kalman filter method, for a p_{T} value larger than 80 MeV. The algorithm finds hits belonging to each track in several iterations, in which earlier iterations identify more straightforward cases of tracks with high-p_{T} values and consistent with the beam spot. Each iteration of the algorithm is seeded by two or three hits in the tracker, 3 pixel hits for the

initial iteration and mixed hits in strip tracker and pixel detectors in later iterations. Hits associated with reconstructed tracks in previous iterations are removed, and this facilitates more challenging reconstruction of low-p_{T} or displaced tracks. The group of hits are refit with removal of outlier hits. Then the quality of each track is assessed based on the number of hits, quality of fitting ($\chi 2/d.o.f.$), and compatibility with the beam spot and primary vertex that the track belongs to. Low quality tracks are considered to be random association of hits or highly affected by wrong hit assignments, hence discarded from the track collection. The analysis uses the high-purity selection, which reduces the fake track rate by a factor of two with a cost of 1–2% of tracking efficiency. For a track $p_{\mathrm{T}} > 1\,\mathrm{GeV}$, the tracking is nearly fully efficient for muons and 90% efficient for pions. The reduction of pion tracking efficiency is due to nuclear interactions with tracker materials, and because of the larger material budget, it is lower by 5–15% in endcaps. The fake rate of a pion track is approximately 1–3%, yet it can get as large as 15% for $p_{\mathrm{T}} > 100\,\mathrm{GeV}$, where they are often located inside the core of extremely dense jets of particles.

Using reconstructed tracks passing minimal quality criteria, primary interaction vertices in the beam spot are identified. The tracks are required to be consistent with the beam spot within 5 s.d. of its impact parameter uncertainty, reconstructed from 5 or more hit layers including 2 or more pixel hits, and have a good fit quality ($\chi^2/d.o.f. < 20$). The selected tracks are clustered based on their z-coordinates at their closest points to the beam spot using the deterministic annealing algorithm [139, 140], which determines the track association using the variable analogous to the statistical free energy and temperature. Then the clusters of tracks are fitted using the adaptive vertex fitter algorithm to determine vertex location and its covariance matrix. The precision of vertex location is strongly dependent on the number of tracks and their quality. For vertices

with more than 50 tracks, the resolution of transverse and longitudinal coordinates of the vertices are 20 and 25 μm for typical fiducial pile-up interaction vertices, and 10 and 12 μm for the the vertices with a jet with $E_{\mathrm{T}} > 20\,\mathrm{GeV}$.

4.2.2 Particle Flow Algorithm

As explained in the Chapter 3, each detector component targets different particle characteristics and can mutually complement their measurement. The particle flow algorithm [141] aims at achieving more accurate description of a global event activity by utilizing all the detector components together. The algorithm associates all detector activities in an event with the same origins and identifies as one of the final states in the detector, either muon, electron, photon, charged, or neutral hadrons. Using these final states, preceding processes in the event are reconstructed, for examples, decays of hadrons, quarks producing jets of collimated particles, and eventually heavier objects as top quarks, heavy vector or Higgs bosons.

The algorithm clusters adjacent hits in calorimeters and reconstruct tracks in inner tracking and muon systems. Detector activities from the same particle is linked, and detector hits belonging to identified particles are removed from collections to improve identification performance of more difficult objects in later stages. Because of small background in the muon system, the muon reconstruction is the simplest and performed first. Then electrons and isolated photons are reconstructed. As a large fraction of electrons and photons lose a significant portion of their energy in the tracker via bremsstrahlung and electromagnetic shower, they need to be considered simultaneously. Remaining detector hits are used to reconstruct hadrons and non-isolated photons. Then the post-processing steps are followed, which includes global assessment of inconsistencies or potential misreconstruction, and modifications are made if necessary.

Muons

Three kinds of tracks, standalone, global, and tracker muon tracks, are reconstructed for muons to combine inner tracking and muon systems. The standalone muon track is reconstructed using only the segments and hits in the muon system. The global muon track is reconstructed from fitting tracks in the two detector systems, if the two tracks are compatible at a common boundary surface. The global muon track requires more than one segments in different stations, hence the reconstruction often fails for muons with p_{T} below 10 GeV due to smaller number of hits or unusual pattern from multiple scattering in the steel yoke. Tracker muon recovers the reconstruction efficiency at low-p_{T}, as it requires only 1 compatible segment in the muon system within 4 s.d. of its position uncertainty.

To avoid misreconstructed case of punch-through hadrons, loose quality criteria are applied on the muon objects. If a sum of track p_{T} and E_{T} of calorimeter clusters within $\Delta R < 0.3$ from the global muon track is less than 10% of the muon p_{T}, no additional quality is required. For non-isolated global muons failing the previous criterion, the track has to satisfy the tight criteria of standard CMS muon identification, described in the later chapter. In addition, it has to include three muon segments in the track or the associated calorimeter energy should be compatible with a muon. Muons that failed the previous iterations for inferior track quality in either detection system is recovered if that in the other system is of high quality. The object is considered a muon if a standalone muon track is reconstructed from more than 22 DT or 14 CSC hits, or the inner track contains 13 measurements with compatible magnitude of calorimeter deposits. The efficiency of reconstruction and identification for the PF muon is better than 99% for the p_{T} value larger than 10 GeV.

Electrons and Isolated Photons

Electrons and photons have experimental signatures of high ECAL deposits in a narrow η window, but a relatively larger ϕ width for magnetic bendings, and small HCAL deposits behind it. Electrons and photons are distinguished by a presence of tracks consistent with the ECAL deposit. Both object reconstruction begins with the identification of a cluster of ECAL deposits, called a supercluster (SC).

Adjacent energy deposits in calorimeter crystals are clustered for those beyond thresholds, which are 80 and 300 MeV for energy in EB and EE, and 150 MeV for E_{T} in EE. If the largest deposit in a crystal exceeds 1 GeV, then this ECAL cluster is considered for supercluster reconstruction. ECAL clusters around the seed cluster within a window in the η-ϕ plane consistent with EM showering are merged to form a supercluster, where the size of the window varies with the seed E_{T} values.

Presence of an electron near the SC is searched, seeded by either reconstructed SCs or tracks. The ECAL-based seeding is initiated if the transverse energy, E_{T}^{SC}, and absolute energy ratio of HCAL and SC, H/E^{SC}, within $\Delta R < 0.15$ satisfy $E_{\mathrm{T}}^{SC} > 4\,\mathrm{GeV}$ and $H/E^{SC} < 0.15$. Assuming a helical path, if there are two barrel pixel hits or endcap inner tracker hits consistent with the SC, then the GSF track algorithm is initiated. On the other hand, tracker-based seeding is initiated if a general track consistent with an ECAL cluster is found using a boosted decision tree classifier. The ECAL-based approach outperforms the tracker-based method for $E_{\mathrm{T}} > 10\,\mathrm{GeV}$, and the latter is important for low-p_{T} or non-isolated electrons.

A special track reconstruction of the GSF algorithm is deployed for the electrons, as the electrons typically lose a large portion of its energy through

bremsstrahlung in the tracker and its track pattern can be different from those of heavy particles. For an electron track, the track parameters are evaluated at each layer and the track is iteratively formed in consideration of an energy loss model of a Bethe-Heitler distribution [142]. Up to five tracks at each layer are considered if multiple compatible hits are found, and final track candidates sharing same hits are dropped, based on the number of hits and track fit quality, χ^2. The reconstructed GSF track is associated with the supercluster if it satisfies a BDT criterion or following matching criteria, only for ECAL-seeded tracks,

- $|\Delta\eta_{in}| \equiv |\eta_{SC} - \eta^{extra}_{trk-in}| < 0.02$
- $|\Delta\phi_{in}| \equiv |\phi_{SC} - \phi^{extra}_{trk-in}| < 0.15$,

where η_{SC} and ϕ_{SC} are coordinates of the SC, and η^{extra}_{trk-in} and ϕ^{extra}_{trk-in} are coordinates of the point formed by a extrapolation of a GSF track from the innermost layer to the calorimeter.

Refinement processes are then followed to recover missing clusters from bremsstrahlung and photon conversions. At each layer of the GSF track, ECAL clusters are searched at the extrapolation of the tangent to the track. Those clusters are considered to be bremsstrahlung from the electron, hence merged to the SC. Photon conversions are identified using a BDT classifier using variables including missing hits, the location of the first track hit, and the transverse impact parameter. If the two displaced tracks with calorimeter clusters are classified as conversion electrons and compatible with the bremsstrahlung of primary electrons, the ECAL clusters are merged to the SC.

At last, the SC with and without an associated GSF track is considered an electron and a photon, respectively. In addition, a set of loose identification criteria is also applied on these object to reduce mis-identification rate. Electrons are distinguished using a BDT classifier with 14 variables related to

shower shapes and track parameters, and photons are required to pass a loose isolation and shower shape criteria. The reconstruction efficiency is nearly 100% for photons and better than 95% for electrons.

Hadrons and Non-isolated Photons

Among the remaining detector activity, calorimeter clusters without associated tracks are considered neutral hadrons or photons. As the majority of the jet constituents are pions and neutral pions decay to two photons before reaching the detector, the neutral component of jet energy detected in the detector is typically from photons. In a study based on the simulation, approximately 65, 25, and 10% of the jet energy is observed to be from charged hadrons, photons, and neutral hadrons, respectively, and neutral hadron leaves only 3% of jet energy in the ECAL. Hence, as an approximation, ECAL clusters are identified as non-isolated photons, and HCAL clusters are considered to be neutral hadrons, respectively.

Calorimetric clusters associated with tracks are decomposed to charged, neutral hadrons, and photons. Each track is considered to be a pion track, classified as a charged hadron, and corresponding expected energy in the calorimeter from tracks is compared with the observed clusters. If the calorimetric energy exceeds the expectation beyond the uncertainty, the excess in the HCAL cluster energy larger than 1 GeV is considered to be a neutral hadron, and those in the ECAL cluster energy larger than 500 MeV is assigned to a non-isolated photon. In contrast, if the calorimetric energy is smaller than the track momenta summation by three or more s.d., then additional non-isolated muons are searched with relaxed criteria. In case the difference persists, the remaining component is attributed to misreconstructed tracks, and tracks are removed from the clusters with the decreasing order of p_{T} uncertainty until the energy gap disappears.

4.2.3 Jet

Elementary particles participating in the strong interaction can never be observed as free particles, as the interaction strength increases with a length scale. With an exception of top quarks, which decays to a W boson and a b quark via the weak interaction, high energy quarks and gluons result in a large number of collimated color-neutral particles, typically low-p_{T} hadrons, around the original parton momenta. This stream of particles are referred to as a jet. Using this object as a proxy for the original parton, physics processes involving those elementary particles can be studied.

There are various ways of grouping particles in such geometric patterns to jets. In this analysis, the anti-kt algorithm [143] is used for the jet reconstruction. In this algorithm, a jet clustering is processed with two distance parameters, a distance d_{ij} between two entities of either a particle or a jet, and a distance d_{iB} between an entity and the beam. The two distance parameters are defined as,

$$\begin{aligned} d_{iB} &= k_{t,i}^{-2} \\ d_{ij} &= min(k_{t,i}^{-2}, k_{t,j}^{-2}) \frac{(y_i - y_j)^2 + (\phi_1 - \phi_2)^2}{R^2}, \end{aligned} \tag{4.2}$$

where k_t and y are the transverse momentum and rapidity, $\mathrm{arctanh}(v_i/c)$, of an object. Particles with the smallest distance are clustered until the value exceeds the distance from the beam. In such a case, the jet is removed from a collection, and the clustering is repeated until the input collection becomes empty. The algorithm associates a soft particle to a hard particle and any particle to one at a very close distance, and leads to conical jets with an approximate size of R in a y-ϕ plane, identical to a η-ϕ plane in the relativistic limit.

In the analysis, the objects reconstructed with the PF algorithm are used as input for the jet reconstruction, and a radius parameter R is chosen to be 0.4. As the hadrons produced in the jet evolution can decay to leptons, they are also included in the jet reconstruction. Charged particles associated with different primary vertices are excluded from the input collection to minimize impact of pile-up interactions. For the neutral particles from the pile-up interactions, an offset correction is applied using the product of the median expected p_{T} density, ρ, and effective jet area. The ρ variable in each event is determined as a median value of p_{T}/A_j of jets reconstructed using kt algorithm, identical to the anti-kt algorithm except k_t^2 in places of k_t^{-2}, with the R parameter at 0.6. The variable A_j refers to the jet area. The p_{T} and η dependence of the pile-up contribution is absorbed into the effective area, measured using simulated samples and corrected using zero-bias data sets. After corrections for the pile-up contribution, reconstructed jets with $p_{\mathrm{T}} > 10\,\mathrm{GeV}$ are kept for the analysis.

4.2.4 Missing Transverse Momentum

Stable or long-lived particles, of which a decay length is larger than the size of the CMS detector, not participating in the strong or electromagnetic interaction does not leave a signal in the detector system. Production of such particles leads to an imbalance of momenta of observed particles in an event. If their momenta are measured with an enough precision, then the magnitude of this imbalance can be used to deduce total momenta of undetected particles, most notably neutrinos. By the nature of collisions of composite particles, the fractions of two proton momenta carried by hard-scattering partons are unknown, hence the longitudinal imbalance cannot be related to the undetected momenta and only the transverse component is used for this purpose. The missing transverse momentum $\vec{p}_{\mathrm{T}}^{\,\mathrm{miss}}$ is defined as a negative vectorial sum of

particle momenta. The variable is calculated using all particles identified by the PF algorithm, including those from different primary vertices. In the thesis, the magnitude of $\vec{p}_{\mathrm{T}}^{\,\mathrm{miss}}$ and its energy component are denoted by $p_{\mathrm{T}}^{\mathrm{miss}}$ and $E_{\mathrm{T}}^{\mathrm{miss}}$.

4.3 Object Selection

The analysis aims to look for an extremely rare process, of which the rate is smaller than the total pp scattering rate by a factor less than 10^{-12}, leading to an increased importance of backgrounds with mis-identified objects. Reconstructed objects described in the previous sections are further discriminated using variables related to their characteristic patterns in the detection systems. In this chapter, the selection criteria for the signal objects are explained.

4.3.1 Primary Vertex

During the pp collision experiment in 2016, each bunch crossing yields approximately 10–40 pile-up interactions with a mean value of 23, requiring a selection of an interaction vertex to analyze. In the thesis, the high quality vertex with the largest activity is selected. The candidate vertex is required to be within 2 and 24 cm in the transverse and longitudinal directions from the nominal center of the detector, and formed by at least four tracks.

For the reconstructed vertices satisfying these criteria, the vertex with the largest value of $\sum_i p_{\mathrm{T},i}^2$ is chosen, where the $p_{\mathrm{T},i}$ is the p_{T} value of an i-th physics object originating from the vertex. The physics objects used for the vertex selection are jets, reconstructed with tracks from the vertex using the anti-kt algorithm and a radius parameter of 0.4, and the missing transverse momentum calculated as a negative vectorial sum of these track-based jets.

4.3.2 Muon

The muons of the signal process are produced from either W or A boson decays. The signal muons from A boson decays have typical p_{T} values between 10 and 40 GeV with a tail of the distribution stretching up to 120 GeV, and those from W boson decays are spread between a few and 200 GeV, with a mean value

near 30 GeV. In both cases, the muons are produced towards the central part of the detector system. In the analysis, muons with $p_{\mathrm{T}} > 10\,\mathrm{GeV}$, reconstructed in the entire muon system ($|\eta| < 2.4$), are considered. The muons are further classified by a set of experimental variables in order to reduce contamination from misreconstructed or nonprompt muons.

Baseline requirements are the tight criteria of the standard CMS muon identification [114]. This requires high quality of a track with enough number of hits in all of the pixel detector, the tracker, and the muon spectrometer with a good global track fit. Exact requirements can be summarized as follows,

- reconstructed as a global muon and also qualify as a PF muon,
- $\chi^2/n_{dof} < 10$ for the global muon track fit,
- include a valid hit in the muon system,
- include a valid pixel hit,
- include hits from more than 5 strip tracker layers,
- include segments in at least 2 muon stations,
- $|d_0| < 2\,\mathrm{mm}$ and $|d_z| < 5\,\mathrm{mm}$,

where the $|d_0|$ and $|d_z|$ are the transverse and longitudinal distance between the primary vertex and the closest approach of a track to it, and they are referred to as the transverse and longitudinal impact parameters. These criteria aims at discrimination of mis-identified objects produced from punch-through hadrons or nonprompt muons produced inside the detector.

Additional cuts are applied on top of these baseline selections to further suppress background rate. The χ^2/n_{dof} of the global track fit is tightened to

ensure that they are real muons. To distinguish prompt muons from secondary muons originating from hadron decays in jets, the muons are required to be isolated from hadronic activity and produced in the vicinity of the primary vertex using I^{μ}_{rel} and impact parameter variables. The relative isolation I^{μ}_{rel} is defined as,

$$I^{\mu}_{rel} = \frac{I_{ch,PV} + \max(0, I_{nh} + I_{ph} - 0.5 I_{ch,PU})}{p_{\mathrm{T}}(\mu)}, \tag{4.3}$$

where $I_{ch,PV}$, I_{nh}, I_{ph}, and $I_{ch,PU}$ are scalar p_{T} sums of charged hadrons from the primary vertex, neutral hadrons, photons, and charged hadrons from pile-up vertices within $\Delta R < 0.4$ from the muon. The $I_{ch,PU}$ term in the expression is an approximation of expected neutral pile-up contributions to I_{nh} and I_{ph}, motivated by a mean contribution of charged hadrons to the jet energy, $\approx 65\%$. The relative isolation is required to be less than 0.2, and this reduces jet-induced background rate by 80% while retaining 90% of signal efficiency when compared to a loose working point, $I^{\mu}_{rel} < 0.6$. The impact parameter of signal muons should satisfy $|d_0| < 0.1\,\mathrm{mm}$, $|d_z| < 0.5\,\mathrm{mm}$, and $|d_0/\sigma_{d_0}| < 4$, where σ_{d_0} is the resolution of d_0. In simulation, these tight impact parameter conditions reduce approximately 60% of non-prompt muon rate with only 2% of a signal loss, when compared to the tight criteria of the standard CMS identification. The full list of ID criteria is listed in Table 4.4, the tight working point (WP) is used for signal identification, and the loose WP is used for background estimation from a sideband region or checking the presence of additional low-quality prompt leptons in the events.

Performance in Data

Efficiency of muon reconstruction and identification is measured with the

Table 4.4: Muon ID criteria

ID Variable	Cut Value	
	Tight WP	Loose WP
standard CMS tight identification	✓	✓
I^{μ}_{rel}	< 0.2	<0.6
global track χ^2/dof	< 4	-
$\lvert d_0 \rvert$(mm)	<0.1	<2
$\lvert d_z \rvert$(mm)	<0.5	<1
$\lvert d_0/\sigma_{d_0} \rvert$	< 4	< 4

tag and probe method using dimuon events from the Drell-Yan production. Oppositely charged inner-track pairs with the invariant mass between 70 and 130 GeV are selected for the efficiency measurement. Each track pair is divided to a tag and a probe, where the tag is required to satisfy a tight selection to ensure a real physics objects and fire triggers to be included in data sets, and the probe is used to measure the efficiency for a procedure of interest. Tag tracks are required to be muons passing the tight identification of the analysis, firing a single muon trigger (HLT_IsoMu24_v*), and having p_{T} >27 GeV. Probe tracks are general tracks with p_{T} >10 GeV and $|\eta|$ <2.4. Passing probes are required to be muons passing tight ID criteria of the analysis. Number of probes are extracted from fitting the Z boson resonance, and only the events with a single probe multiplicity are used. The signal template, with 40 bins, is modelled with the Double Voigtian function. Combined efficiency of the muon reconstruction and identification, measured with data, is shown in Figure 4.1. The typical efficiency of data is approximately 90% with 3% of difference between data and simulation.

For the systematic uncertainty in the measurement, different conditions are examined for the criteria of tag muons, number of mass bins, signal shape, and

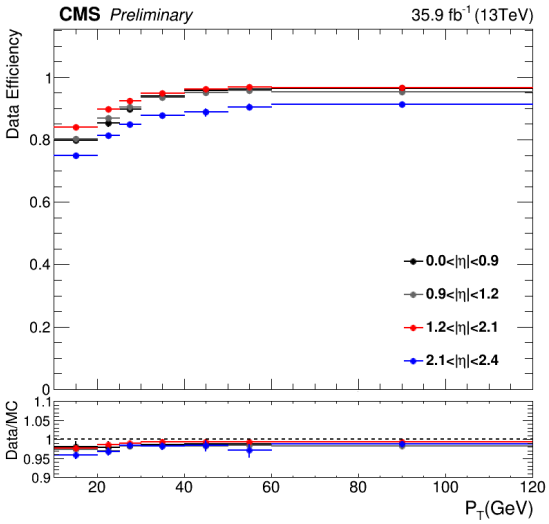

Figure 4.1: Combined efficiency of muon reconstruction and identification

mass range in the fitting. For the tag criteria, two different isolation working points of 0.15 and 0.25 have been checked instead of the nominal value, 0.20. For signal shape, a single Voigtian function is checked instead of the nominal double Voigtian distribution. For the number of mass bins, templates with 30 and 50 bins are used instead of the nominal 40 bins. For the dimuon mass range, two alternative ranges, [60,130] and [70,120] (GeV), are tested instead of the nominal range, [70,130] (GeV). The systematic uncertainty is observed to be less than 2% in all p_{T} and $|\eta|$ range of muons.

4.3.3 Electron

Signal electrons are always produced from W boson decays. Kinematic patterns are similar to the descriptions for the muons from W boson decays in the previous section. They typically exhibit p_{T} values of a few tens of GeV and are emitted towards the barrel detector systems. Electrons with $p_{\mathrm{T}} > 25\,\mathrm{GeV}$ and in the inner tracker coverage, $|\eta| < 2.5$, are considered for the signal identi-

fication. The p_{T} threshold is motivated by the trigger p_{T} thresholds for electrons. For the identification of additional low-quality electrons in events, they are identified down to 10 GeV. As the gap region between the EE and EB are highly prone to mis-identification, the electrons with its SC location in the range $1.442 < |\eta| < 1.566$ are not used for any purposes.

Electrons are further classified by a hybrid method of cut-based and multivariate (MVA) identification in order to reduce contamination from fake electrons. The MVA classifier used in this analysis is the boosted decision tree (BDT) discriminant of the standard CMS electron identifications [144]. The classifier was trained to discriminate prompt electrons from misreconstructed and nonprompt electrons in the electroweak scale. The training was separately done for three eta regions of inner barrel ($|\eta| < 0.8$), outer barrel ($0.8 < |\eta| < 1.47$), and endcap ($|\eta| > 1.47$), using numerous variables for track and calorimetric patterns. At the WP for the signal identification, the classifier rejects 99% of jet-induced nonprompt or misreconstructed electrons with 10% loss of prompt electrons from Z decays.

On top of MVA requirements, we ensure the electron is well isolated in the detector and originating from the primary vertex using the relative isolation of electrons, I^{e}_{rel}, and impact parameter variables. The I^{e}_{rel} variable is defined as,

$$I^{\mathrm{e}}_{rel} = \frac{I_{ch,PV} + \max(0, I_{nh} + I_{ph} - \rho A_{eff})}{p_{\mathrm{T}}(\mathrm{e})}, \tag{4.4}$$

where the variables $I_{ch,PV}$, I_{nh}, and I_{ph} are identical to those for muons except the smaller radius of a cone, 0.3, and A_{eff} is the effective area of the cone, parameterized as a function of $|\eta|$. The relative isolation of signal electrons is required to be less than 0.06, which reduces the nonprompt electron rate by 85% and retains 90% of prompt electron efficiency in $\mathrm{t\bar{t}}$ simulation. The impact parameters of signal electrons should satisfy the conditions, $|d_0|<0.25$ mm,

$|d_z|$<1 mm, and $|d_0/\sigma_{d_0}|$<4, of which additional cut efficiency is approximately 98% for prompt electrons and 75% for nonprompt electrons in $t\bar{t}$ simulation.

In addition, criteria for rejecting photon conversions and those emulating trigger selections are also applied. The conversion veto selection requires that the electron is not compatible with a conversion hypothesis. If an electron with the opposite charge in the detector is found to form a vertex with the signal candidate electron, then the electron-pair is examined. To be considered as originating from a photon conversion, the radial distance between the vertex and the center of the beam spot is larger than 2 cm, and the electrons should not have track hits before this vertex. Most importantly, the p-value of the $\chi^2/n_{d.o.f.}$ of the vertex fit should be less than 10^{-6}, implying a mis-classification rate of a conversion vertex less than 10^{-6}. On the other hand, the trigger emulation cuts are intended for reducing bias in estimation of nonprompt lepton backgrounds arising from online electron selections. The variables include following lists,

- $\sigma_{i\eta i\eta}$: defined as, $[\sum_i(\eta_i - \bar{\eta})^2 w_i]/\sum_i w_i$, where the sum runs over 5×5 crystals around the highest E_{T} crystal in the SC, and w_i is defined as, $w_i = \max(0, 4.7 + \ln(E_i/E_{5\times5}))$.

- $|\Delta\eta_{in}|$: the difference in η coordinates of the seed ECAL cluster for the SC and the point at the calorimeter from extrapolation of the GSF track from the innermost layer.

- $|\Delta\phi_{in}|$: the difference in ϕ coordinates of the energy-weighted SC position and the point at the calorimeter from extrapolation of the GSF track from the innermost layer.

- H/E : the ratio of HCAL deposits within $\Delta R < 0.15$ from the SC position and the supercluster E_{T}.

- ECAL PF Cluster Iso : the E_{T} sum of ECAL deposits within $\Delta R < 0.3$ from the SC.
- HCAL PF Cluster Iso : the E_{T} sum of HCAL deposits within $\Delta R < 0.3$ from the SC.
- Tracker Iso : the p_{T} sum of other tracks within $\Delta R < 0.3$ from the SC.

A full list of identification criteria is shown in Table 4.5. The tight WP is used for the identification of signal electrons, the loose WP is used for estimation of nonprompt lepton background from the sideband and identification of additional low quality leptons in events.

Table 4.5: Electron identification criteria. In case η dependent cut is applied, it is denoted by tuples. A tuple (a,b) represents that the value a and b are applied to $|\eta|<1.479$ and $1.479<|\eta|<2.5$, and (a,b,c) represents that a, b, and c are applied to $|\eta|<0.8$, $0.8<|\eta|<1.479$, and $1.479<|\eta|<2.5$, respectively.

Variable	Cut Value	
	Tight WP	Loose WP
MVA	>(0.837,0.715,0.357)	>(-0.92,-0.88,-0.78)
I^{e}_{rel}	< 0.06	< 0.4
$\lvert d_0\rvert$(mm)	<0.25	<0.25
$\lvert d_z\rvert$(mm)	< 1	< 1
$\lvert d_0/\sigma_{d_0}\rvert$	< 4	< 4
Conversion Veto	✓	✓
Trigger Emulation Cuts		
$\sigma_{i\eta i\eta}$	<(0.012,0.033)	<(0.012,0.033)
$\lvert\Delta\eta_{in}\rvert$	<(0.0095, –)	<(0.0095, –)
$\lvert\Delta\phi_{in}\rvert$	<(0.065, –)	<(0.065, –)
H/E	<(0.09,0.09)	<(0.09,0.09)
Rel. ECAL PF Cluster Iso	<(0.37,0.45)	<(0.37,0.45)
Rel. HCAL PF Cluster Iso	<(0.25,0.28)	<(0.25,0.28)
Rel. Tracker Iso	<0.18	<0.18

Performance in Data

Efficiency of electron identification is measured with the tag and probe method using dielectron Drell-Yan events. Oppositely charged dielectron events within the invariant mass range, 60<M(ee)<120 GeV, passing a single electron trigger (HLT_Ele27_eta2p1_WPTight_Gsf_v*) are used. Tag electrons are required to fire the trigger, have p_{T} >30 GeV, $|\eta_{SC}|$ <2.1, and be outside the gap region of ECAL. The number of passing and failing probes are extracted from fitting the Z boson resonance. The signal template is modeled using a distribution obtained from simulation of Z boson decays, convoluted with a Gaussian resolution function. On the other hand, the background template is modeled as a RooCMSShape function, defined as a product of an exponential and an error functions. Efficiency in a simulated sample is extracted from counting number of probes that are matched to generator-level electrons from Z boson decays. Systematic uncertainty in the efficiency measurement is estimated with variations of conditions. For an alternative signal shape, the template is modeled with a Breit-Wigner function smeared with an one-sided Crystal Ball function, and for an alternative background shape, it is modeled with an exponential function. A tighter tag condition is examined by requiring an additional cut of MVA>0.92, and a different generator of MC@NLO is tested.

The identification efficiency measured from data is observed to be approximately 80% with 5% of the difference between the simulation and data, as shown in the Fig. 4.2. The difference of efficiency between data and simulation is corrected with measured efficiency scale factor in the analysis. Uncertainty in efficiency is typically 1∼2%.

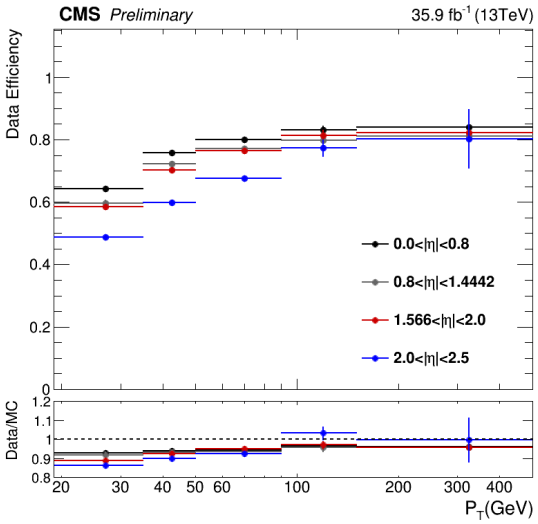

Figure 4.2: Efficiency of electron identification

4.3.4 Jet

Jets in the signal events are typically emitted towards the barrel region, yet with a large range of p_{T} values depending on their origins. The jets from the W boson decays have similar p_{T} range as the electrons, a few tens of GeV with a mean value near 30–40 GeV, and p_{T} values of those from the SM top quark decay, $\mathrm{t} \to \mathrm{bW}$, are typically around 80 GeV and spread up to a few hundred GeV. In contrast, the p_{T} value of the b-jet produced in association with the H^+ boson, $\mathrm{t} \to \mathrm{bH}^+$, highly depends on the Higgs boson mass, and it can be vanishingly small for $m_{\mathrm{H}^+} \approx m_{\mathrm{t}}$. In this analysis, the reconstructed jet objects are considered for $p_{\mathrm{T}} > 25\,\mathrm{GeV}$ and $|\eta| < 2.4$.

Constituents of reconstructed jets are not always genuine particles with well-measured properties, but can be merely a noise in the detector or a poorly reconstructed particle. Jets with their energy values dominated by a single detector component or a particle type typically correspond to such cases. In

order to reject such jets strongly impacted by malfunctioning detectors or mis-reconstructed objects, a set of loose criteria is required, which is summarized in the Table 4.6. This selection rejects a majority of fake jets, yet keeps genuine particle jets with an efficiency value close to 100%.

Table 4.6: Jet identification criteria

Variable	Cut
number of jet constituents	> 1
charged particle multiplicity among jet constituents	> 0
charged hadron fraction of jet energy	> 0
neutral hadron fraction of jet energy	< 0.99
electron fraction of jet energy	< 0.99
photon fraction of jet energy	< 0.99

Signal leptons can also be included in the jet collection, as the leptons are used as the input for the jet reconstruction. This occurs very frequently, because of the loose identification criteria and large pile-up activity. As the jets are mainly intended for the study of hadronic process of the signal, the double counting of leptons in the jet collection needs to be avoided. Hence, the jets found within $\Delta R < 0.4$ from a reconstructed lepton passing the loose WP identification are discarded from the jet collection.

Identification of b jets

Jets originating from b quarks can be identified by analyzing their constituents. B hadrons decay mainly via the cross-generation weak interaction, strongly suppressed by the off-diagonal CKM matrix element, hence its decay length is as large as a few mm, long enough to be well distinguished from the primary vertex using the tracking system. In addition, the large mass of B

meson result in its daughter particle p_{T} higher than those from other hadrons. Hence, the jets including B hadrons have distinctive features of displaced higher p_{T} tracks forming a secondary vertex separated from the primary vertex.

The Combined Secondary Vertex v2 (CSVv2) algorithm [145] is one of the methods for this purpose. The CSVv2 algorithm is based on the multivariate analysis method of an artificial neural network, specifically feed-forward multilayer perceptrons with a single hidden layer. It analyzes 19 variables motivated from kinematic properties of B hadrons in jets, and returns a value between 0 and 1, increasing with the likelihood of originating from b jets. In case the B hadrons decay close to the primary vertex, or less than two tracks from its decay is reconstructed, b jets may not include a secondary vertex. Hence, the training is separately done for three cases of jets with a secondary vertex, jets without a secondary vertex but with at least two displaced tracks not originating from K_S decays, and the remaining jets. The resulting three discriminator values are combined using the likelihood ratio in consideration of different jet flavors. These process is separately done for b jet discrimination against c jets and light (udsg) jets, and a linear combination of these two discriminator forms the final classifier of the CSVv2 algorithm.

In this analysis, the medium working point of the CMS b-tagging with the CSVv2 algorithm [145] is used. In the simulation study using this working point, b jets are identified with an efficiency of 63%, and c and light jets are misclassified with a rate of 12 and 0.9%, respectively. Performance of the algorithm in real data is measured using an inclusive jet sample and a muon-enriched jet sample, and the simulated samples of the analysis is corrected using the factors for the difference between the tagging efficiency in real data and simulation derived from these data samples.

4.3.5 Missing Transverse Momentum

The reconstructed $\vec{p}_{\mathrm{T}}^{\,\mathrm{miss}}$ relies on an accurate global reconstruction of particles within the detector acceptance, yet, rarely, noises in the detector can result in a large $\vec{p}_{\mathrm{T}}^{\,\mathrm{miss}}$. Therefore, a series of algorithms are developed for analyzing various anomalous detector signals, and the detector hits identified as a noise are masked in the reconstruction for small number of channels. If a large number of channels in an event are affected by noise, then the event is considered unacceptable for physics analysis and rejected. Fraction of such events is negligibly small. The event filters for known detector issues can be summarized as follows [146].

- HCAL filters: a large HCAL unphysical signal can be produced by direct particle interactions with light guides and photomultipliers in HF or a random noise in the photodiodes and electronics in the read-out box of HB and HE, which can affect up-to 72 channels at a time. These are identified by analyzing timing, pulse shape, and geometric patterns of photodiodes and read-out box channels.

- ECAL filters: similarly to HCAL, a large ECAL unphysical signal can be produced by direct particle interactions in photodetectors or electronics noise. These are identified from timing and geometric patterns. Also some channels in ECAL crystals produce extreme spurious spikes. Such events are identified from total SC energy and number of low-quality hits.

- beam halo filter: non-beam particles traveling in the LHC can collide with the detector and contaminate the data. It can be identified by activity in the calorimeters and CSC muon detector along a line with a constant azimuthal coordinate.

- reconstruction filter: a misreconstructed high-p_{T} track can lead to an anomalous large $p_{\mathrm{T}}^{\mathrm{miss}}$ signal. They are identified based on the uncertainty of the track fit.

In addition, by definition of the $\vec{p}_{\mathrm{T}}^{\mathrm{miss}}$, errors in the momentum measurements of all particles in events is propagated to this object. Especially, the errors in the jet energy typically have the largest impact on the $\vec{p}_{\mathrm{T}}^{\mathrm{miss}}$. Hence, the corrections applied on the jet energy, including those for both scale and resolutions, are propagated to the $\vec{p}_{\mathrm{T}}^{\mathrm{miss}}$ calculation.

The calculation of $\vec{p}_{\mathrm{T}}^{\mathrm{miss}}$ can be biased by nonhomogeneous detector response, nonfunctioning detector components, mis-alignment, and displacement of a beam spot. As a result, raw $\vec{p}_{\mathrm{T}}^{\mathrm{miss}}$ azimuthal distribution is not uniform, but exhibits a sinusoidal distribution, of which magnitude linearly increase with the number of pile-up interactions in Drell-Yan events. This effect is corrected by shifting the origin of coordinates in the transverse plane. The correction is derived using $\mathrm{Z} \to \mu^{+}\mu^{-}$ events, and parameterized as a function of number of reconstructed primary vertices. This also partly corrects for the impact of pile-up deposits lost through the imperfect detector response.

4.4 Trigger Selection

4.4.1 Selection Strategy

A set of dilepton triggers are used for this analysis, as listed in Table 4.1, which are closely related to kinematic characteristics of signal events. The majority of trilepton signal events are from WW $\rightarrow \ell\nu$qq$'$ and A $\rightarrow \mu\mu$ processes. Those leptons are composed of one hard lepton of $p_{\mathrm{T}} \sim 40$ GeV from W boson decay, and two comparatively soft muons from A $\rightarrow \mu\mu$ decay, where the leading muon from A has p_{T} of 10–40 GeV, as shown in Fig. 4.3. Thus we chose triggers with p_{T} thresholds of the leading lepton at 17–23 GeV that targets the lepton from W boson decays, a p_{T} threshold of subleading muon at 8 GeV that targets the leading lepton from A boson decays.

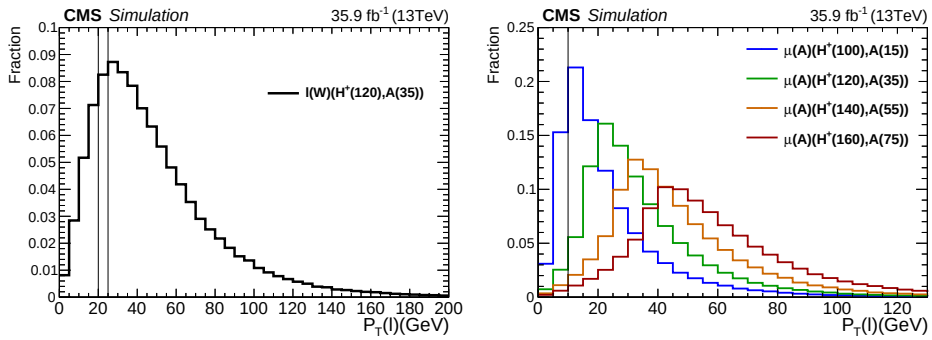

Figure 4.3: The p_{T} distribution of generator-level leptons from W boson decays (left), and leading muons from A boson decays (right) within the detector acceptance ($|\eta(\mathrm{e})|$ <2.5, $|\eta(\mu)|$ <2.4). The analysis-level p_{T} cuts induced by triggers (p_{T} thresholds+2–3GeV) are lined in the figures.

In the e$\mu\mu$ channel, the possibility of covering phase space of low-p_{T} electrons and high-p_{T} muons by using an additional eμ trigger with lower electron p_{T} and higher muon p_{T} thresholds is not considered, since the sensitivity of the search is not expected to be improved. This is mainly due to difference in

the fraction of low-p_{T} electrons between electrons from W boson decays and nonprompt electrons from jets. The fraction is small for electrons from W boson decays in contrast with nonprompt electrons, so the increase in nonprompt electron background is expected to be much larger than signal processes when the electron-p_{T} cut is lowered. In addition, the increase in the signal rate is further suppressed by the higher muon p_{T} threshold on low-p_{T} muons from A boson decays in many of the signal hypotheses.

An alternative approach with additional single lepton triggers is not considered as well. As will be discussed in the next subsections, the trigger selection was observed to be nearly fully efficient, 100% (3μ) and 97% (1e2μ), in the simulation, hence a gain in trigger efficiency was expected to be negligible for 3μ events and less than 3% for 1e2μ events. Besides, the online selection of single lepton triggers are much tighter than the offline identification. This can potentially bias the estimation of nonprompt lepton backgrounds from sidebands in identification variables in this analysis. In a study based on simulated samples, extrapolation factors from sidebands passing single lepton triggers are observed to be biased by 300% from those of inclusive samples. For these reasons, the usage of additional low-p_{T} single lepton triggers is avoided in the analysis.

The expected fraction of signal processes that can be triggered is approximately 60–90% depending on mass hypotheses and final states. The fraction of signals with at least two generator-level leptons within the geometric detector acceptance is in general $\approx$ 90%, hence the variation of the fraction is mainly determined by p_{T} requirements of triggers.

4.4.2 Efficiency Measurement

In simulated samples, trigger efficiency is observed to be 97 and 100% for 1e2μ and 3μ events, respectively. The high trigger efficiency is achieved from

multiple sets of trigger objects in each event fulfilling the trigger requirements. There can be up to 2 or 3 signal lepton pairs satisfying the trigger requirements for 1e2μ or 3μ events, and these additional pairs recover efficiency whenever the first pair failed the selection.

Trigger efficiency in data is measured in terms of factorized filter efficiencies. A dilepton trigger can be factorized into filters constituting the trigger. A collection of entire filters applied on a single physics object are commonly referred to as a "leg". There are also another type of filters, which are applied on two physics objects. These will be denoted by "pairwise filter" in the thesis. The dilepton trigger sequences are then factorized to two legs, applied on each of two leptons, and pairwise filters. These leg and pairwise filter efficiency is measured using the tag-and-probe method or reference triggers. This approach of factorized filters provides the trigger efficiency in fine p_{T} and η bins with uncertainty less than O(1%).

For dimuon triggers, the leg efficiency is measured with the tag and probe method using dimuon events within the invariant mass range, [70, 130] (GeV), passing the single muon trigger. Tag muons are required to pass the standard CMS tight identification, an isolation condition $I^{\mu}_{rel} < 0.2$, and fire the single muon trigger. Probe muons are required to pass tight identification of the analysis. The signal template is modeled with a double Voigtian function, and the background template is modeled with an exponential function.

The pairwise filter efficiency of dimuon triggers is measured using events collected with reference triggers, of which the sequence and filters are identical to the signal dilepton triggers except the absence of pairwise filters. Events with opposite-sign muon pairs with $|\mathrm{M}(\mu\mu) - 91.2| < 20\,\mathrm{GeV}$, $p_{\mathrm{T}}(\mu) > 20(10)\,\mathrm{GeV}$ for the leading (subleading) muon, $\Delta R(\mu\mu) > 0.4$, and pass the last filters of the reference triggers are used. Passing events are required to have both muons

passing the pairwise filters.

For systematic uncertainty of leg efficiency, variations in the number of bins, the mass range of fitting, the signal shape, and tag muon requirements are considered. For variations of number of mass bins, 30 and 50 bins are checked instead of 40 bins for central value. For alternative mass ranges, [60,130] and [70,120] (GeV) are used. For ian alternative signal shape, a single Voigtian function is considered. The impact of the probe multiplicity is also checked by removing a single probe requirement in the event. For alternative tag conditions, two conditions of $p_{\mathrm{T}}(\mu_{tag})$>30 GeV with I^{μ}_{rel}<0.08, and $p_{\mathrm{T}}(\mu_{tag})$>20 GeV with no isolation cut are checked. For uncertainty in the pairwise filter efficiency, usage of an alternative simulated sample ($\mathrm{t\bar{t}}$) is checked. Total uncertainty of legs and pairwise filters are less than 1% in all kinematic range of measurement. The resulting efficiency is shown in Fig. 4.4 and Table 4.7.

Table 4.7: Pairwise filter efficiency of dimuon triggers

Data Efficiency	MC Efficiency	SF
0.9794±0.0006	0.9894±0.0005	0.9899±0.0008

In case of eμ triggers, trigger efficiency is measured using eμ events passing offline identification criteria, which is enriched with $\mathrm{t\bar{t}}$ events. Each leg efficiency is measured with the tag and probe method, and pairwise filter efficiency is measured using the reference triggers. Events with exactly one opposite-sign eμ pair with $\Delta R(\mathrm{e},\mu) > 0.4$ are used for the measurement.

For efficiency measurement of the electron leg, events firing the single muon trigger are used, and tag muons are required to pass the last filter of the trigger and have $p_{\mathrm{T}} > 27$ GeV. Passing probes for the electron leg are required to fire the last filter of electron leg sequence before the pairwise filter. For efficiency

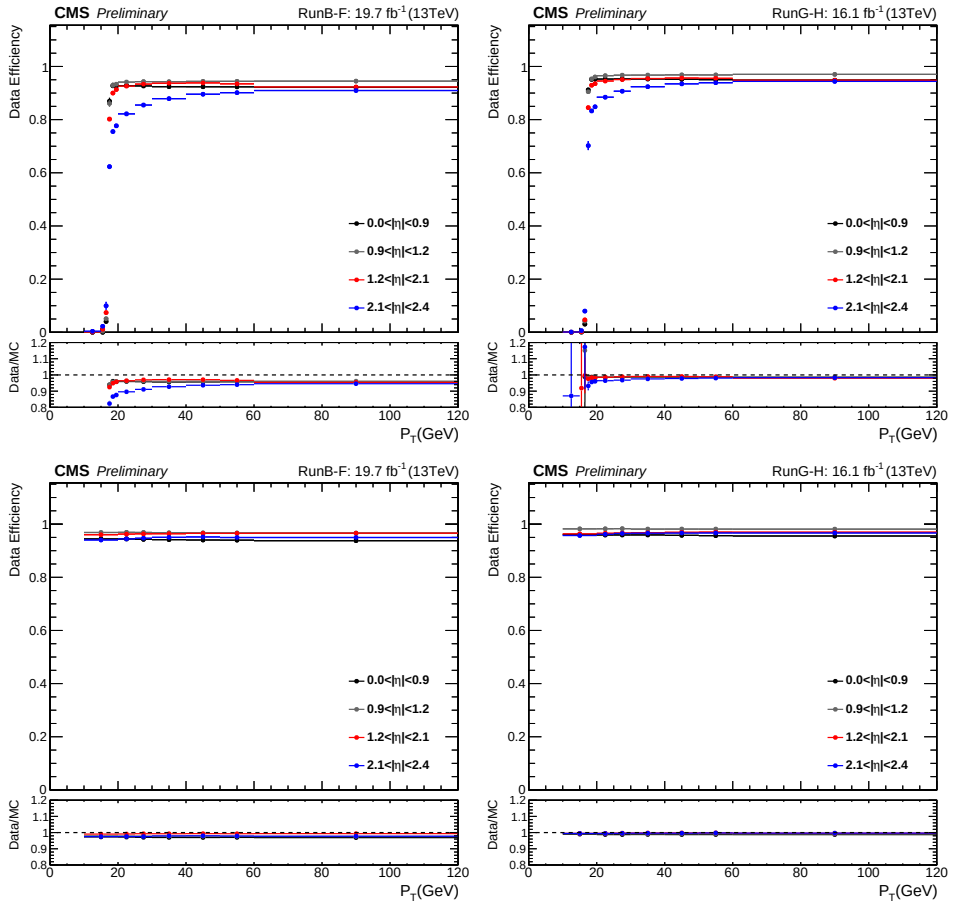

Figure 4.4: Efficiency of the first leg of dimuon triggers in the period B-F (left, upper row) and G-H (right, upper row), and those of the second leg in the period B-F (left, bottom row) and G-H (right, bottom row)

measurement of the muon leg, events firing the single electron trigger are used, and tag electrons are required to have $p_{\mathrm{T}} > 30\,\mathrm{GeV}$ and fire the single electron trigger. Passing probes for the muon leg are required to fire the last filter of muon leg sequence before the pairwise filter. For the measurement of pairwise filter efficiency, events firing reference triggers without the pairwise filters are used. Electrons and muons are required to be $p_{\mathrm{T}}(\mathrm{e}) > 25\,\mathrm{GeV}$, $p_{\mathrm{T}}(\mu) > 10\,\mathrm{GeV}$, and pass the last filter of the electron and muon leg sequences. Passing events are required to have electron and muon passing the pairwise filter of the trigger.

Systematic uncertainty in each leg efficiency is estimated from alternative tag and simulated sample conditions. For the tag variations, the tag is required to pass $p_{\mathrm{T}}(\mu)$>35 GeV and I^{μ}_{rel}<0.1 for tag muons, and pass $p_{\mathrm{T}}(\mathrm{e})$>40 GeV and $|\eta(\mathrm{e})|$<2.1 for tag electrons. For an alternative simulated sample, dielectron events from Z boson decays are used. The largest source of uncertainty in the leg efficiency is statistical uncertainty, and the subleading source is the process dependency observed at high p_{T}. The magnitude of total uncertainty in filter efficiency is typically 1-2%. For uncertainty of pairwise filters, statistical uncertainty and the alternative simulated sample are considered, but the variation was minor, and total uncertainty is dominated by the statistical uncertainty. The resulting efficiency is shown in the Fig. 4.5, 4.6, and the Table 4.8.

Table 4.8: Pairwise filter efficiency of eμ triggers

Data Efficiency	MC Efficiency	SF
0.962±0.005	0.991±0.002	0.970±0.005

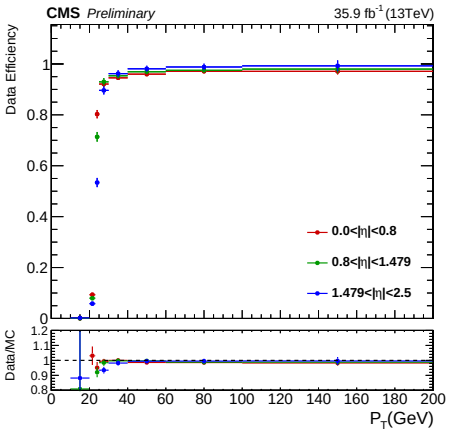

Figure 4.5: Electron leg efficiency of eμ triggers

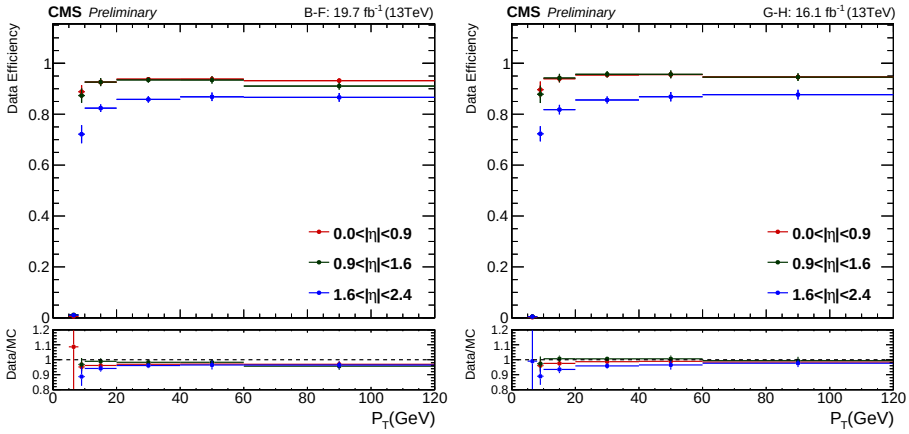

Figure 4.6: Muon leg efficiency of eμ triggers in the period B-F (left) and G-H (right)

4.4.3 Trigger Efficiency Correction

Method

Trigger efficiency is formulated with the efficiency of leg and pairwise filters forming the dilepton triggers. The formulation depends on the number of leptons in events. Trigger efficiency of multilepton events passing dilepton triggers are modelled as follows. The $\varepsilon_{\text{pair}}$ can be replaced with 1 for those without pairwise filters.

1. Trigger efficiency of dilepton events

   (a) Electron-muon trigger efficiency of eμ events

   $$\varepsilon(\text{e},\mu) = \varepsilon_{\text{e}}(\text{e})\varepsilon_{\mu}(\mu)\varepsilon_{\text{pair}} \tag{4.5}$$

   (b) Dimuon trigger efficiency of dimuon events

   $$\varepsilon(\mu_1,\mu_2) = \varepsilon_{\text{leg1}}(\mu_1)\varepsilon_{\text{leg2}}(\mu_2)\varepsilon_{\text{pair}} \tag{4.6}$$

2. Trigger efficiency of trilepton events

   (a) Electron-muon trigger efficiency of e$\mu\mu$ events

   $$\varepsilon(\text{e},\mu_1,\mu_2) = \varepsilon_{\text{e}}(\text{e})\left\{\varepsilon_{\mu}(\mu_1)\varepsilon_{\text{pair}} + (1-\varepsilon_{\mu}(\mu_1)\varepsilon_{\text{pair}})\varepsilon_{\mu}(\mu_2)\varepsilon_{\text{pair}}\right\} \tag{4.7}$$

   (b) Dimuon trigger efficiency of $\mu\mu\mu$ events

   $$\begin{aligned}\varepsilon(\mu_1,\mu_2,\mu_3) =& \varepsilon_{\text{leg1}}(\mu_1)\left\{\varepsilon_{\text{leg2}}(\mu_2)\varepsilon_{\text{pair}} + (1-\varepsilon_{\text{leg2}}(\mu_2)\varepsilon_{\text{pair}})\varepsilon_{\text{leg2}}(\mu_3)\varepsilon_{\text{pair}}\right\} \\ &+ (1-\varepsilon_{\text{leg1}}(\mu_1))\varepsilon_{\text{leg1}}(\mu_2)\varepsilon_{\text{leg2}}(\mu_3)\varepsilon_{\text{pair}}\end{aligned} \tag{4.8}$$

Then the scale factor for the efficiency correction is calculated as a ratio of trigger efficiency in data and simulation, each of which is calculated following the described formulae:

$$SF = \frac{\varepsilon_{\mathrm{DATA}}(\ell_1, \ell_2, ...)}{\varepsilon_{\mathrm{MC}}(\ell_1, \ell_2, ...)} \tag{4.9}$$

Validation of the Method

There are a few assumptions lying beneath the approach. For example, the method assumes each leg efficiency on a particular object is independent of other objects in the event (e.g. $\varepsilon_{\mathrm{e}}(\mathrm{e}|\mu) = \varepsilon_{\mathrm{e}}(\mathrm{e})$), so that the total efficiency can be factorized to leg and filter efficiency. Full correlation of leg decisions on a particular object is also assumed. For example, if the leading muon failed the leading leg, then it cannot pass other leg filters as well. Also no correlation between the tag and probe in measurements is assumed. In order to make sure measured leg and filter efficiencies combined with previous formulae based on such assumptions can describe the total trigger efficiencies of background and signal processes, a closure test is performed for the trigger efficiency.

In this test, the observed efficiency of trigger simulation is compared with the expected efficiency of simulation calculated from the measured leg and filter efficiency and the efficiency formulae.

$$\varepsilon_{\mathrm{exp}} = \frac{\Sigma_{\text{All Evt}} w_i \varepsilon_{i,\mathrm{Trig}}(\ell_1, \ell_2, ...)}{\Sigma_{\text{All Evt}} w_i}, \quad \varepsilon_{\mathrm{obs}} = \frac{\Sigma_{\text{Pass Trig}} w_i}{\Sigma_{\text{All Evt}} w_i} \tag{4.10}$$

$\varepsilon_{i,\mathrm{Trig}}$ represents the expected trigger efficiency of an event i calculated from formulae in the previous section, and w_i represents the applied weight, which is a product of generator weights of simulated events and the pile-up weight. The test is performed on selected events above trigger thresholds: $p_{\mathrm{T}}(\mu)$>10 and

p_T(e)>25 (GeV) for eμ triggers, $p_T(\mu)$>20 and 10 GeV for leading and other muons for dimuon triggers.

As shown in Table 4.9 and 4.10, a good prediction of the trigger efficiency of signal and background events are observed from filter efficiencies measured using DY and $t\bar{t}$ simulated samples. Hence, the approach of factorized filter efficiency is expected to be valid for the description of background and signal processes.

Table 4.9: Closure tests of trigger efficiency of dilepton events with statistical uncertainty

		Non-DZ Path		DZ Path	
		Observed	Expected	Observed	Expected
$\mu\mu$	DY	0.947	0.940±0.0009	0.937	0.930±0.001
	$t\bar{t}$	0.952	0.941±0.002	0.942	0.931±0.002
eμ	DY	0.896	0.897±0.014	0.886	0.889±0.017
	$t\bar{t}$	0.923	0.922±0.014	0.914	0.914±0.018

Table 4.10: Closure tests of trigger efficiency of trilepton events with statistical uncertainty. In case of signal, numbers in parentheses represent the masses of particles in GeV.

		Non-DZ Path		DZ Path	
		Observed	Expected	Observed	Expected
$\mu\mu\mu$	WZ	0.994	0.996±0.006	0.994	0.995±0.006
	$t\bar{t}Z$	0.998	0.997±0.006	0.997	0.996±0.006
	H^+(100),A(15)	0.997	0.993±0.012	0.996	0.992±0.012
	H^+(160),A(35)	0.998	0.996±0.007	0.998	0.995±0.007
e$\mu\mu$	WZ	0.971	0.969±0.012	0.964	0.969±0.012
	$t\bar{t}Z$	0.973	0.973±0.011	0.966	0.972±0.012
	H^+(100),A(15)	0.972	0.970±0.016	0.964	0.969±0.016
	H^+(160),A(35)	0.972	0.971±0.012	0.966	0.970±0.012

4.4.4 Validation of Corrections on Physics Objects

The validity of various corrections on physics objects applied in the analysis are checked in dilepton event regions. The result is shown in Fig. 4.7 and 4.8. Statistical uncertainty of simulated samples and uncertainty in the production cross sections and integrated luminosity is overlaid on the plots. Overall, the simulated samples after various corrections provide decent description of data.

Dimuon control region

Event selection:

- Pass dimuon triggers,
- opposite-sign dimuon with $p_{\mathrm{T}} > 20, 10\,\mathrm{GeV}$,
- $M(\mu\mu) > 50\,\mathrm{GeV}$.

Purpose: Validation of corrections applied on muons and dimuon triggers.

Electron-muon control region

Event selection:

- Pass eμ triggers,
- opposite sign eμ pair with $p_{\mathrm{T}}(\mathrm{e}) > 25\,\mathrm{GeV}$, $p_{\mathrm{T}}(\mu) > 10\,\mathrm{GeV}$, and $\Delta R(\mathrm{e}, \mu) > 0.4$,
- $N_{jets} \geq 2$.

Purpose: Validation of corrections applied on muons, electrons, electron-muon triggers, jets, b-tagging, and $E_{\mathrm{T}}^{\mathrm{miss}}$.

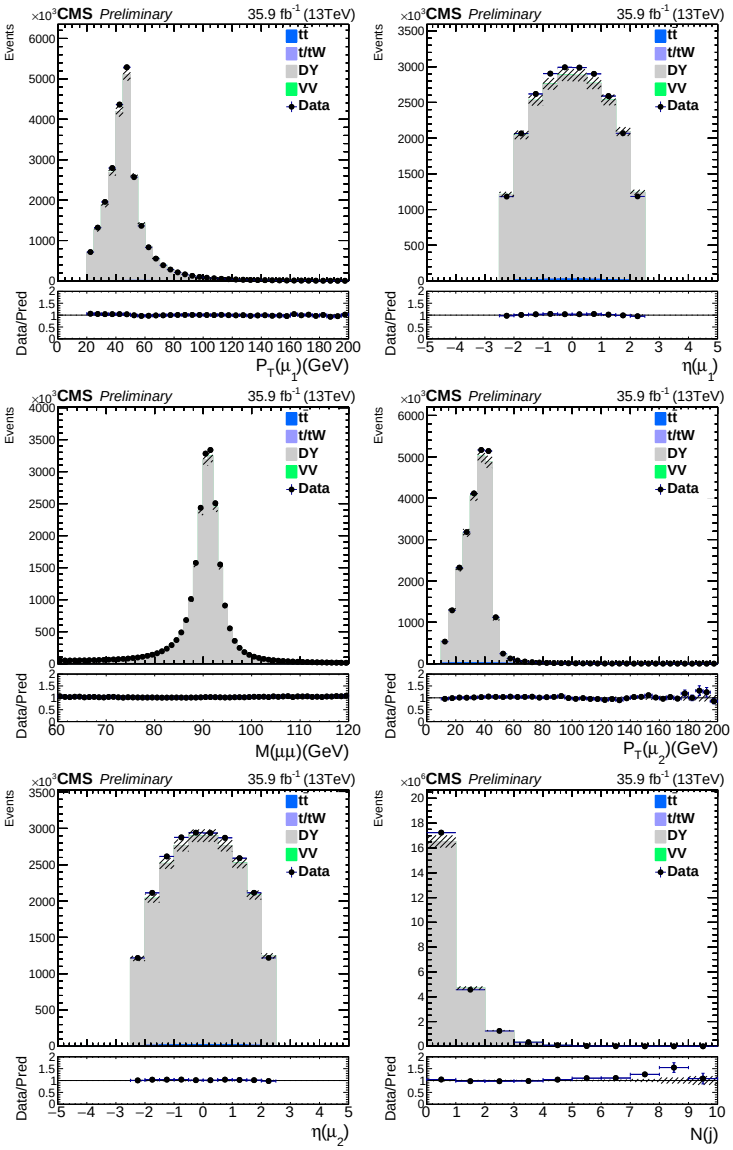

Figure 4.7: Kinematic distributions of physics objects in dimuon events.

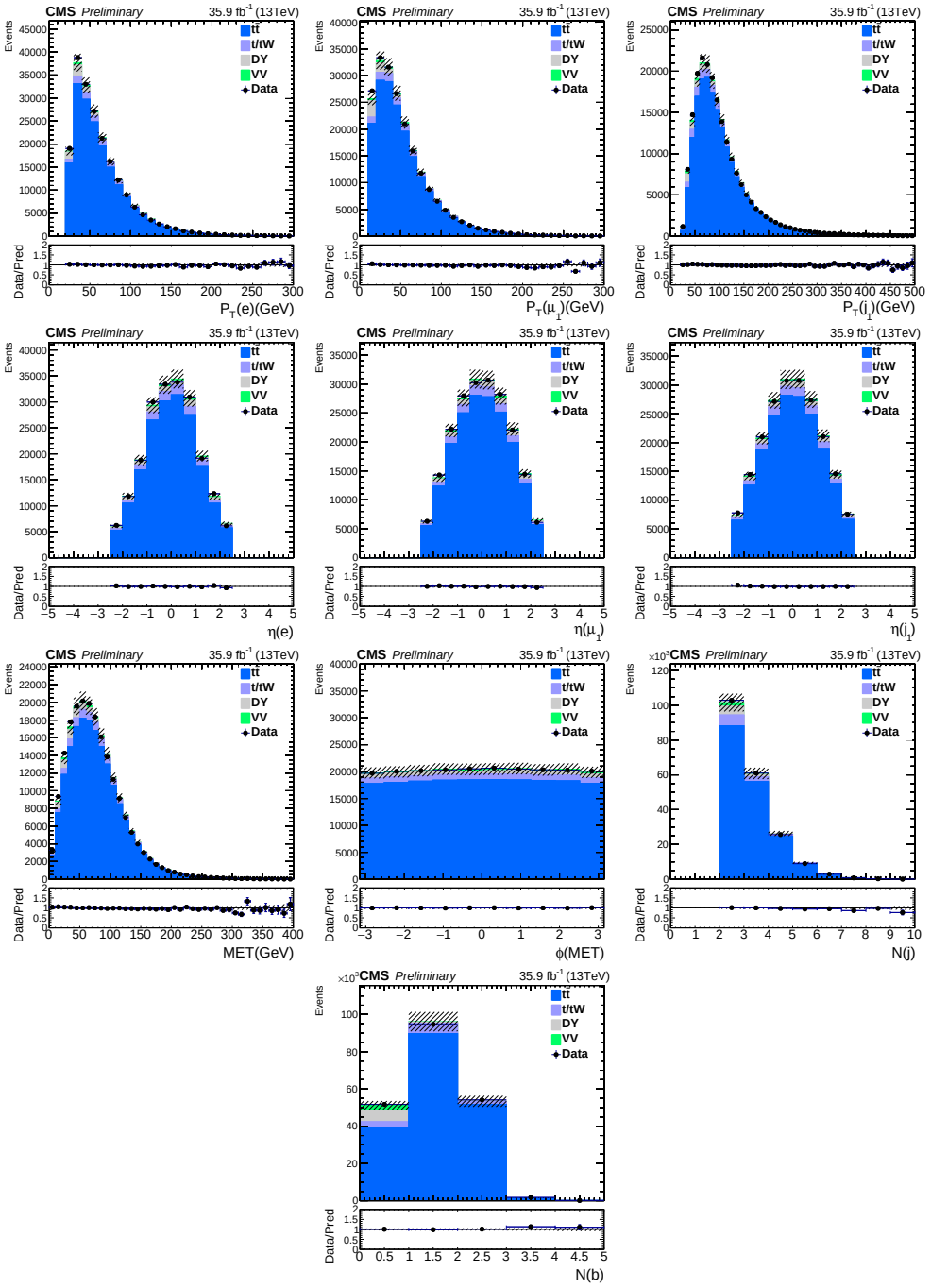

Figure 4.8: Kinematic distributions of physics objects in electron-muon events.

4.5 Event Selection

4.5.1 Baseline Selection

The baseline selection for the signal events is determined from kinematic characteristics of signal and background processes to maximize the sensitivity with a minimum loss of signal efficiency for the mass range considered in the search. Leading and subleading lepton p_{T} selections are motivated from trigger thresholds, and the trailing muon p_{T} cut is motivated for suppression of nonprompt muon backgrounds and limitations in the muon identification. Typical p_{T} scale of jet constituent tracks is about a few GeV [147], hence low-p_{T} lepton regions are dominated with nonprompt lepton backgrounds. In a study based on simulation, inclusion of muons below 10 GeV worsened the expected search sensitivity in many of signal hypotheses. Besides, muons with a p_{T} scale of a few GeV exhibits a reduced hit efficiency in the muon system, especially in the outermost stations, and suffers from multiple scatterings in the steel yoke, leading to a decrease in the reconstruction and identification efficiency. The tight criteria of the standard CMS muon identification reaches its plateau of efficiency at p_{T} value of 10 GeV [141].

In addition to lepton p_{T} cuts, the invariant mass of an opposite-sign muon pair is required to be larger than 12 GeV and distant from the Z boson mass by at least 10 GeV, in order to reject backgrounds with the Z boson and low-mass vector meson resonances. Events are further required to include two or more jets, among which at least one jet is b-tagged, to suppress electroweak diboson backgrounds, which have a low jet multiplicity and does not involve b quarks. These selections rejects the DY+jets and electroweak diboson processes, which are the dominant backgrounds to the inclusive trilepton production, to a negligible level. Remaining backgrounds are dominated by $\mathrm{t\bar{t}}$ process, with a

minor contribution from $t\bar{t}$ + W/Z/H processes. The baseline selection of the signal region can be summarized as follows:

- include exactly three leptons, 1e2μ or 3μ,
- include an opposite-sign muon pair,
- p_{T}(e)>25 GeV (1e2μ) and $p_{\mathrm{T}}(\mu)$>20 GeV (3μ, leading muon),
- M($\mu\mu$) > 12 GeV for all opposite-sign muon pairs,
- |M($\mu\mu$) − 91.2|>10 GeV for all opposite sign muon pairs,
- $N_{\mathrm{b\ tags}} \geq 1$,
- $N_{\mathrm{jets}} \geq 2$.

The impact of these selections on the signal and background rates are summarized in Table 4.11, 4.12, 4.13, and 4.14. The DY and $t\bar{t}$ rates are estimated using simulated samples with mis-identified leptons. In order to illustrate the impact of lower muon p_{T} thresholds on physics processes, event rates with the trailing muon p_{T} cut at 5 GeV is also shown in the tables. No lepton efficiency correction is applied in the values, as the corrections are measured using prompt leptons from Z boson decays and are not valid for fake or nonprompt leptons in jets. Besides, the magnitude of efficiency corrections on prompt leptons is about a few percent, hence it does not change the overall behavior. The lower invariant mass cut, M($\mu^+\mu^-$)>12 GeV, is applied in all steps. The uncertainty values shown in the tables are statistical uncertainty in estimation.

Table 4.11: Evolution of event yields of major background processes in 3μ channel with the baseline selection.

Selection	Source						
	DY(fake)	WZ	Zγ	$t\bar{t}$ (fake)	$t\bar{t}Z$	$t\bar{t}W$	$t\bar{t}H$
p_T >20,10,5 GeV	9608±282	2786±16	818±24	560±15	97.0±0.5	14.9±0.2	10.5±0.1
p_T >20,10,10 GeV	2429±135	2554±16	791±22	347±12	91.5±0.5	13.7±0.2	9.3±0.1
Z Veto	437±87	401±6	636±20	259±10	16.8±0.2	10.5±0.2	6.6±0.1
$N_{b\ tags}\geq 1$	32.3±10.7	9.5±1.0	18.8±3.8	140±8	12.9±0.2	7.9±0.2	5.1±0.1
$N_{jets}\geq 2$	13.6±5.9	5.4±0.7	6.9±2.3	79.5±5.7	12.6±0.2	6.8±0.2	5.0±0.1

Table 4.12: Evolution of event yields of signal processes in 3μ channel with the baseline selection (σ_{signal}=20fb).

Selection	Source				
	H^+(100) A (15)	H^+(160) A (15)	H^+(130) A (45)	H^+(160) A (45)	H^+(160) A (75)
p_T >20,10,5 GeV	19.9±0.2	42.2±0.3	40.0±0.3	48.1±0.3	52.1±0.3
p_T >20,10,10 GeV	13.6±0.2	35.7±0.2	34.9±0.2	42.3±0.3	49.7±0.3
Z Veto	12.5±0.1	29.5±0.2	32.1±0.2	35.4±0.2	43.4±0.3
$N_{b\ tags}\geq 1$	9.2±0.1	16.9±0.2	22.2±0.2	20.1±0.2	24.7±0.2
$N_{jets}\geq 2$	8.7±0.1	15.5±0.2	21.0±0.2	18.5±0.2	22.6±0.2

Table 4.13: Evolution of event yields of major background processes in 1e2μ channel with the baseline selection.

Selection	Source						
	DY(fake)	WZ	Zγ	$t\bar{t}$ (fake)	$t\bar{t}Z$	$t\bar{t}W$	$t\bar{t}H$
p_T >25,10,5 GeV	358±53	1583±12	1042±27	347±12	63.2±0.4	18.0±0.2	10.8±0.2
p_T >25,10,10 GeV	281±44	1492±12	854±24	220±10	61.0±0.4	17.0±0.2	9.8±0.1
Z Veto	61±27	279±5	622±21	187±9	15.7±0.2	14.8±0.2	8.5±0.1
$N_{b\ tags}\geq 1$	0±0	7.0±0.8	9.9±3.4	101±6	11.9±0.2	11.3±0.2	6.6±0.1
$N_{jets}\geq 2$	0±0	3.6±0.6	8.0±2.7	58±5	11.5±0.2	9.8±0.2	6.4±0.1

Table 4.14: Evolution of event yields of signal processes in 1e2μ channel with the baseline selection (σ_{signal}=20fb).

Selection	Source				
	H^+(100) A (15)	H^+(160) A (15)	H^+(130) A (45)	H^+(160) A (45)	H^+(160) A (75)
p_T >25,10,5 GeV	11.9±0.1	25.6±0.2	23.5±0.2	29.2±0.2	29.7±0.2
p_T >25,10,10 GeV	7.8±0.1	21.9±0.2	21.1±0.2	26.3±0.2	29.2±0.2
Z Veto	7.8±0.1	21.6±0.2	21.0±0.2	26.1±0.2	29.1±0.2
$N_{b\ tags}\geq 1$	5.7±0.1	12.2±0.1	14.6±0.2	14.6±0.2	16.5±0.2
$N_{jets}\geq 2$	5.5±0.1	11.2±0.1	13.8±0.2	13.5±0.2	15.1±0.2

4.5.2 Selections Dependent on Signal Hypotheses

Variable for Signal Extraction

The signal process consists of a cascade decay of a top quark with three intermediate resonant bosons, H^+, W, and A, hence resonant invariant mass distributions can be observed in signal events for various combinations of physics objects. The most intuitive choice for the signal extraction would include the reconstructed mass of H^+ and A bosons. As shown in Fig. 4.9, the H^+ boson decay, $H^+ \to W^+A \to W^+\mu^+\mu^-$, yields resonances in invariant mass distributions of $\mu\mu$jj and $\mu\mu\ell\nu$ systems for hadronic and leptonic W boson decays, respectively. These distributions exhibit resonant distributions with very large widths and long high-mass tails, and they are spread over ranges of several hundred GeV. In the figures, the jet pair with its invariant mass value closest to the W boson mass is chosen, and the neutrino momentum is constructed using the constraints of W boson mass on the lepton momentum and $\vec{p}_{\mathrm{T}}^{\,\mathrm{miss}}$. The muon selection in 3μ events is discussed in the later part of the section. The broad distribution originates from the large resolution of jet energy and $E_{\mathrm{T}}^{\mathrm{miss}}$ values, and combinatorials for the jet assignments contribute to the long high-mass tail.

The A boson decay, $A \to \mu^+\mu^-$, on the other hand, produces a narrow resonance in the invariant mass distribution of a muon pair, spread within a range between a few hundred MeV and few GeV. As can be seen in the figure, the signal distribution is very clearly distinguished from non-resonant background spread over a few hundred GeV, in contrast with the reconstructed H^+ boson mass. For this reason, the dimuon invariant mass is considered as the variable for the signal extraction.

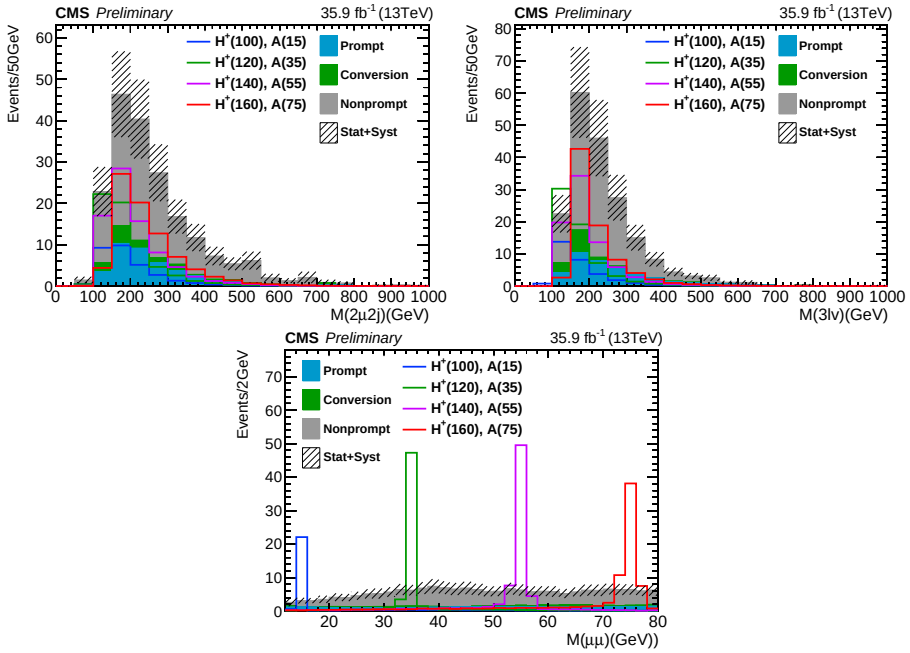

Figure 4.9: Distributions of invariant mass of $\mu\mu$jj (upper left), $\mu\mu\ell\nu$ (upper right), and $\mu\mu$ (bottom) systems for the H^+ and A boson decays (1e2μ+3μ). The signal cross section is assumed to be 50fb.

Selection of Muon Pairs

In each events of the baseline selection, a muon pair is selected to reconstruct the A boson mass. In 1e2μ events, the opposite-sign muon pair is considered as candidate objects from A $\to \mu^+\mu^-$ decay. In 3μ events, where an ambiguity in assignment exists, the candidate muon pair is determined from the p_{T} order and the consistency of transverse mass, $\mathrm{M_T}(\ell, \vec{p}_{\mathrm{T}}^{\,\mathrm{miss}})$, with W bosons. In this analysis, the transverse mass of a lepton and $\vec{p}_{\mathrm{T}}^{\,\mathrm{miss}}$ system is defined as,

$$\mathrm{M_T}(\ell, \vec{p}_{\mathrm{T}}^{\,\mathrm{miss}}) = \sqrt{2(|\vec{p}_{\mathrm{T}}^{\,\ell}||\vec{p}_{\mathrm{T}}^{\,\mathrm{miss}}| - \vec{p}_{\mathrm{T}}^{\,\ell} \cdot \vec{p}_{\mathrm{T}}^{\,\mathrm{miss}})} \tag{4.11}$$

where the $\vec{p}_{\mathrm{T}}^{\,\ell}$ is the projection of the lepton momentum on the transverse plane. Three muons with an opposite charge pair include two muons with same charges. In signal events, they are produced from decays of the A and W bosons with different top quark origins. The muon with a lower and higher p_{T} value is assigned to the A and W bosons, respectively. When the p_{T} difference between them is less than 25 GeV and only one of them produces the transverse mass consistent with the W boson, $50<\mathrm{M_T}(\ell, \vec{p}_{\mathrm{T}}^{\,\mathrm{miss}})<120$ GeV, then the muon with the transverse mass inconsistent with the W boson is assigned to the A boson. The assignment is motivated from features that muons originating from A bosons generally have transverse momentum and transverse mass lower than muons from W boson decays in many of the signal hypotheses, as can be seen in Fig. 4.10. The cut values are determined to be about the average value of cuts that maximize accuracy in each of mass hypothesis. The assignment accuracy in the baseline selection is generally 60–80% depending on H^+ and A mass hypotheses, as shown in Fig. 4.11.

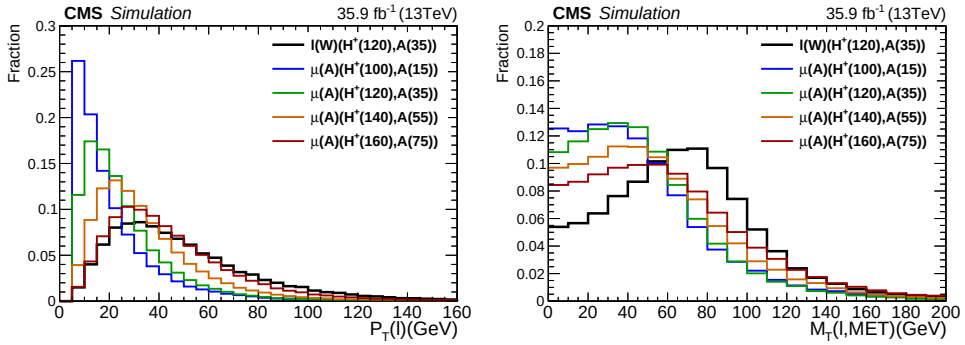

Figure 4.10: The p_{T} and $\mathrm{M_T}(\ell, \vec{p}_{\mathrm{T}}^{\,\mathrm{miss}})$ distributions of muons from A and W boson decays, respectively.

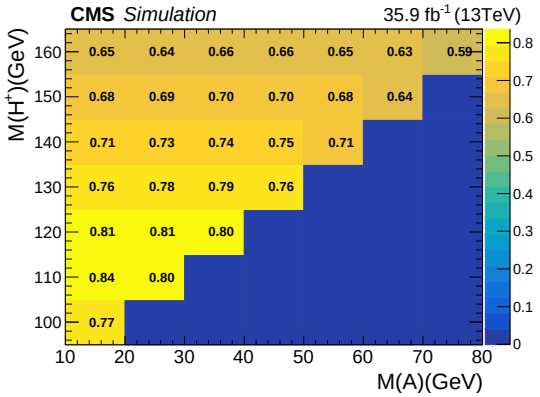

Figure 4.11: Accuracy of muon-pair assignments to the A boson in 3μ events.

Mass Windows for Signal Extraction

Presence of the targeted signal process is examined by counting number of events within mass windows centered at A boson mass hypotheses. The width values of mass windows are optimized at mass points where the simulated signal samples are produced (simulation points), and the width values for the m_{A} values between the simulation points are determined by linear interpolation. The width values are optimized to maximize the expected median significance, $\sqrt{2[(n_{\mathrm{s}}+n_{\mathrm{b}})\ln(1+n_{\mathrm{s}}/n_{\mathrm{b}})-n_{\mathrm{s}}]}$ [148], where the n_{s} and n_{b} are the number of signal and background events in a mass window. This expression holds down to a very small number where an approximation of a Gaussian distribution is not valid, and it converges to the expectation from the approximation, $n_{\mathrm{s}}/\sqrt{n_{\mathrm{b}}}$ in the limit of large $n_{\mathrm{s}}+n_{\mathrm{b}}$ and small $n_{\mathrm{s}}/n_{\mathrm{b}}$ values. The signal cross section is assumed to be 20 fb in the optimization, yet the dependence of optimum cut values on the signal rates is observed to be small, as can be seen in examples in Fig. 4.12. In addition, the optimal size of mass windows are observed to be similar, implying that the search sensitivity is mainly determined near the A mass resonance, and the impact of mis-assigned muon pairs on the window size for 3μ events is small. Hence, the same mass window is used in both final states for a given m_{A} value. The width values of mass windows corresponds to 1.9–3.3 times a resolution of dimuon invariant mass for the m_{A} values considered.

The acceptance of mass windows is approximately 80–90% for $1\mathrm{e}2\mu$ events and 50–70% for 3μ events. For a correctly assigned muon pair, the mass window acceptance varies in 83–93%, but additional degradation of efficiency arises from wrong assignments of muon pairs in 3μ events and contributions from $\mathrm{WW} \to 2\ell 2\nu$ decays of signal, in which one of the four leptons is not within detector acceptance or fails identification.

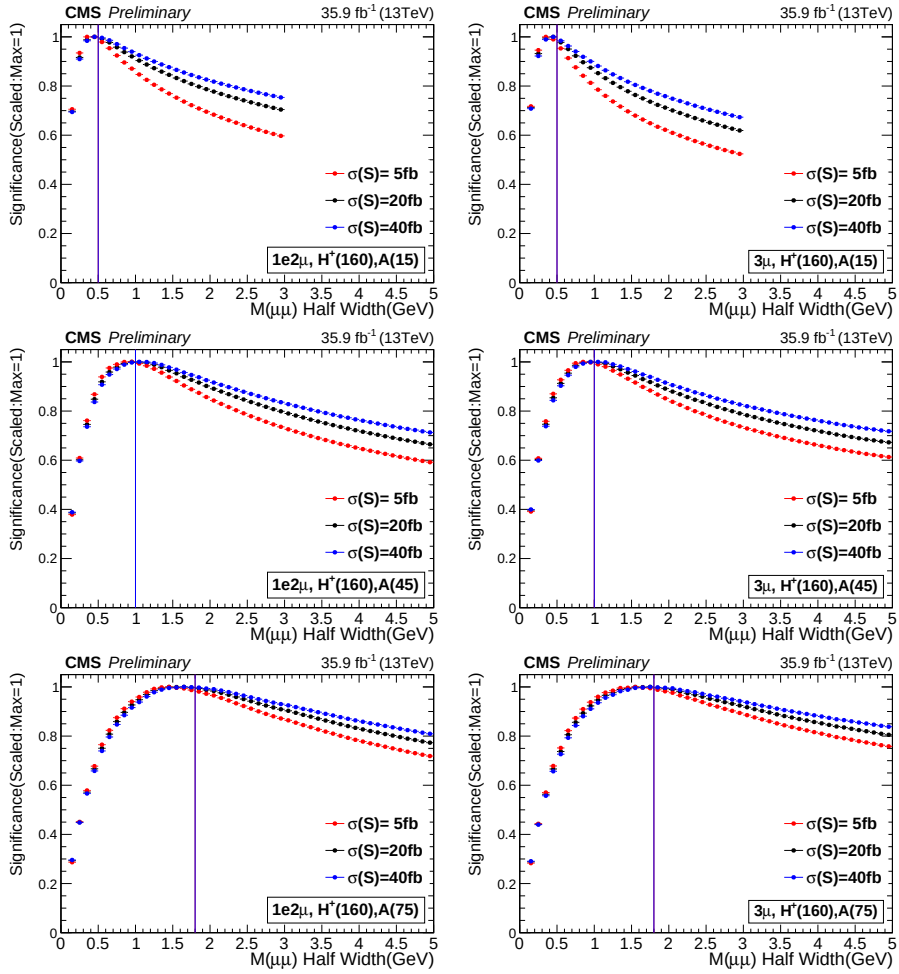

Figure 4.12: Normalized median significance as a function of half width of mass windows. The chosen sizes of windows are shown with vertical lines.

Centers of the mass windows in between simulation points are determined to ensure any m_{A} values within the search range can be covered with at least 95% of mass window acceptance at adjacent bin centers. The mass steps between the centers of mass windows vary in the range of 0.45–1.15 GeV, corresponding to 1.2–3 times the resolution of dimuon invariant mass for the m_{A} values. In total, 95 mass windows are placed between 15 and 75 GeV, which is summarized in Table 4.15

Selection Efficiency of Signal Events

Selection efficiency of signal events are modeled using simulated samples, and those at m_{H^+} and m_{A} values in between simulation points are determined by interpolation, based on the Delaunay triangulation and barycentric coordinates [149–151]. The method reduces to the usual linear interpolation for efficiency values along a line connecting two adjacent simulation points on the mass plane. In the configuration of simulation points, the method has up to two-fold ambiguity in interpolation, yet the relative difference between them is typically as small as 1–2%. Hence, the nominal value is determined as the average of the two values, and conservatively, a systematic uncertainty of 5% is assigned on the interpolated efficiency values from their maximal difference.

In addition, validity of interpolation in the mass window acceptance is tested using an alternative method. In this test, the signal distribution is modeled as an analytic function, and interpolation of internal parameters that best fits the distributions at the simulation points provide the signal shape on the entire mass plane. The mass window acceptance at the 95 mass windows can be calculated from the integration of these signal probability density functions within the window ranges, and the resulting values agreed with the efficiency values directly interpolated from the simulation points. More details on this study can

Table 4.15: Definition of dimuon mass windows (unit: GeV).

Bin Index	1	2	3	4	5	6	7	8
Center	15	15.45	15.9	16.35	16.8	17.25	17.7	18.15
±Range	0.5	0.509	0.518	0.527	0.536	0.545	0.554	0.563
Bin Index	9	10	11	12	13	14	15	16
Center	18.6	19.05	19.5	19.95	20.4	20.85	21.3	21.75
±Range	0.572	0.581	0.59	0.599	0.608	0.617	0.626	0.635
Bin Index	17	18	19	20	21	22	23	24
Center	22.2	22.65	23.1	23.55	24	24.45	24.9	25
±Range	0.644	0.653	0.662	0.671	0.68	0.689	0.698	0.7
Bin Index	25	26	27	28	29	30	31	32
Center	25.55	26.1	26.65	27.2	27.75	28.3	28.85	29.4
±Range	0.7055	0.711	0.7165	0.722	0.7275	0.733	0.7385	0.744
Bin Index	33	34	35	36	37	38	39	40
Center	29.95	30.5	31.05	31.6	32.15	32.7	33.25	33.8
±Range	0.7495	0.755	0.7605	0.766	0.7715	0.777	0.7825	0.788
Bin Index	41	42	43	44	45	46	47	48
Center	34.35	34.9	35	35.6	36.2	36.8	37.4	38
±Range	0.7935	0.799	0.8	0.812	0.824	0.836	0.848	0.86
Bin Index	49	50	51	52	53	54	55	56
Center	38.6	39.2	39.8	40.4	41	41.6	42.2	42.8
±Range	0.872	0.884	0.896	0.908	0.92	0.932	0.944	0.956
Bin Index	57	58	59	60	61	62	63	64
Center	43.4	44	44.6	45	45.75	46.5	47.25	48
±Range	0.968	0.98	0.992	1	1.015	1.03	1.045	1.06
Bin Index	65	66	67	68	69	70	71	72
Center	48.75	49.5	50.25	51	51.75	52.5	53.25	54
±Range	1.075	1.09	1.105	1.12	1.135	1.15	1.165	1.18
Bin Index	73	74	75	76	77	78	79	80
Center	54.75	55	55.9	56.8	57.7	58.6	59.5	60.4
±Range	1.195	1.2	1.227	1.254	1.281	1.308	1.335	1.362
Bin Index	81	82	83	84	85	86	87	88
Center	61.3	62.2	63.1	64	64.9	65	66.15	67.3
±Range	1.389	1.416	1.443	1.47	1.497	1.5	1.5345	1.569
Bin Index	89	90	91	92	93	94	95	
Center	68.45	69.6	70.75	71.9	73.05	74.2	75	
±Range	1.6035	1.638	1.6725	1.707	1.7415	1.776	1.8	

be found in Appendix A.

The final selection efficiency, including the branching fractions of W bosons, kinematic acceptance, and experimental efficiency, in each channel of signal events is shown in Fig. 4.13.

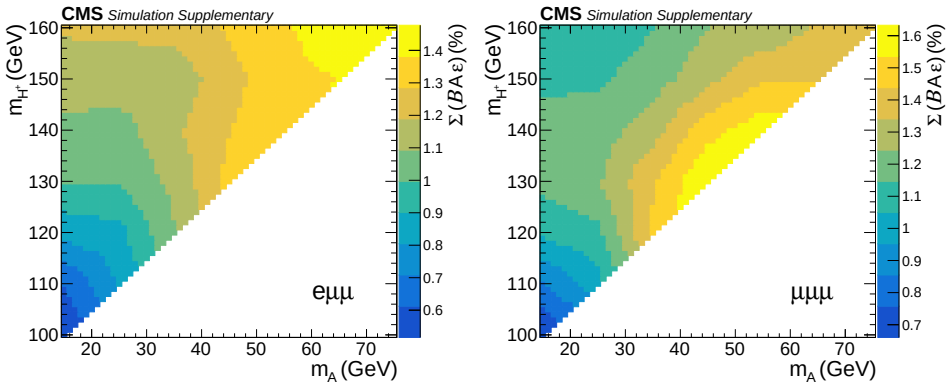

Figure 4.13: Selection efficiency of signal processes in the 1e2μ (left) and 3μ (right) final states. The shown values are relative to the yields before W boson decays, and they include the branching fraction of the two W bosons ($\mathcal{B}$), kinematic acceptance (A), and detection efficiency (ε). All decay modes of the two W bosons are considered in the calculation.

4.6 Background Estimation

Backgrounds of the search are classified as three categories of prompt, nonprompt, and conversions depending on their properties, origins, and methods used for estimation. In this section, the methods used for estimation of these backgrounds are discussed.

4.6.1 Jet-induced Nonprompt Leptons

This class of backgrounds are processes with less than three prompt leptons but pass the event selection by inclusion of at least one jet-induced nonprompt lepton. Fake objects can also be produced in jets, and their contribution is estimated together with nonprompt leptons in the method that will be described in this section. For simplicity, the two terminologies of fake and nonprompt leptons are used in this section without distinction, and they refer to the total jet-induced mis-identified leptons, unless otherwise mentioned. This category of background gives the largest contribution to total background as $\approx 60\%$. In studies of simulation, the dominant source of nonprompt background in the signal selection was observed to be $t\bar{t}$ processes, especially dileptonic $t\bar{t}$ decays.

Estimation Method

These nonprompt lepton backgrounds are estimated with the Tight-to-Loose method [152], also known as the Fake Rate Method. This method estimates amount of nonprompt lepton contribution by extrapolating identification variables from the loose selection to the tight selection with extrapolation factors measured in independent control event regions. The control event region that the extrapolation factor is measured is denoted by 'measurement region' or 'measurement sample', and the control event region with the loose selection

that the extrapolation factor is applied to estimate nonprompt lepton contribution is denoted by 'application region' or 'application sample'. The extrapolation factor is defined as a fraction of objects passing the tight identification relative to objects passing the loose identification, and the extrapolation factor of a nonprompt lepton is referred by 'fake rate', and that of a prompt lepton by 'prompt rate'. Then the composition of observed events ($\vec{N}_{obs}$) categorized by origins of leptons can be connected by a connection matrix constructed from prompt rates ($\varepsilon(p)$) and fake rates ($\varepsilon(f)$). Each element of the connection matrix represents probability that a specific origin composition of prompt and nonprompt leptons entering a particular tight and loose ID composition,

$$\begin{aligned}
\vec{N}_{obs} =& \begin{pmatrix} N_{TTT} & N_{TTL} & N_{TLT} & N_{LTT} & N_{LLT} & N_{LTL} & N_{TLL} & N_{LLL} \end{pmatrix}^{\mathrm{T}}, \\
\vec{N}_{origin} =& \begin{pmatrix} N_{ppp} & N_{ppf} & N_{pfp} & N_{fpp} & N_{ffp} & N_{fpf} & N_{pff} & N_{fff} \end{pmatrix}^{\mathrm{T}}, \\
\vec{N}_{obs} =& \mathbb{M}\vec{N}_{origin},
\end{aligned} \tag{4.12}$$

where elements of the matrix $\mathbb{M}$, connecting the observed ID compositions $N_{ID_1ID_2ID_3}$ and the underlying origin compositions $N_{o_1o_2o_3}$, are expressed as,

$$\mathbb{M}(ID_1, ID_2, ID_3, o_1, o_2, o_3) = \prod_{n \in pass\ T} \varepsilon(o_n) \prod_{m \in fail\ T} (1 - \varepsilon(o_m)). \tag{4.13}$$

The underlying composition can be obtained by applying inverse matrix ($\mathbb{M}^{-1}$) to observed ID composition of loosely selected events. ($\vec{N}_{obs}$). In this analysis, estimation with $\varepsilon(p)$=1 approximation is used, and in that case, the analytic formula for the total contribution of at least one nonprompt lepton to the signal event region can be written as,

$$
\begin{aligned}
N_{\geq 1f} =& \frac{f_1}{1-f_1} N_{LTT} + \frac{f_2}{1-f_2} N_{TLT} + \frac{f_3}{1-f_3} N_{TTL} - \frac{f_1 f_2}{(1-f_1)(1-f_2)} N_{LLT} \\
& - \frac{f_2 f_3}{(1-f_2)(1-f_3)} N_{TLL} - \frac{f_3 f_1}{(1-f_3)(1-f_1)} N_{LTL} \\
& + \frac{f_1 f_2 f_3}{(1-f_1)(1-f_2)(1-f_3)} N_{LLL},
\end{aligned} \tag{4.14}
$$

where f_i is used in the places of $\varepsilon(f_i)$ for convenience.

The fake rate can vary depending on the p_{T} and η values of a lepton, and in consideration of this, the event rates of nonprompt lepton background in each signal bin is estimated with usage of event weights on the application region,

$$
\begin{aligned}
w_i =& \frac{f_1}{1-f_1} \delta_{i,LTT} + \frac{f_2}{1-f_2} \delta_{i,TLT} + \frac{f_3}{1-f_3} \delta_{i,TTL} - \frac{f_1 f_2}{(1-f_1)(1-f_2)} \delta_{i,LLT} \\
& - \frac{f_2 f_3}{(1-f_2)(1-f_3)} \delta_{i,TLL} - \frac{f_3 f_1}{(1-f_3)(1-f_1)} \delta_{i,LTL} \\
& + \frac{f_1 f_2 f_3}{(1-f_1)(1-f_2)(1-f_3)} \delta_{i,LLL},
\end{aligned} \tag{4.15}
$$

where $\delta_{i,j}$ is the Kronecker delta function.

The above expression is also used for calculation of binned distributions of nonprompt lepton backgrounds. As can be seen in the analytic formula, the estimation does not utilize the signal region events, N_{TTT}, but only the application region events. This ensures the statistical independence between the signal region events and this data-driven estimation of nonprompt lepton background.

Modeling of Identification Sidebands

Types of identification variables and their sideband ranges are designed to reduce systematic uncertainty in fake rates, originating from parton flavors

and energy scales of jets. The impact of mother jet flavors on the fake rate is important for electron fake rate, in which the contribution of mis-reconstructed objects in jets are significant when compared to that of nonprompt genuine electrons. Such a mis-reconstructed objects are abundantly produced in light flavor jets, in contrast with nonprompt leptons with small impact parameters which are mostly produced in heavy flavor jets, and the flavor composition of jets producing mis-identified electrons is not dominated by a single jet flavor. Hence, it is desirable to minimize the difference in the fake rate of different jet flavors.

In case of muons, the large material budget up to the last layer of the muon system, 20–27λ_I, and strong magnetic fields on both the inner tracking and muon systems strongly inhibit the possibility of a hadron track penetrating from the inner tracker to the last muon station with a good global track fit and small calorimeter deposits. Mis-identified muons for the tight identification of the analysis are almost purely nonprompt muons from hadron decays in heavy flavor jets, and mis-reconstructed muons are ignorable.

The dependency of electron fake rates on the mother jet flavor is minimized by inclusion of multiple identification variables sensitive to different types of mis-identified leptons. In simulated samples, for a given number of mis-identified electrons per a jet flavor passing tight identification, more nonprompt electrons from heavy flavor jets are observed in the isolation sideband when compared to the mis-reconstructed electrons from light flavor jets. On the other hand, the MVA criteria includes many variables exclusively sensitive to mis-reconstructed cases, hence far more mis-reconstructed electrons from light flavor jets are found in the MVA sideband, when compared to the nonprompt electrons in heavy flavor jets. Thus, by inclusion of sidebands of both variables, the fake rates of different jet flavors becomes similar, as can be seen in Fig. 4.14.

The dependence of fake rates on the mother jet energy scale arises due to the fact that more energetic jets contains more energy around a lepton with a given p_{T} value. To reduce this effect on isolation sidebands, fake rates are parameterized with the cone-corrected momentum, $p_{\mathrm{T}}^{\mathrm{corr}}$, as a proxy of mother jet E_{T}. The $p_{\mathrm{T}}^{\mathrm{corr}}$ variable is defined as,

$$p_{\mathrm{T}}^{\mathrm{corr}} = p_{\mathrm{T}}(1 + \max(0, I_{\mathrm{rel}} - I_{\mathrm{rel}}^{\mathrm{Tight}})), \tag{4.16}$$

where I_{rel} and $I_{\mathrm{rel}}^{\mathrm{Tight}}$ are the relative isolation of a lepton and the cut on the relative isolation in the tight WP of lepton identification.

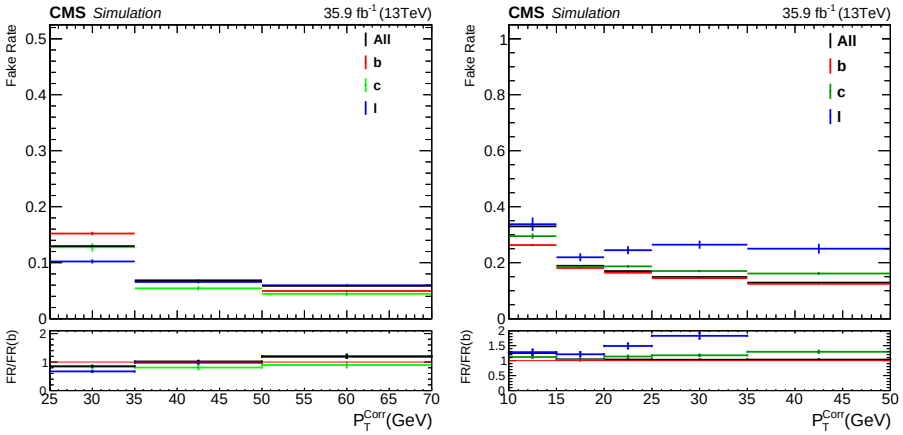

Figure 4.14: Fake rates of electrons (left) and muons (right) after loose ID optimization in $\mathrm{t\bar{t}}$ MC for each flavor of nearby jets, $\Delta R(\ell, \mathrm{j}) < 0.4$.

Measurement of Fake Rates

Fake rates in real data are measured using single lepton events passing the prescaled single lepton triggers listed in Table 4.1. These triggers are chosen to measure the fake rate, as these triggers require online selections similar to the dilepton triggers used for the signal region of this analysis. Event selection of

the measurement region requires the event topology of QCD multijet events. To reduce prompt lepton backgrounds from W boson and $\mathrm{t\bar{t}}$ processes, low $p_{\mathrm{T}}^{\mathrm{miss}}$ and $\mathrm{M_T}(\ell, \vec{p}_{\mathrm{T}}^{\mathrm{miss}})$ is also required. Exact event selection of the measurement region can be summarized as,

- exactly one lepton passing loose WP identification,
- at least one jet with p_{T}>40 GeV and $\Delta R(\ell, \mathrm{j})$>1.0,
- $p_{\mathrm{T}}^{\mathrm{miss}}$<25 GeV, $\mathrm{M_T}(\ell, \vec{p}_{\mathrm{T}}^{\mathrm{miss}})$<25 GeV.

Residual prompt contributions in the event selection are estimated with simulated samples, and these are subtracted in the calculation of fake rates. Normalization factors for simulated samples are measured from an event selection enriched with W boson events, requiring $p_{\mathrm{T}}^{\mathrm{miss}}$>50 GeV, $\mathrm{M_T}(\ell, \vec{p}_{\mathrm{T}}^{\mathrm{miss}})$>70 GeV, and at least one jet with p_{T}>40 GeV. Modeling of the prompt contribution is validated in each of trigger paths, and normalization factors are double checked in an alternative event selection enriched with the Z boson process, $|\mathrm{M}(\ell\ell) - 91.2|$<15 GeV with at least one jet with p_{T}>40 GeV, passing the same triggers, as shown in Fig. 4.15.

The fake rates measured in data are shown in Fig. 4.16. Fake rates of electrons and muons are approximately 0.1–0.2, respectively, in the most of the bins for the loose and tight WP identification. These values will be applied to the sideband of the signal region, the application region, to estimate the event rate of jet-induced nonprompt lepton background in the signal region.

Figure 4.15: $M_T(\ell, \vec{p}_T^{\,miss})$ and $M(\ell\ell)$ distributions in event regions enriched with the W (top) and Z boson (bottom) processes, passing electron (left) and muon triggers with online selections, $p_T > 17\,GeV$ (center) and $p_T > 8\,GeV$ (right).

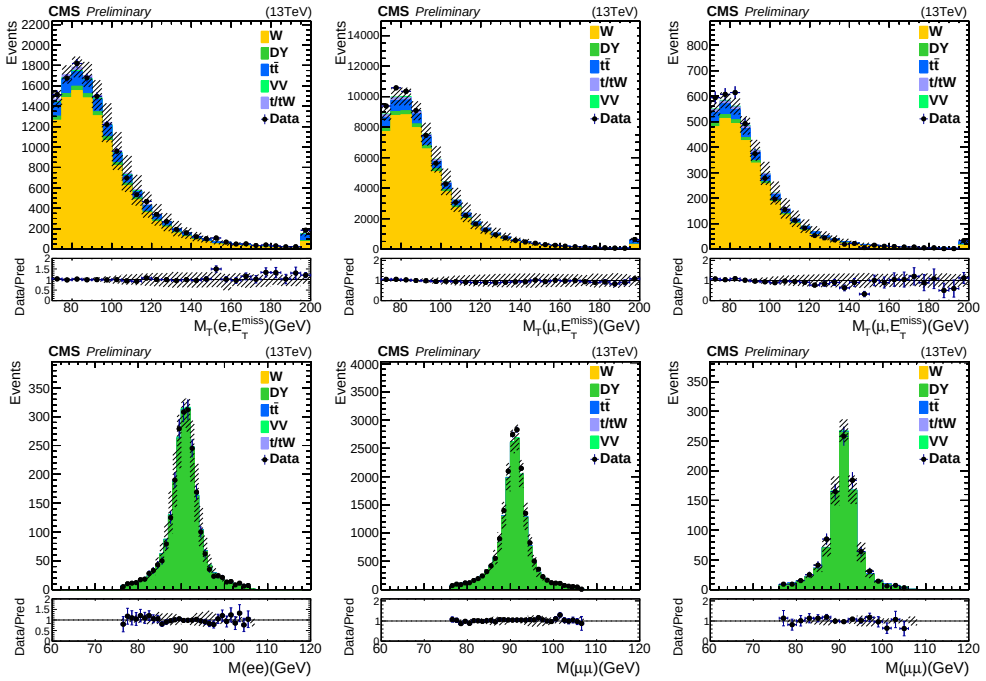

Figure 4.16: Fake rates of electrons (left) and muons (right) measured in data. Error bands include statistical and systematic uncertainties.

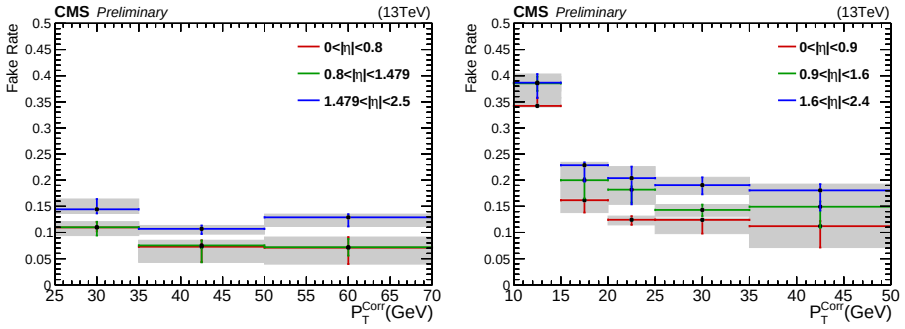

4.6.2 Conversion Leptons

This class of backgrounds are processes with either internal conversion or external conversions of photons. In the thesis, internal conversion refers to processes with a production of a lepton pair via a virtual photon ($\gamma^{*}\to\ell^{+}\ell^{-}$) at the interaction vertex, while external conversion refers to processes with an on-shell photon, converted to a lepton pair inside the detector material. Since the rate of external conversions is proportional to the inverse mass square [138, 153], external conversions are only meaningfully observed for electrons. In case of muons, nearly all simulated events are produced from internal conversions. Since we require that electrons used in the analysis should not be originating from a reconstructed conversion vertex, and veto events with opposite-sign dilepton pair mass below 12 GeV, conversion processes pass the event selection only when either one of the two leptons is not reconstructed or identified. In a simulation study, most of these cases are highly asymmetric conversion that the leading lepton takes most of the photon momentum, and subleading lepton has very small momentum. These processes are estimated with simulation. For this class of background processes, $\mathrm{Z}\gamma^{(*)}$ and $\mathrm{t\bar{t}}\gamma^{(*)}$ are considered.

In case of the $\mathrm{Z}\gamma^{(*)}$ process, normalization of this background is confined in a specific event selection. Conversion of a photon from final state radiation in Z boson decays, $\mathrm{Z}\to\ell^{+}\ell^{-}\gamma^{(*)}\to\ell^{+}\ell^{-}\ell'+X$, forms a shifted Z mass bump in trilepton invariant mass distributions. Hence, events located at this mass bump region are enriched with conversion processes, and these are used to extract correction factors. As the lepton from a photon conversion passing event selection has a momentum similar to the photon, the location of the mass bump is close to the Z boson mass, as can be seen in Fig. 4.17. The $\mathrm{Z}\gamma^{(*)}$ process also have characteristics of small $E_{\mathrm{T}}^{\mathrm{miss}}$ value and opposite-sign dilepton mass values

lower than Z boson mass. These two features are exploited to suppress the large WZ background in trilepton events. The event selection used for measurement of normalization of $Z\gamma^{(*)}$ conversion process can be summarized as follows.

- include exactly 3 leptons, 1e2μ or 3μ,
- include an opposite-sign muon pair with 12<M($\mu^+\mu^-$)<81.2 GeV,
- $|M(\mu^+\mu^-) - 91.2|$>10 GeV for the second $\mu^+\mu^-$ pair in 3μ events
- $|M(3\ell) - 91.2|$<10 GeV,
- E_T^{miss}<50 GeV.

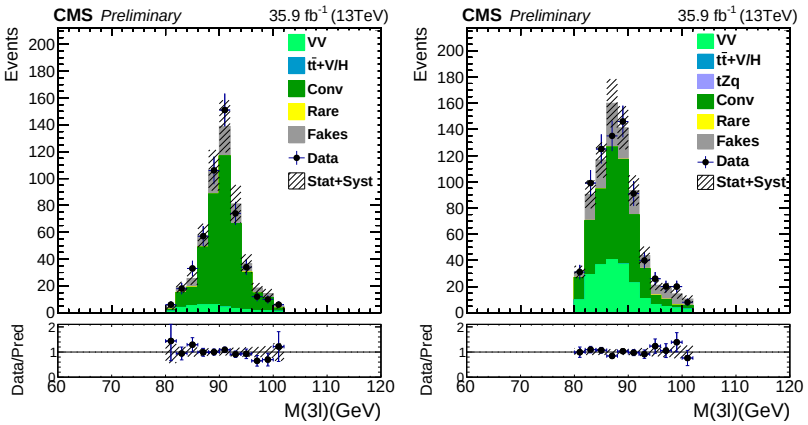

Figure 4.17: M(3ℓ) distributions of 1e2μ (left) and 3μ events (right), with the normalization corrections applied on the Zγ processes.

Due to different mechanisms of photon conversions, normalization is separately measured for 1e2μ and 3μ final states. Measured scale factors for the normalization of $Z\gamma^{(*)}$ process in each channel of 1e2μ and 3μ are,

$$SF = 0.96\pm0.09\ (1e2\mu\ \text{channel}), \quad SF = 0.84\pm0.12\ (3\mu\ \text{channel}). \qquad (4.17)$$

The uncertainty in scale factors is estimated from statistical uncertainty and propagation of all the systematic uncertainty described in the systematic uncertainty section.

4.6.3 Prompt Leptons

Prompt lepton backgrounds, or prompt processes, are processes that involve at least three charged leptons, electrons and muons, from decays of W, Z, and H bosons, including those from decays of tau leptons from the boson decays. Major contributions originate from $t\bar{t}$+V (V=W, Z), $t\bar{t}$+H, VV (WZ, ZZ) processes. Though the expected contribution is small, rare processes, such as the associated production of the Z boson and single top quark (t+Z), triboson processes (WWW, WWZ, WZZ, ZZZ), and the H boson production in the gluon fusion or vector boson fusion channels, are also included in the estimation. These contributions are estimated from simulation. Details regarding how these processes are modelled in the simulation are described in the Section 4.1.2.

4.6.4 Validation of Background Estimation

The validity of aforementioned background estimation methods are checked in two control event regions.

1. Region 1 - inclusive on-Z trilepton events (Fig. 4.18 and 4.19)

- include exactly 3 leptons, 1e2μ or 3μ, with an opposite-sign muon pair,
- for all opposite-sign muon pair, M($\mu\mu$)>12 GeV,
- at least one opposite-sign muon pair satisfies |M($\mu\mu$)-91.2|<10 GeV.

These events are enriched with WZ, ZZ, Z+j (fake), and small contribution from $Z\gamma^{(*)}$ conversions. The observed distributions are well described by estimation of the prompt, conversion, and jet-induced nonprompt lepton backgrounds.

2. Region 2 - same-sign dilepton events (Fig. 4.20 and 4.21)

- pass the same eμ or $\mu\mu$ triggers as in 1e2μ or 3μ channels of the analysis,
- exactly one same-sign eμ or $\mu\mu$ pair,
- $N_{\text{jets}} \geq 3$ and $N_{\text{b tags}} \geq 1$.

These events are enriched with semi-leptonic $t\bar{t}$ events, with one of the jets producing a mis-identified lepton, and a minor prompt lepton contribution originates from $t\bar{t}$+V/H, similarly as in the signal region. In eμ final states, charge-mismeasured dileptonic $t\bar{t}$ decays also yields significant event rates, and these are estimated with simulation. The observed data in this selection is well described by estimated background distributions.

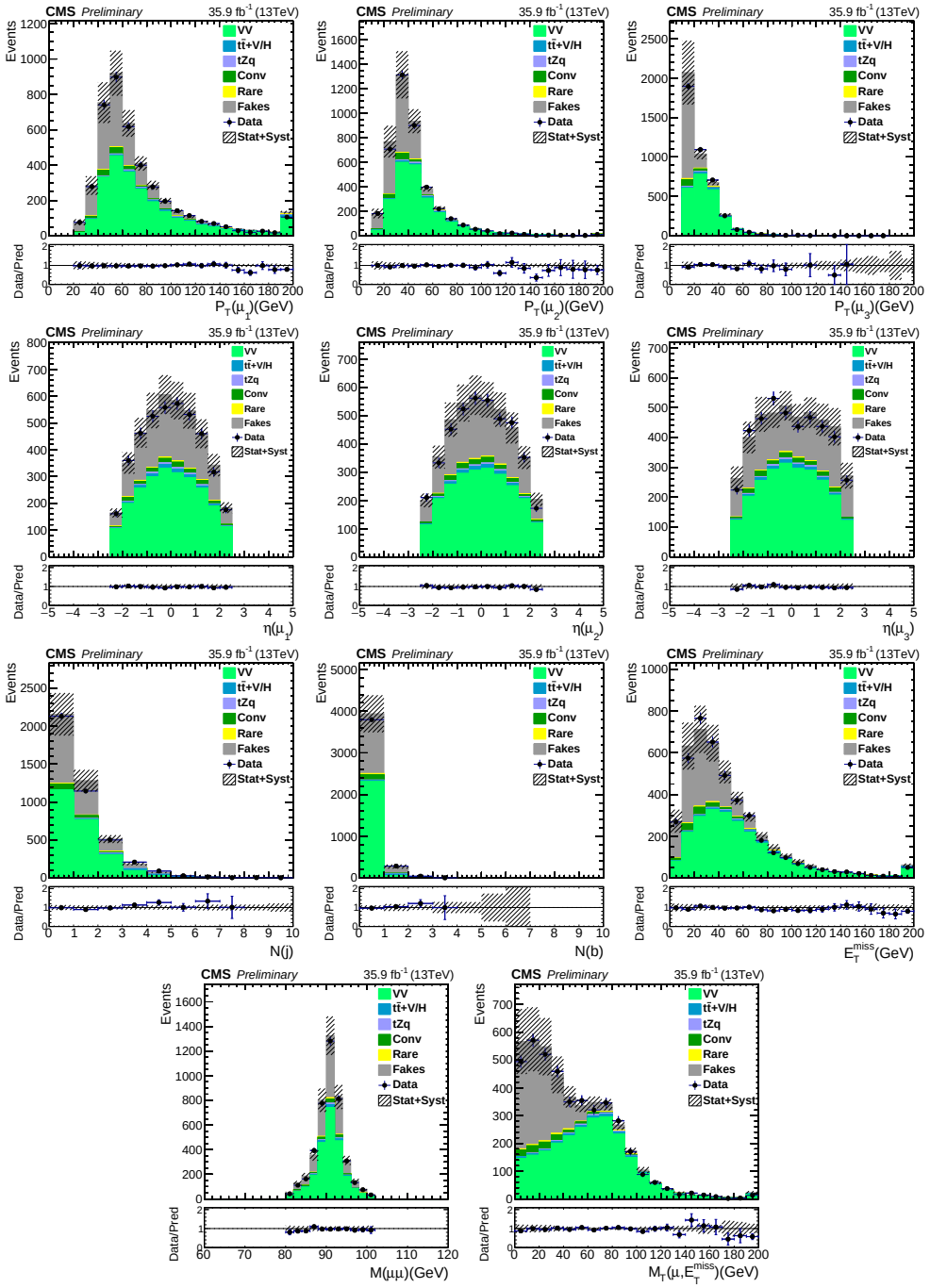

Figure 4.18: Kinematic distributions of physics objects in the inclusive on-Z trilepton event region (3μ).

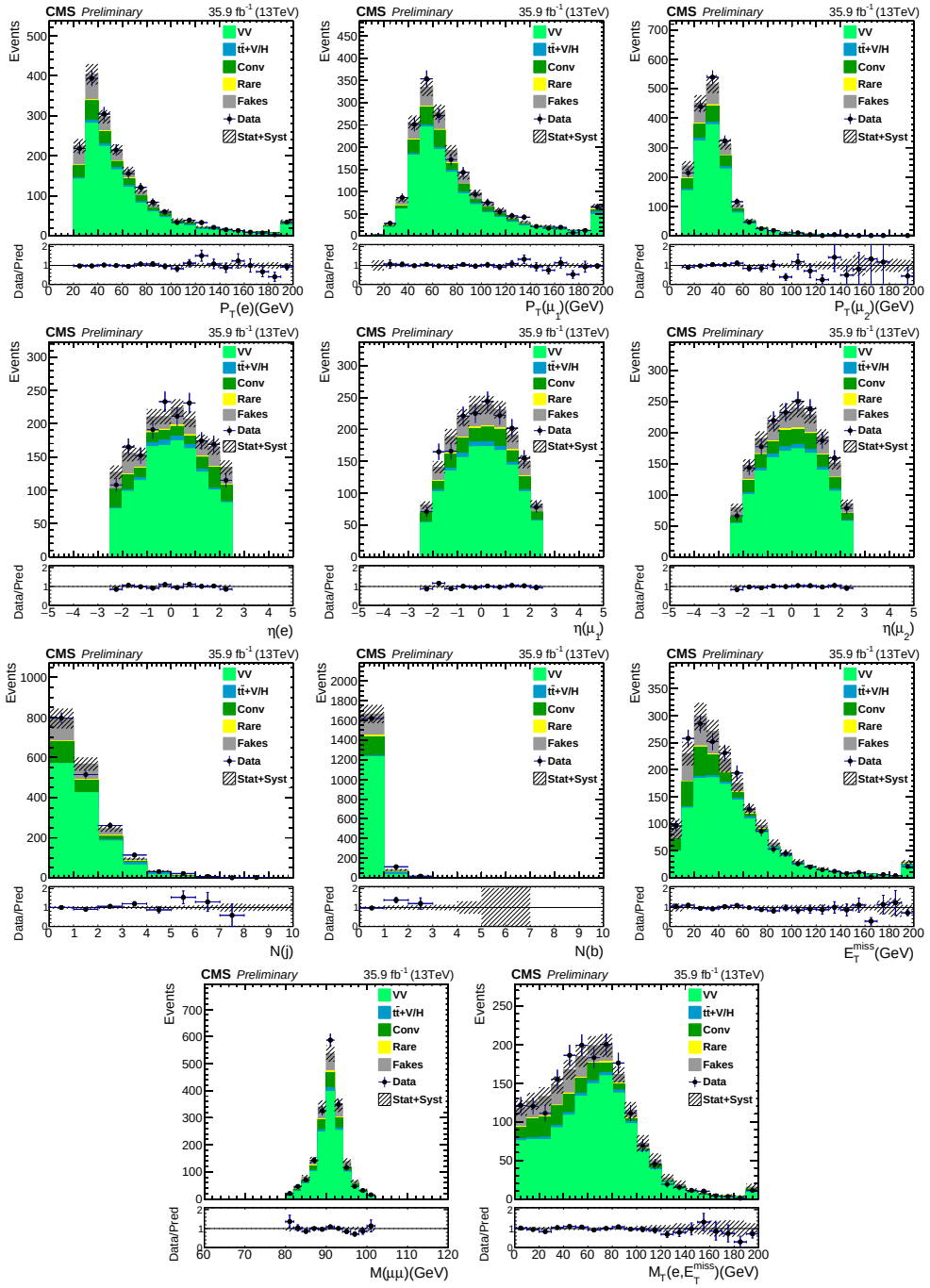

Figure 4.19: Kinematic distributions of physics objects in the inclusive on-Z trilepton event region (1e2μ).

Figure 4.20: Kinematic distributions of physics objects in the same-sign dilepton event region ($\mu\mu$).

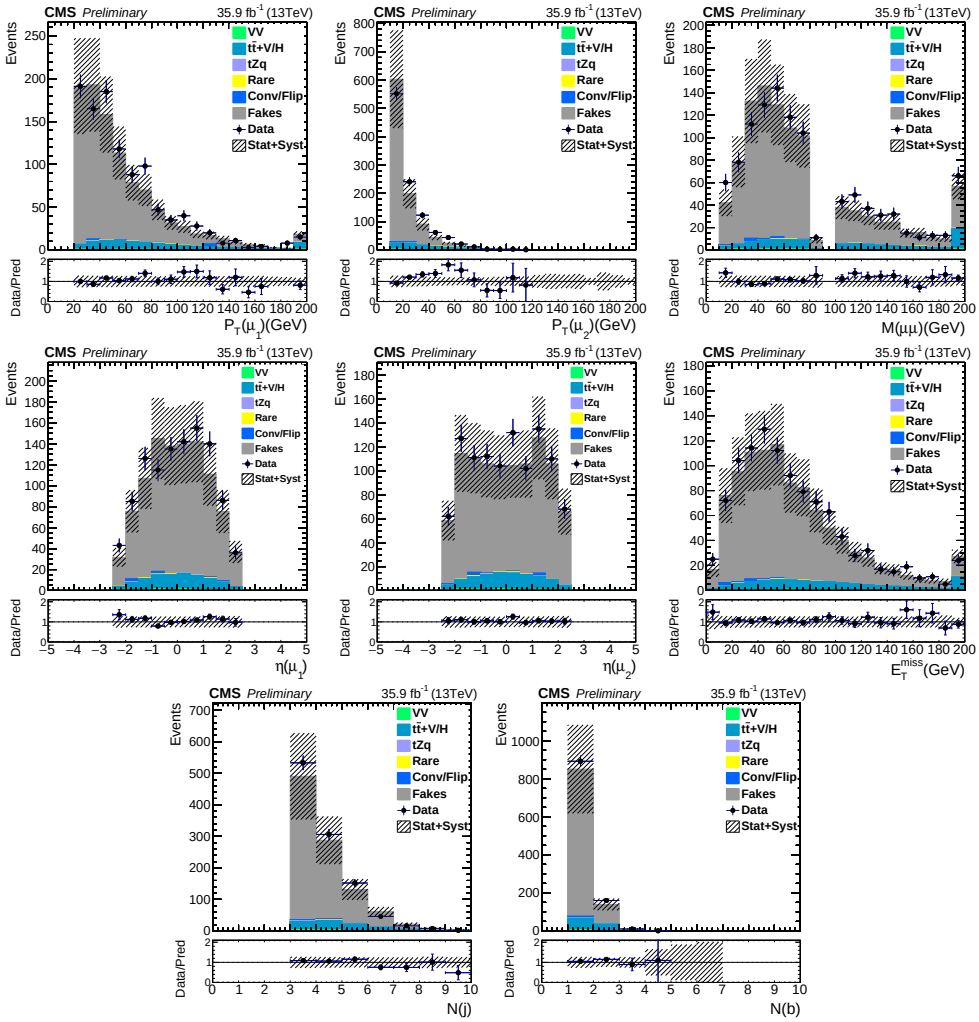

Figure 4.21: Kinematic distributions of physics objects in the same-sign dilepton event region (eμ).

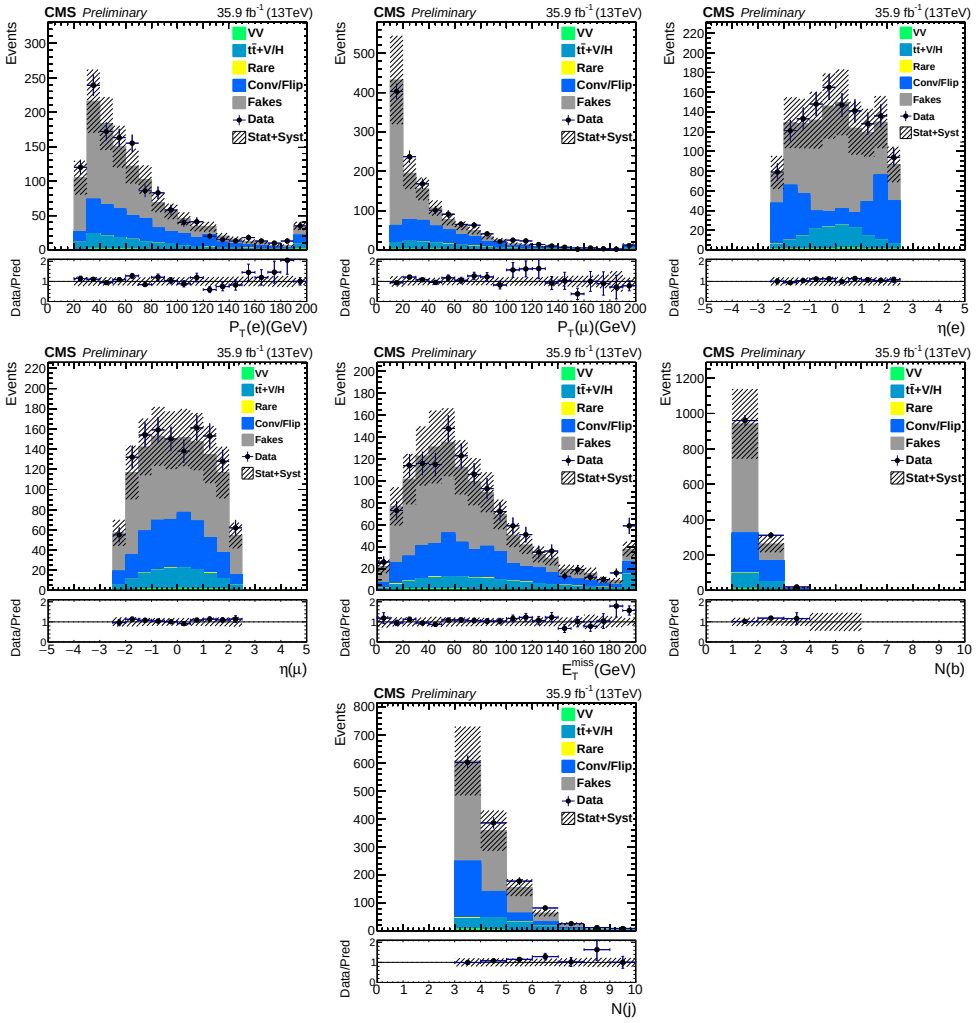

4.6.5 Linear Approximation of Background Distributions

Since the dimuon mass windows for the signal extraction are extremely narrow, background yields within the window acceptance are expected to be very small, less than a few events. The direct estimation using simulated samples passing the window acceptance suffers from a large statistical uncertainty. Alternatively, the background rates in the mass windows are estimated using the simulated or identification sideband samples within a extended dimuon mass range, i.e. inclusion of sidebands to the mass windows. The range of the mass sidebands are limited to be approximated as a linear function.

Technically, the background yield in a signal window (N_1) is obtained by scaling the expected yield in a larger concentric dimuon mass range with the ratio of widths of the signal window and the extended window ($N_2 \times w_1/w_2$), where N_i and w_i ($i = 1, 2$) are the event yields in the windows and the widths of the signal window (1) and the extended window (2). The method will be referred to as the scaling method or linear approximation of background in this analysis. It can be shown that the method is equivalent to a linear approximation of background events in the large window for slowly varying functions.

For a smoothly varying function $f(x)$, the area below the curve in the two symmetric range around a certain point, M_0, can be approximated from the series expansion of $f(\mathrm{M}_0 + \delta x)$,

$$
\begin{aligned}
N_2 &= \int_{-w_2}^{+w_2} f(\mathrm{M}_0 + \delta x) d\delta x \qquad (4.18)\\
&= \int_{-w_2}^{+w_2} [f(\mathrm{M}_0) + a_1 \delta x + a_2 \delta x^2 \ldots] d\delta x = f(\mathrm{M}_0) \cdot 2w_2 + O(\delta x^2)\\
N_1 &= \int_{-w_1}^{+w_1} f(\mathrm{M}_0 + \delta x) dx = f(\mathrm{M}_0) \cdot 2w_1 + O(\delta x^2) = N_2 \cdot \frac{w_1}{w_2} + O(\delta x^2).
\end{aligned}
$$

Hence, the first order approximation of the background produces the event

rate within the mass window proportional to its width. The half width of an extended window (w_2) is chosen to be 5 GeV, with exceptions of $|m_{\mathrm{A}}$-boundary$|$ values for the m_{A} values within 5 GeV from the boundary.

For the systematic uncertainty arising from the linear approximation, variation of expected yield is examined when the size of the extended window is changed by $\pm 20\%$. The approach and magnitudes of variations are motivated from the higher order terms in the approximation.

$$\Delta N = |N_1 - N_2 \cdot \frac{w_1}{w_2}| = \frac{2}{3}|a_2| w_1 (w_2^2 - w_1^2) + O(\delta x^4) \tag{4.19}$$
$$\frac{\Delta N}{N_2 \cdot \frac{w_1}{w_2}} = \frac{|a_2| w_2^2}{3a_0}(1 - (\frac{w_1}{w_2})^2) + O(\delta x^4) \approx \frac{|a_2| w_2^2}{3a_0} + O(\delta x^4)$$

The last approximation is based on the range of the squared fraction is small as 0.01–0.13 in current choice of bins. The difference between the variation of the extended window range by a factor of r becomes,

$$\frac{|a_2| w_2^2}{3a_0}((1+r)^2 - (1-r)^2) = \frac{|a_2| w_2^2}{3a_0} \cdot 4r \tag{4.20}$$

Hence variations of the size of the extended window by 20$\sim$30% is sufficient for estimation of the bias from the linear approximation.

In addition, the validity of this approach is cross-checked using simulated samples. In the simulated samples of major background processes, entire dimuon invariant mass distribution below Z boson mass is fitted using various analytic functions, and integration of these probability density functions within the signal windows are compared with the values obtained from the aforementioned linear approximation. The values from two approaches agreed within a few % of uncertainty, and this assures the validity of the approach and the extended window ranges.

4.7 Systematic Uncertainty

The systematic uncertainties of the analysis are categorized into the uncertainty related to data-driven methods, the limited size of the simulated or sideband samples, approximation methods, uncertainty related to correction factors on simulated samples, and the theoretical uncertainty in simulation. Those uncertainties are summarized in Table 4.16, and the impact on the signal strength is summarized in the Fig. 4.22.

4.7.1 Uncertainty Sources and Treatments

Uncertainty in Fake Rates

Systematic uncertainty of jet-induced nonprompt lepton estimation is assessed from two different approaches. The first method emulates the procedures of measurement and application using only simulated samples. In this study, fake rates are measured in simulated QCD multijet samples, with the selection requirements identical to those used for the measurement in real data, except the $p_{\mathrm{T}}^{\mathrm{miss}}$ and $\mathrm{M_T}(\ell, \vec{p}_{\mathrm{T}}^{\mathrm{miss}})$ cuts for suppression of the W boson background. These fake rates are applied to the $\mathrm{t\bar{t}}$ simulated sample, the major source of nonprompt leptons in the analysis. Overall event rates and dimuon mass distributions in the baseline selection are compared with estimation from the application region of simulated samples. This test attempts to assess the predictability with the fake rate measured in this method, and the impact of unknown systematic sources in fake rates. Agreement between the observed and expected yields in baseline selection, N_{obs}/N_{exp}, is 0.73±0.10 and 0.77±0.08 in 1e2μ and 3μ channels, respectively. The closure tests for dimuon mass distributions can be found in Appendix B, yet the jet and Z-veto requirements in the baseline selection is lifted in this case for the limited sample size.

The second method assesses the impact of variation of known systematic sources in the fake rate measurement in real data. Three categories of uncertainty is considered, which are uncertainty in the subtraction of prompt lepton backgrounds, dependence on the jet-flavor composition, and the energy scale of the ancestor jet. The first category is assessed by varying the normalization of simulated samples by 15%. Magnitude of the variation is determined from an envelope of variations of pile-up scenario, theoretical production cross sections, and energy scale of jets, leptons, and unclustered energy by their uncertainty, added in quadrature. The second category of uncertainty is assessed by inclusion of b-tagged jets in the event selection for the measurements. The third category of uncertainty is assessed by variation of the p_{T} thresholds for jets away from the lepton, $\Delta R(\ell, \mathrm{j})>1$. by $\pm 20\,\mathrm{GeV}$ for muons and -10/+20 GeV for electrons. The asymmetric cut for electron final states is due to the online jet-p_{T} selection. These uncertainty sources are combined by adding up in quadrature, and the result is shown in the error bars in Fig 4.16. Then these uncertainty is propagated to the estimated dimuon mass distributions in the baseline selection. The propagated variation has an impact of approximately 20% on the distributions in the baseline selection and enclosed within the flat error band of 30%.

Based on these two studies, a systematic uncertainty of 30% is assigned on the fake rates used for estimation of jet-induced nonprompt lepton backgrounds.

Uncertainty in Conversion Backgrounds

Among the conversion backgrounds, normalization of $\mathrm{Z}\gamma$ is constrained in the event selection enriched with $\mathrm{Z} \to \ell\ell\gamma$ events. Uncertainty in the scale factor for the normalization is estimated from propagation of uncertainty in

fake rates, common correction factors for the simulated samples, and the limited sample size. As a result, an uncertainty of 9.2% and 15% is assigned on the normalization of Zγ process in 1e2μ and 3μ channels, respectively.

Uncertainty from Limited Sample Size

Statistical uncertainty of simulated samples and application region samples for nonprompt lepton backgrounds is considered. The uncertainty is estimated by quadratic-summation of event weights for the both cases of data-driven and simulation-based estimations. The typical magnitudes of the uncertainty is approximately 7, 20, and 100% for prompt, nonprompt, and conversion lepton backgrounds, respectively, and it is about 1% for signal processes. The large magnitude of uncertainty for conversions barely has an impact on the final result due to its small contribution to the total background.

Uncertainty in Approximations

Systematic uncertainties associated with several approximation methods used for estimation of background yields and signal efficiencies are considered. For the linear approximation of background surrounding signal mass windows, the difference in estimation from the variation of widths of extended windows by $\pm$20% is assigned. The bias estimation is motivated from the higher order term in the series expansion of the probability density function. Typical magnitude of impacts on the event rates are 4, 10, and 50% for prompt, nonprompt, and conversion lepton backgrounds. Importance of the uncertainty is typically small due to presence of much larger uncertainty in the category, such as uncertainty in fake rates, or small contribution to the total background, in case of conversions.

For the interpolation of signal efficiency, a systematic uncertainty of 5% is assigned. The uncertainty is determined from the maximal difference between the two different values permitted in the interpolation method used. In addition, limiting to the mass window acceptance, the direct interpolation of signal efficiency is compared with integration of signal probability density function, modeled with parametric functions, and they agreed within an uncertainty of approximately 1%, well covered by the conservative uncertainty of 5%.

Uncertainty in Common Experimental Corrections in Simulation

This category of systematic uncertainty includes uncertainty associated to the integrated luminosity and experimental corrections applied in simulation. The uncertainty in the integrated luminosity is considered to be 2.5% [154]. The uncertainty is determined from dedicated study on sources affecting the measurement of fiducial total pp cross section during the vdM scan and those affecting the integration of bunch luminosity. The largest source of uncertainty in the vdM scan originate from the XY-correlation of a bunch shape and uncertainty in the length scale. For the integration of bunch luminosity, the uncertainty is mainly determined by difference in the luminosity values from different detector components.

Uncertainty in the total inelastic pp cross section used in the pile-up modeling is considered to be 4.6%. The magnitude of uncertainty is determined from the comparison of pile-up sensitive variables in real data and simulated samples, which include number of reconstructed primary vertices and mean pile-up p_{T} density. The impact of this uncertainty is assessed by reweighting to pile-up multiplicity distribution at varied cross section values.

For the lepton reconstruction and identification, the correction factors for

the difference in efficiency between the real data and simulation is obtained using the Z boson events and the tag-and-probe method. Uncertainty is mainly estimated based on the fit uncertainty in the extraction of the numbers. Because of the large Z boson production rate and its clear resonant shape, the uncertainty is typically quite small as 1%.

For the trigger efficiency, the correction factor is measured using either Z boson or $t\bar{t}$ events. The measurement based on Z boson events is approached with the same procedure as the correction factors for the lepton identification is applied. For the measurement based on $t\bar{t}$ events, it is assessed by variation of event selections used in the measurement and it is complemented by comparing with a study based on simulation. Because of the large Z and $t\bar{t}$ rate, and high purity of the sample, uncertainty in these correction factors are very small as 1% or less. Impact of event rate in the signal event region is assessed by propagation of variation of each filter efficiency combined in quadrature-summation.

Uncertainty in object momentum scale and resolution is considered by re-evaluating event rates with object momentum corrected by their uncertainty [146]. For the uncertainty in muon p_{T} scale and resolution, conservatively the whole amount of applied scale and resolution correction is taken as the uncertainty. For those of electron momentum, uncertainty of 0.6 and 1.5% is considered for the barrel and endcap regions. For the jet energy, the considered uncertainty is 3% or less for the scale and 5–20% for the resolution. Precision of unclustered energy, defined as energy of PF particles not categorized as leptons or constituents of jets, affects the calculation of $p_{\mathrm{T}}^{\mathrm{miss}}$, used in the muon assignment in the 3μ final state. It is estimated by simultaneous variation of unclustered particle energy by uncertainty values parameterized with particle type, p_{T}, and η. The uncertainty in the unclustered energy scale is considered only in the 3μ final state, it does not affect the $1\mathrm{e}2\mu$ channel.

Uncertainty in the b-tagging efficiency is assessed by re-evaluating correction factors with an efficiency changed by the uncertainty [145], and this procedure is separately performed for each jet flavor. Uncertainty in the b-jet tagging and c-jet mis-tagging efficiency is considered to be fully correlated, and the light jet mis-tagging efficiency is treated independently. Relative uncertainty in the b-tagging efficiency is as small as 1–1.5% for typical b jets from top quark decays and it is less than 5% in all kinematic ranges. Relative uncertainty in the mis-tagging efficiency of c or light jets are typically 10% for most kinematic regions.

Theoretical Uncertainty

Uncertainty in signal acceptance arising from uncertainty in Parton Distribution Function (PDF) is considered in the analysis. For the uncertainty arising from the PDF, the sample standard deviation of acceptances in 100 MC replicas of the PDF set is taken as the uncertainty arising from PDF. We also checked the sample standard deviation of acceptances in 4 different LO PDF sets (CT14llo, MMHT2014lo68cl, HERAPDF20_LO_EIG, NNPDF30_lo_as_0130), and the result was similar with estimation from MC replica set.

For the prompt lepton backgrounds, estimated with simulation, uncertainty in the theoretical production cross section is considered. The choice of renormalization and factorization scales, uncertainty in the PDF, and strong coupling constants are taken into account. The scales uncertainty is assessed by the envelope from variation of the two scales by a factor of 0.5 and 2, independently. The uncertainty in the PDF and strong coupling constants are in general treated with the approach in the Ref. [155]. The magnitude of scale uncertainty is usually asymmetric, and in such cases, conservatively a symmetric uncertainty with

a larger value is applied.

The uncertainty in the WZ production cross section at NLO QCD [156] is estimated to be +2.9/-3.8% and ±1.6% for scale and PDF+α_S uncertainty, respectively. For the ZZ cross section at NLO QCD [157], the estimated uncertainty values are +5.3/-7.7% and 2.2% for scale and PDF+α_S in ee$\mu\mu$ final state, and +4.3/-6.2% and 1.7% for scale and PDF+α_S in $\mu\mu\mu\mu$ final states. The total theoretical uncertainty combined by quadrature-summations are 4.1 and 8% for WZ and ZZ processes, respectively.

Theoretical uncertainty in $t\bar{t}$+X processes is also considered. The theoretical uncertainty in the $t\bar{t}Z$ production cross section is assessed to be +9.6/-11.3, ±2.8, and ±2.8% for the scale, PDF, and α_S uncertainty. For the $t\bar{t}W$ cross section, the theoretical uncertainty is estimated to be +12.9/-11.5, ±2.0, and ±2.7% for the scale, PDF, and α_S uncertainty. In case of the uncertainty in $t\bar{t}H$ production rate, uncertainty values of +5.7/-9.3 and 8.8% for the scale and PDF+α_S uncertainty. The total theoretical uncertainty obtained by quadrature-summations are 13.3, 12, and 12.8% for the $t\bar{t}W$, $t\bar{t}Z$, and $t\bar{t}H$ productions.

For the rare processes, conservatively 50% of uncertainty is assigned. Triboson, SM Higgs production from gluon fusion or vector boson fusion channels, tZ, and $t\bar{t}\gamma$ processes are considered as rare backgrounds.

4.7.2 Impact of Systematic Uncertainty

Typical impact of each uncertainty source is summarized in the Fig 4.22. As a representative point, signal hypothesis with m_{H^+} and m_A values of 160 and 45 GeV is chosen assuming a signal cross section of 1fb. The systematic uncertainty that has the largest impact on the result are the uncertainty in fake rates. Subleading source of uncertainty is the limited size of the application

Table 4.16: Summary of systematic uncertainty considered in the analysis.

Source	Process
integrated luminosity	prompt, signal
total inelastic pp cross section (pile-up modeling)	prompt, signal, conv.
muon identification efficiency	prompt, signal, conv.
electron identification efficiency	prompt, signal, conv.
trigger efficiency	prompt, signal, conv.
muon momentum scale and resolution	prompt, signal, conv.
electron energy scale	prompt, signal, conv.
electron energy resolution	prompt, signal, conv.
jet energy scale	prompt, signal, conv.
jet energy resolution	prompt, signal, conv.
b-tagging efficiency (b-jet)	prompt, signal, conv.
b-tagging efficiency (c/l-jet)	prompt, signal, conv.
unclustered energy scale	prompt, signal, conv. (3μ only)
fake rate	nonprompt
Zγ normalization	conv. (Zγ only)
linear approximation (bkgd.)	prompt, nonprompt, conv.
limited sample size	all processes
cross section (μ_F/μ_R, PDF, α_S)	prompt
PDF (acceptance)	signal
efficiency interpolation	signal

region sample for the estimation of jet-induced nonprompt lepton background. Impact from other uncertainty sources are in general much smaller than these uncertainty. As can be seen in the figure, the impact of these uncertainty in the signal strength is much smaller than its total uncertainty, because of the very small expected background rates. The impact of systematic uncertainty is generally minor in this analysis, when compared to the statistical uncertainty in observed data.

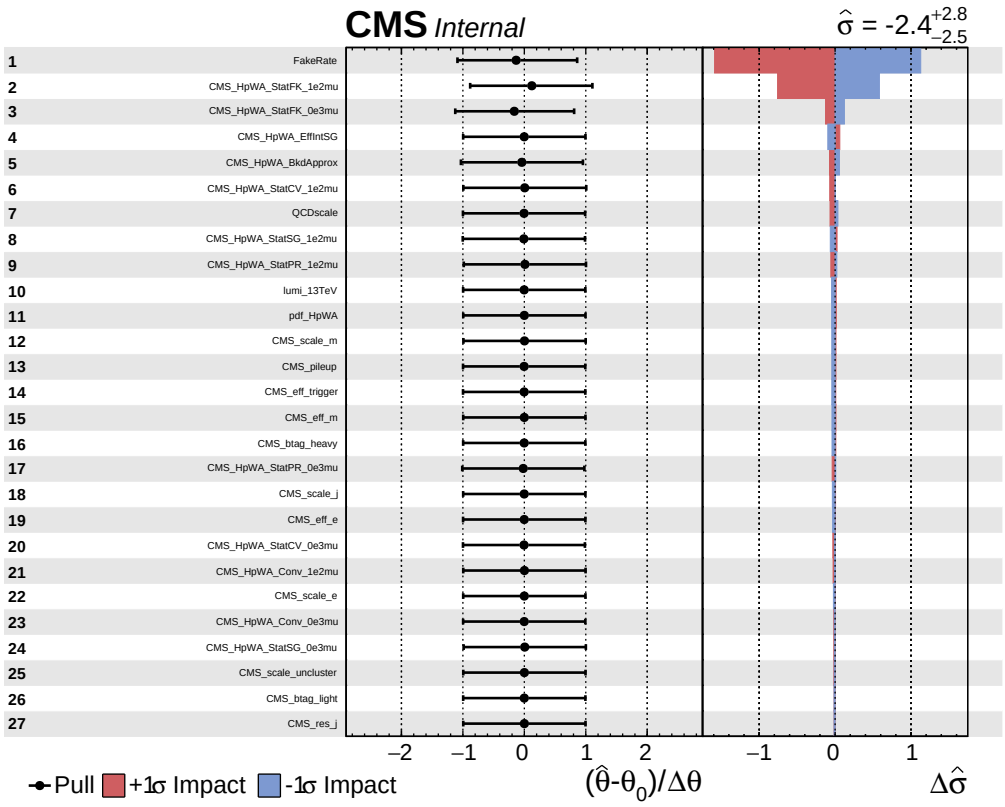

Figure 4.22: Impact of nuisance parameters on the signal strength. As a representative point, signal with m_{H^+} and m_{A} values of 160 and 45 GeV is chosen.

4.8 Result

4.8.1 Event Rates and Variable Distributions

Overall, 72 and 109 events are observed in the dimuon invariant mass range, [12, 80] GeV, with the baseline selection for 1e2μ and 3μ events, respectively. This is in good agreement with the expected number of background events, 78.3 ± 17.1 and 115.6 ± 27.0, in each final state, as shown in Table 4.17. The expected background rates are dominated by jet-induced nonprompt lepton backgrounds, and contributions from prompt and conversion lepton backgrounds are small. Approximately, 75 (70), 20 (20), and 5 (10)% of expected backgrounds in the 3μ (1e2μ) final state originate from jet-induced nonprompt, prompt, and conversion lepton backgrounds, respectively.

Table 4.17: Event yields in the dimuon invariant mass range, [12, 80] GeV, of the baseline signal selection.

	Expected Event Yields				Observed
	Nonprompt	Prompt	Conversion	Total Bkgd.	
1e2μ	54.4±16.9	17.0±1.3	6.9±2.6	78.3±17.1	72
3μ	87.5±26.9	22.0±1.8	6.1±2.3	115.6±27.0	109

The dimuon invariant mass distribution for the A boson candidates in the two final states is shown in Fig. 4.23. The distributions for individual final states can be found in the Appendix C. The scaling method is used in the background distributions to smear the statistical fluctuations. The distribution is observed to be well described by the expected background distributions, of which the rate in the dimuon mass spectrum is very low as approximately 1–4 events/GeV. With presence of a signal in the considered Higgs mass regions, an excess of event rates in a very narrow range is expected to be seen, as shown in the figure.

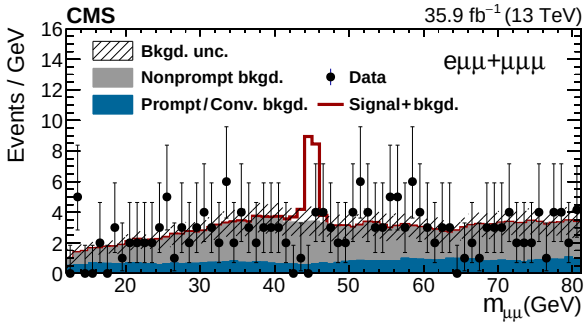

Figure 4.23: Dimuon invariant mass distributions for the A boson candidates in 1e2μ and 3μ final states. An expected signal distribution is overlaid on the background distribution, with assumptions of $m_{\mathrm{H}^+} = 130$, $m_{\mathrm{A}} = 45\,\mathrm{GeV}$, $\sigma(\mathrm{t\bar{t}}) = 832\,\mathrm{pb}$, and the signal decay rate, $\mathcal{B}_{\mathrm{sig}}$, of 6×10^{-6}.

The number of events in the mass windows used for the signal extraction are shown in Fig. 4.24 for each final state. Observed numbers of events vary in 0–8 and 0–9 for 1e2μ and 3μ events, respectively, and they are in good agreement with the expected background rates, as can be seen in the figure. Presence of a signal would lead to an excess in a few consecutive mass windows, partially overlapping near the m_{A} value, with a maximal magnitude at the window center closest to the m_{A} value.

4.8.2 Upper Limits on Signal Decay Rates

No statistically significant evidence of the signal is observed, hence upper limits are set on the signal rates. The limits are set at 95% CL using the CLs criterion, which is applied on a test statistic of the LHC experiments based on the profiled likelihood ratio. [158–160]. For a given signal strength r, defined as a scaling parameter of the signal event rate, and a set of nuisance parameters, θ, the likelihood function, L, is constructed as a product of a Poisson distribution

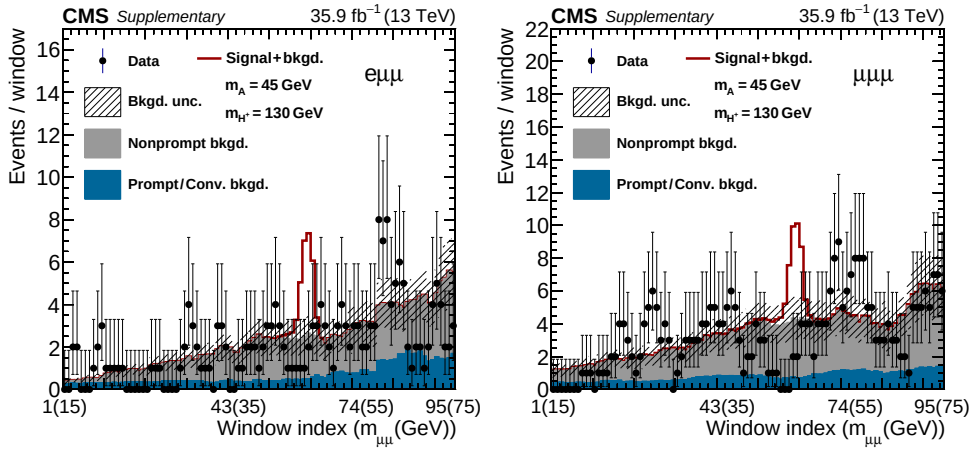

Figure 4.24: Number of events in dimuon mass bins used for the signal extraction. Expected signal distributions are overlaid on the background distributions, with the same assumptions as in the Fig. 4.23.

and a nuisance p.d.f., $\rho(\theta|\tilde{\theta})$,

$$L(data|r,\theta) = \left(\prod_i \frac{(rs_i + b_i)^{n_i}}{n_i!} e^{-rs_i - b_i}\right) \rho(\theta|\tilde{\theta}), \tag{4.21}$$

where i runs over different channels, n_i, s_i, and b_i are observed number of events, expected signal, and background rates in each channel. The nuisance p.d.f. is modeled as a log-normal distribution,

$$\rho(\theta|\tilde{\theta}) = \frac{1}{\sqrt{2\pi}\theta \ln(\kappa)} \exp\left(-\frac{(\ln(\theta/\tilde{\theta}))^2}{2(\ln\kappa)^2}\right). \tag{4.22}$$

Motivated by the asymptotic behavior of the log-normal distribution as the normal distribution, $N(\tilde{\theta}, (\kappa-1)^2)$, for κ values close to 1, the relative systematic uncertainty, ε, discussed in the previous section is incorporated into the likelihood as $\kappa = 1 + \varepsilon$. The choice of the log-normal distribution is motivated from its positive definite behavior, preventing a necessity for truncations in cases of non-negative variables such as efficiency and energy.

The test statistic, formulated in terms of these likelihoods, is defined as,

$$\tilde{q}_r = -2 \ln \frac{L(data|r, \hat{\theta}_r)}{L(data|\hat{r}, \hat{\theta})}, \quad 0 \leq \hat{r} \leq r, \tag{4.23}$$

where the $\hat{\theta}_r$ is the conditional maximum likelihood estimator of θ, for a given r value in signal+background hypothesis, and $\hat{r}$ and $\hat{\theta}$ are the global maximum likelihood estimators of r and θ. In addition, $\hat{\theta}_0$, the maximum likelihood estimator of θ in the background-only hypothesis is found. The values of these maximum likelihood estimators are obtained by fitting model to the observed data. From the determined model parameters, the p.d.f. for the test statistic is obtained by MC simulation in each of signal+background and background-only hypotheses, $f(\tilde{q}_r|r, \tilde{\theta}_r)$ and $f(\tilde{q}_r|0, \tilde{\theta}_0)$.

From the cumulative distribution of the two test statistic distributions from the pseudo-experiments, two p-values are determined,

$$p_r = P(\tilde{q} \geq \tilde{q}_r|\text{signal} + \text{bkgd.}), \quad 1 - p_b = P(\tilde{q} \geq \tilde{q}_r|\text{bkgd. only}). \tag{4.24}$$

From these p-values, the CLs criterion is calculated as, $\text{CL}_\text{s} = p_r/(1 - p_b)$. Exclusion at a $(1 - \alpha)$ confidence level with the CLs criterion refers to exclusion of parameter regions with $\text{CL}_\text{s} < \alpha$. The choice of a criterion in the LHC experiments is intended to avoid accidental exclusion of model parameters with weak signal strengths in case of downward statistical fluctuations. As the criterion is always larger than the p-value in the signal+background scenario, i.e. p_r, it is always more conservative than a test based solely on p_r.

The range of limit values expected in the background-only hypothesis is also calculated for comparison. For this purpose, a pseudo-data set is produced using MC simulation with the parameters in the background-only hypothesis. Then each of these pseudo-data is analyzed with the same method as the real

data, described previously. From the cumulative distribution of parameter values corresponding to $CL_s = \alpha$ in pseudo-events, the quantiles of the limit values are extracted. The median expected limit corresponds to the quantile of 50%, and ± 1 and 2 s.d. bands refer to the range of limit values in the quantile of 16–84 and 2.5–97.5%.

With the aforementioned approach, 95% CL upper limits on the signal decay rate, $\mathcal{B}_{\text{sig}} = \mathcal{B}(\text{t} \to \text{bH}^+)\mathcal{B}(\text{H}^+ \to \text{W}^+\text{A})\mathcal{B}(\text{A} \to \mu^+\mu^-)$, are calculated using the observed and expected number of events in dimuon mass windows of the two final states. The $\text{t}\bar{\text{t}}$ production cross section is assumed to be 831.76 pb, as mentioned in the section 4.1.2, and calculation is done for m_{A} values corresponding to window centers, defined in the Table 4.15. The resulting limit values for m_{H^+} values of $(m_{\text{A}} + 85)$ and 160 GeV are shown in Fig. 4.25. These m_{H^+} values correspond to the upper and lower boundaries of the considered m_{H^+} ranges, and the selection efficiency at these m_{H^+} values are close to the maximal and minimal values for a given m_{A} value. Hence, the limit values at these m_{H^+} values are approximately the largest and smallest values. As the difference between the limit values at those two m_{H^+} values is not large, when compared to the uncertainty bands in the figure, only the values at these two m_{H^+} values are shown in this section. The upper limits on the signal rates in other m_{H^+} values can be found in Appendix D.

For comparison, the limit values from individual final state are also shown in Fig. 4.26. As can be seen in the latter figure, the sensitivity to the signal is similar for both final states, hence inclusion of both final states in the combined likelihood significantly improves the limit values, as can be seen in Fig. 4.25.

The combined upper limits range between 1.9×10^{-6} and 8.6×10^{-6} in the entire mass region. These two values occur on m_{A} values of 44 and 19.05 GeV, and m_{H^+} values of 129 and 104.05 GeV, respectively. For the considered mass

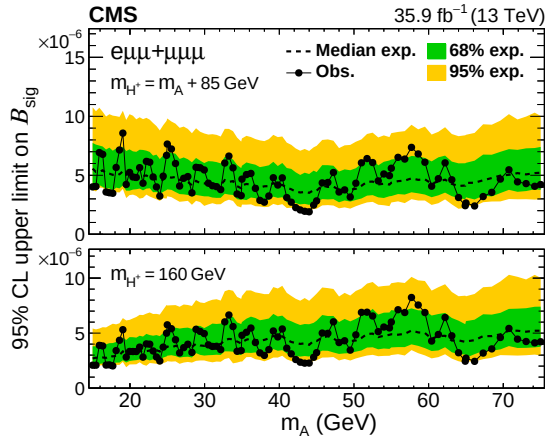

Figure 4.25: Upper limits at 95% CL on the $\mathcal{B}_{\text{sig}}$ for the m_{A} values in the Table 4.15 and m_{H^+} values of $(m_{\text{A}}+85)$ (top) and 160 GeV (bottom). Event yields in both final states are used in the calculation. Green and yellow bands respectively represents the range of upper limit values expected for the background-only hypothesis.

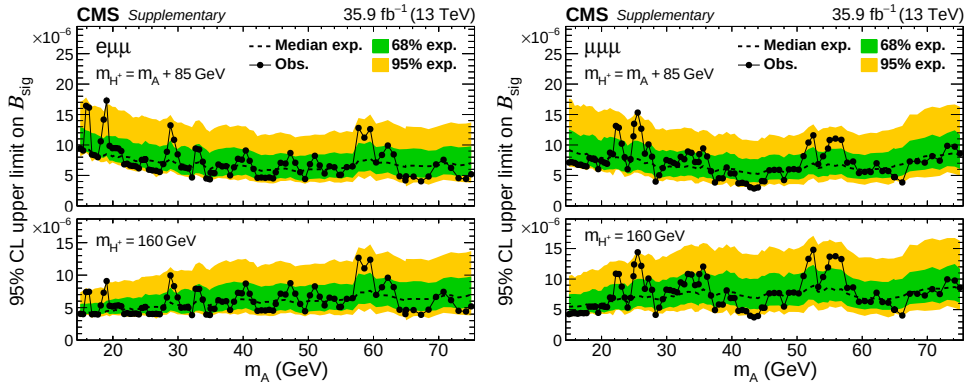

Figure 4.26: Upper limits at 95% CL on the $\mathcal{B}_{\text{sig}}$ for the m_{A} values in the Table 4.15 and m_{H^+} values of $(m_{\text{A}}+85)$ (top) and 160 GeV (bottom). Only the event yields in either 1e2μ (left) or 3μ (right) final states are used in the calculation. Definitions of green and yellow bands are the same with Fig. 4.25.

region, $m_{\mathrm{A}} \geq 15\,\mathrm{GeV}$ and $m_{\mathrm{A}} + 85 \leq m_{\mathrm{H^+}} \leq 160\,\mathrm{GeV}$, $\mathcal{B}_{\mathrm{sig}} > 8.6 \times 10^{-6}$ is excluded at 95% CL for all values of the two Higgs boson mass. These are the first upper limits on the combined branching fraction for the decay chain, $\mathrm{t} \to \mathrm{bH^+} \to \mathrm{bW^+A} \to \mathrm{bW^+}\mu^+\mu^-$.

As explained in the section 2.2.4 and Fig. 2.6, the branching fraction for the $\mathrm{A} \to \mu^+\mu^-$ decay is approximately 3×10^{-4} in type-1/2 2HDM and NMSSM, and 3.5×10^{-3} in type-X 2HDM, for moderate and large $\tan\beta$ values. For comparison with other experiments, these upper limits on $\mathcal{B}_{\mathrm{sig}}$ can be translated into upper limits $\mathcal{B}(\mathrm{t} \to \mathrm{bH^+})\mathcal{B}(\mathrm{H^+} \to \mathrm{W^+A}) \lesssim 2.9\%$ for type-1/2 2HDM and 0.25% for type-X 2HDM in the $\tan\beta$ region. This is approximately one order of magnitude more stringent than the results with the $\mathrm{A} \to \tau\tau$ decays from CDF Collaboration. In addition, the limit values are comparable to the upper limits on $\mathcal{B}(\mathrm{t} \to \mathrm{bH^+})\mathcal{B}(\mathrm{H^+} \to ff')$ for the fermionic $\mathrm{H^+}$ decay modes obtained in the LHC Run-1, introduced in the section 2.2.5.

Chapter 5

Conclusion

The standard model (SM) of particle physics has been immensely successful in description of most elementary particle phenomena. Nevertheless, there are still a few cosmological phenomena or experimental results in the precision frontier in conflict with the SM, suggesting the potential for extended particle spectra in the complete model. In this thesis, the possibility of an extended Higgs sector is explored.

As of now, the Higgs sector of observed particle spectra consists of single Higgs boson, discovered in the LHC Run-1, and its properties have been observed to be highly consistent with the SM prediction. Still, there are alternative scenarios with an extended Higgs sector consistent with the experimental results, such as the two-Higgs-doublet models (2HDM). The models can accommodate one of the Higgs bosons with a structure of couplings to fermions and gauge bosons identical to the SM. Investigation of such alternative models is important for deeper understanding of mass generating mechanisms and would strengthen the foundation of theories of Higgs bosons.

In the dissertation, the first search for the rare decay chain of a top quark, $t \to bH^+ \to bW^+A \to bW^+\mu^+\mu^-$, is discussed, where the H^+ and A are the charged and CP-odd neutral Higgs bosons. The mass of the two bosons are considered for m_A values between 15 and 75 GeV, and m_{H^+} values between $(m_A + 85)$ and 160 GeV. The search is based on data of proton-proton collisions at a center-of-mass energy of 13 TeV, recorded with the CMS detector at the CERN LHC in 2016. The integrated luminosity of data used in the analysis corresponds to $35.9\,\text{fb}^{-1}$. The top quark pair-production channel is considered for the source of top quarks, and 5.97×10^7 top quarks are expected to be produced in the period. Final states with three leptons, $e\mu\mu$ or $\mu\mu\mu$, and at least two jets, including a b-tagged jet, are analyzed. Presence of a signal is examined with analysis of event rates in the dimuon invariant mass distributions.

No statistically significant evidence of the top quark decay was observed, and the first upper limit was set on the product of branching fractions for the decay chain, $\mathcal{B}_{\text{sig}} = \mathcal{B}(t \to bH^+)\mathcal{B}(H^+ \to W^+A)\mathcal{B}(A \to \mu^+\mu^-)$, between 1.9×10^{-6} and 8.6×10^{-6} at the 95% CL, depending on the mass of the two Higgs bosons. In the parameter region of 2HDM with the unsuppressed branching fraction for the $A \to \mu^+\mu^-$ decay, these limits impose more stringent constraints on the decay, $t \to bH^+ \to bW^+A$, than the previous experiments, and comparable to those on $t \to bH^+ \to bff'$ for fermionic H^+ decays investigated in the LHC Run-1. The study presented in the thesis constitute the first search for the bosonic decay mode of the H^+ bosons using the subsequent $A \to \mu^+\mu^-$ decay.

Bibliography

1. ATLAS Collaboration. Observation of a new particle in the search for the Standard Model Higgs boson with the ATLAS detector at the LHC. *Phys. Lett. B* **716,** 1. arXiv: 1207.7214 [hep-ex] (2012).
2. CMS Collaboration. Observation of a new boson at a mass of 125 GeV with the CMS experiment at the LHC. *Phys. Lett. B* **716,** 30. arXiv: 1207.7235 [hep-ex] (2012).
3. CMS Collaboration. Observation of a new boson with mass near 125 GeV in pp collisions at $\sqrt{s} = 7$ and 8 TeV. *JHEP* **06,** 081. arXiv: 1303.4571 [hep-ex] (2013).
4. Sakharov, A. D. Violation of CP invariance, C asymmetry, and baryon asymmetry of the universe. *Soviet Physics Uspekhi* **34,** 392 (May 1991).
5. Davidson, S., Nardi, E. & Nir, Y. Leptogenesis. *Phys. Rept.* **466,** 105–177. arXiv: 0802.2962 [hep-ph] (2008).
6. Dolgov, A. Non-GUT baryogenesis. *Physics Reports* **222,** 309–386. ISSN: 0370-1573 (1992).
7. Zwicky, F. Die Rotverschiebung von extragalaktischen Nebeln. *Helvetica Physica Acta* **6,** 110–127 (Jan. 1933).
8. Massey, R., Kitching, T. & Richard, J. The dark matter of gravitational lensing. *Rept. Prog. Phys.* **73,** 086901. arXiv: 1001.1739 [astro-ph.CO] (2010).
9. Planck Collaboration. Planck 2018 results. VI. Cosmological parameters. *Astron. Astrophys.* **641.** [Erratum: Astron.Astrophys. 652, C4 (2021)], A6. arXiv: 1807.06209 [astro-ph.CO] (2020).

10. Muon g-2 Collaboration. Measurement of the Positive Muon Anomalous Magnetic Moment to 0.46 ppm. *Phys. Rev. Lett.* **126,** 141801. arXiv: 2104.03281 [hep-ex] (2021).

11. Dimopoulos, S. & Georgi, H. Softly Broken Supersymmetry and SU(5). *Nucl. Phys. B* **193,** 150–162 (1981).

12. Haber, H. E. & Kane, G. L. The search for supersymmetry: Probing physics beyond the standard model. *Phys. Rep.* **117,** 75 (1985).

13. Minkowski, P. $\mu \to e\gamma$ at a Rate of One Out of 10^9 Muon Decays? *Phys. Lett. B* **67,** 421–428 (1977).

14. Yanagida, T. Horizontal Symmetry and Masses of Neutrinos. *Prog. Theor. Phys.* **64,** 1103 (1980).

15. Schechter, J. & Valle, J. W. F. Neutrino Masses in SU(2) x U(1) Theories. *Phys. Rev. D* **22,** 2227 (1980).

16. Cheng, T. P. & Li, L.-F. Neutrino Masses, Mixings and Oscillations in SU(2) x U(1) Models of Electroweak Interactions. *Phys. Rev. D* **22,** 2860 (1980).

17. Gelmini, G. & Roncadelli, M. Left-handed neutrino mass scale and spontaneously broken lepton number. *Phys. Lett. B* **99,** 411 (1981).

18. Foot, R., Lew, H., He, X. G. & Joshi, G. C. Seesaw Neutrino Masses Induced by a Triplet of Leptons. *Z. Phys. C* **44,** 441 (1989).

19. Abada, A., Biggio, C., Bonnet, F., Gavela, M. B. & Hambye, T. $\mu \to e\gamma$ and $\tau \to \ell\gamma$ decays in the fermion triplet seesaw model. *Phys. Rev. D* **78,** 033007. arXiv: 0803.0481 [hep-ph] (2008).

20. Mohapatra, R. N. & Senjanovic, G. Neutrino Mass and Spontaneous Parity Nonconservation. *Phys. Rev. Lett.* **44,** 912 (1980).

21. CMS Collaboration. A portrait of the Higgs boson by the CMS experiment ten years after the discovery. *Nature* **607,** 60–68. arXiv: 2207.00043 [hep-ex] (2022).

22. CMS Collaboration. Combined measurements of Higgs boson couplings in proton–proton collisions at $\sqrt{s} = 13\,\text{TeV}$. *Eur. Phys. J. C* **79,** 421. arXiv: 1809.10733 [hep-ex] (2019).

23. Gonderinger, M., Lim, H. & Ramsey-Musolf, M. J. Complex Scalar Singlet Dark Matter: Vacuum Stability and Phenomenology. *Phys. Rev. D* **86,** 043511. arXiv: 1202.1316 [hep-ph] (2012).

24. Chakraborty, I. & Kundu, A. Controlling the fine-tuning problem with singlet scalar dark matter. *Phys. Rev. D* **87,** 055015. arXiv: 1212.0394 [hep-ph] (2013).

25. Turok, N. & Zadrozny, J. Electroweak baryogenesis in the two doublet model. *Nucl. Phys. B* **358,** 471–493 (1991).

26. Enomoto, K., Kanemura, S. & Mura, Y. Electroweak baryogenesis in aligned two Higgs doublet models. *JHEP* **01,** 104. arXiv: 2111.13079 [hep-ph] (2022).

27. Davidson, S. M. & Logan, H. E. Dirac neutrinos from a second Higgs doublet. *Phys. Rev. D* **80,** 095008. arXiv: 0906.3335 [hep-ph] (2009).

28. Ma, E. Verifiable radiative seesaw mechanism of neutrino mass and dark matter. *Phys. Rev. D* **73,** 077301. arXiv: hep-ph/0601225 (2006).

29. Cherchiglia, A., Stöckinger, D. & Stöckinger-Kim, H. Muon g-2 in the 2HDM: maximum results and detailed phenomenology. *Phys. Rev. D* **98,** 035001. arXiv: 1711.11567 [hep-ph] (2018).

30. Ellwanger, U., Hugonie, C. & Teixeira, A. M. The Next-to-Minimal Supersymmetric Standard Model. *Phys. Rept.* **496,** 1–77. arXiv: 0910.1785 [hep-ph] (2010).

31. Bento, M. P., Haber, H. E., Romão, J. C. & Silva, J. P. Multi-Higgs doublet models: physical parametrization, sum rules and unitarity bounds. *JHEP* **11,** 095. arXiv: 1708.09408 [hep-ph] (2017).

32. Aoki, M., Kanemura, S., Tsumura, K. & Yagyu, K. Models of Yukawa interaction in the two Higgs doublet model, and their collider phenomenology. *Phys. Rev. D* **80,** 015017. arXiv: 0902.4665 [hep-ph] (2009).

33. CMS Collaboration. Search for a charged Higgs boson in pp collisions at $\sqrt{s} = 8$ TeV. *JHEP* **11,** 018. arXiv: 1508.07774 [hep-ex] (2015).

34. CMS Collaboration. Search for a charged Higgs boson decaying to charm and bottom quarks in proton-proton collisions at $\sqrt{s} = 8$ TeV. *JHEP* **11,** 115. arXiv: 1808.06575 [hep-ex] (2018).

35. CMS Collaboration. Search for a light charged Higgs boson decaying to $c\bar{s}$ in pp collisions at $\sqrt{s} = 8$ TeV. *JHEP* **12,** 178. arXiv: 1510.04252 [hep-ex] (2015).

36. CMS Collaboration. Search for a light charged Higgs boson in the $H^{\pm} \to cs$ channel in proton-proton collisions at $\sqrt{s} = 13$ TeV. *Phys. Rev. D* **102,** 072001. arXiv: 2005.08900 [hep-ex] (2020).

37. CMS Collaboration. Search for charged Higgs bosons in the $H^{\pm} \to \tau^{\pm}\nu_{\tau}$ decay channel in proton-proton collisions at $\sqrt{s} = 13$ TeV. *JHEP* **07,** 142. arXiv: 1903.04560 [hep-ex] (2019).

38. CMS Collaboration. Search for charged Higgs bosons decaying into a top and a bottom quark in the all-jet final state of pp collisions at $\sqrt{s} = 13$ TeV. *JHEP* **07,** 126. arXiv: 2001.07763 [hep-ex] (2020).

39. ATLAS Collaboration. Search for charged Higgs bosons decaying via $H^{\pm} \to \tau^{\pm}\nu$ in fully hadronic final states using *pp* collision data at $\sqrt{s} = 8$ TeV with the ATLAS detector. *JHEP* **03,** 088. arXiv: 1412.6663 [hep-ex] (2015).

40. ATLAS Collaboration. Search for charged Higgs bosons in the $H^{\pm} \to tb$ decay channel in *pp* collisions at $\sqrt{s} = 8$ TeV using the ATLAS detector. *JHEP* **03,** 127. arXiv: 1512.03704 [hep-ex] (2016).

41. ATLAS Collaboration. Search for charged Higgs bosons decaying via $H^{\pm} \to \tau^{\pm}\nu_{\tau}$ in the τ+jets and τ+lepton final states with 36 fb^{-1} of *pp* collision data recorded at $\sqrt{s} = 13$ TeV with the ATLAS experiment. *JHEP* **09,** 139. arXiv: 1807.07915 [hep-ex] (2018).

42. ATLAS Collaboration. Search for charged Higgs bosons decaying into top and bottom quarks at $\sqrt{s} = 13$ TeV with the ATLAS detector. *JHEP* **11,** 085. arXiv: 1808.03599 [hep-ex] (2018).

43. Rathsman, J. & Rossler, T. Closing the Window on Light Charged Higgs Bosons in the NMSSM. *Adv. High Energy Phys.* **2012,** 853706. arXiv: 1206.1470 [hep-ph] (2012).

44. Dermisek, R., Lunghi, E. & Raval, A. Trilepton Signatures of Light Charged and CP-odd Higgs Bosons in Top Quark Decays. *JHEP* **04,** 063. arXiv: 1212.5021 [hep-ph] (2013).

45. Kling, F., Pyarelal, A. & Su, S. Light charged Higgs bosons to AW/HW via top decay. *JHEP* **11,** 051. arXiv: 1504.06624 [hep-ph] (2015).

46. Arhrib, A., Benbrik, R. & Moretti, S. Bosonic decays of charged Higgs bosons in a 2HDM type-I. *Eur. Phys. J. C* **77,** 621. arXiv: 1607.02402 [hep-ph] (2017).

47. CDF Collaboration. Search for a very light CP-odd Higgs boson in top quark decays from $p\bar{p}$ collisions at $\sqrt{s} = 1.96$ TeV. *Phys. Rev. Lett.* **107,** 031801. arXiv: 1104.5701 [hep-ex] (2011).

48. CDF Collaboration. Search for charged Higgs bosons from top quark decays in $p\bar{p}$ collisions at $\sqrt{s} = 1.96$ TeV. *Phys. Rev. Lett.* **96,** 042003. arXiv: hep-ex/0510065 [hep-ex] (2006).

49. DELPHI Collaboration. Search for charged Higgs bosons at LEP in general two Higgs doublet models. *Eur. Phys. J. C* **34,** 399–418. arXiv: hep-ex/0404012 (2004).

50. OPAL Collaboration. Search for charged Higgs bosons in e^+e^- collisions at $\sqrt{s}$ = 189–209 GeV. *Eur. Phys. J. C* **72,** 2076. arXiv: 0812.0267 [hep-ex] (2012).

51. ALEPH, DELPHI, L3, and OPAL Collaborations, and the LEP working group for Higgs boson searches. Search for charged Higgs bosons: combined results using LEP data. *Eur. Phys. J. C* **73,** 2463. arXiv: 1301.6065 [hep-ex] (2013).

52. Weinberg, S. A Model of Leptons. *Phys. Rev. Lett.* **19,** 1264–1266 (1967).

53. Glashow, S. L. Partial Symmetries of Weak Interactions. *Nucl. Phys.* **22,** 579–588 (1961).

54. Higgs, P. W. Broken Symmetries and the Masses of Gauge Bosons. *Phys. Rev. Lett.* **13** (ed Taylor, J. C.) 508–509 (1964).

55. Englert, F. & Brout, R. Broken Symmetry and the Mass of Gauge Vector Mesons. *Phys. Rev. Lett.* **13** (ed Taylor, J. C.) 321–323 (1964).

56. Particle Data Group. Review of Particle Physics. *Prog. Theor. Exp. Phys.* **2022,** 083C01 (2022).

57. Esteban, I., Gonzalez-Garcia, M. C., Maltoni, M., Schwetz, T. & Zhou, A. The fate of hints: updated global analysis of three-flavor neutrino oscillations. *JHEP* **09,** 178. arXiv: 2007.14792 [hep-ph] (2020).

58. Branco, G. C. *et al.* Theory and phenomenology of two-Higgs-doublet models. *Phys. Rept.* **516,** 1–102. arXiv: 1106.0034 [hep-ph] (2012).

59. Babu, K. S. & Jana, S. Enhanced Di-Higgs Production in the Two Higgs Doublet Model. *JHEP* **02,** 193. arXiv: 1812.11943 [hep-ph] (2019).

60. Nebot, M., Botella, F. J. & Branco, G. C. Vacuum Induced CP Violation Generating a Complex CKM Matrix with Controlled Scalar FCNC. *Eur. Phys. J. C* **79,** 711. arXiv: 1808.00493 [hep-ph] (2019).

61. Akeroyd, A. G., Arhrib, A. & Naimi, E.-M. Note on tree level unitarity in the general two Higgs doublet model. *Phys. Lett. B* **490,** 119–124. arXiv: hep-ph/0006035 (2000).

62. Haber, H. E. & Hempfling, R. The Renormalization group improved Higgs sector of the minimal supersymmetric model. *Phys. Rev. D* **48,** 4280–4309. arXiv: hep-ph/9307201 (1993).

63. Davidson, S. & Haber, H. E. Basis-independent methods for the two-Higgs-doublet model. *Phys. Rev. D* **72.** [Erratum: Phys.Rev.D 72, 099902 (2005)], 035004. arXiv: `hep-ph/0504050` (2005).

64. Moretti, S. Pair production of charged Higgs scalars from electroweak gauge boson fusion. *J. Phys. G* **28,** 2567–2582. arXiv: `hep-ph/0102116` (2002).

65. Aoki, M. *et al.* Light Charged Higgs bosons at the LHC in 2HDMs. *Phys. Rev. D* **84,** 055028. arXiv: `1104.3178 [hep-ph]` (2011).

66. Akeroyd, A. G., Moretti, S. & Hernandez-Sanchez, J. Light charged Higgs bosons decaying to charm and bottom quarks in models with two or more Higgs doublets. *Phys. Rev. D* **85,** 115002. arXiv: `1203.5769 [hep-ph]` (2012).

67. Eriksson, D., Rathsman, J. & Stal, O. 2HDMC: Two-Higgs-Doublet Model Calculator Physics and Manual. *Comput. Phys. Commun.* **181,** 189–205. arXiv: `0902.0851 [hep-ph]` (2010).

68. Spira, M., Djouadi, A., Graudenz, D. & Zerwas, P. M. Higgs boson production at the LHC. *Nucl. Phys. B* **453,** 17–82. arXiv: `hep-ph/9504378` (1995).

69. Braaten, E. & Leveille, J. P. Higgs Boson Decay and the Running Mass. *Phys. Rev. D* **22,** 715 (1980).

70. Drees, M. & Hikasa, K.-i. Note on QCD Corrections to Hadronic Higgs Decay. *Phys. Lett. B* **240.** [Erratum: Phys.Lett.B 262, 497 (1991)], 455 (1990).

71. Gorishnii, S. G., Kataev, A. L., Larin, S. A. & Surguladze, L. R. Corrected Three Loop QCD Correction to the Correlator of the Quark Scalar Currents and $\Gamma_{tot}(H^0 \to \text{Hadrons})$. *Mod. Phys. Lett. A* **5,** 2703–2712 (1990).

72. Deur, A., Brodsky, S. J. & de Teramond, G. F. The QCD Running Coupling. *Nucl. Phys.* **90,** 1. arXiv: `1604.08082 [hep-ph]` (2016).

73. Chetyrkin, K. G. Quark mass anomalous dimension to $O(\alpha_s^4)$. *Phys. Lett. B* **404,** 161–165. arXiv: `hep-ph/9703278` (1997).

74. Lee, T. D. A theory of spontaneous T violation. *Phys. Rev. D* **8,** 1226 (1973).

75. ALEPH Collaboration. Search for charged Higgs bosons in e^+e^- collisions at energies up to $\sqrt{s} = 209$-GeV. *Phys. Lett. B* **543,** 1–13. arXiv: `hep-ex/0207054` (2002).

76. DELPHI Collaboration. Search for charged Higgs bosons at LEP-2. *Phys. Lett. B* **460,** 484–497 (1999).

77. L3 Collaboration. Search for charged Higgs bosons at LEP. *Phys. Lett. B* **575,** 208–220. arXiv: `hep-ex/0309056` (2003).

78. OPAL Collaboration. Search for Charged Higgs Bosons in e^+e^- Collisions at $\sqrt{s} = 189 - 209$ GeV. *Eur. Phys. J. C* **72,** 2076. arXiv: `0812.0267 [hep-ex]` (2012).

79. OPAL Collaboration. Search for Higgs bosons in e^+e^- collisions at 183 GeV. *Eur. Phys. J. C* **7,** 407–435. arXiv: `hep-ex/9811025` (1999).

80. CDF Collaboration. Search for charged Higgs bosons in decays of top quarks in $p\bar{p}$ collisions at $\sqrt{s} = 1.96$ TeV. *Phys. Rev. Lett.* **103,** 101803. arXiv: `0907.1269 [hep-ex]` (2009).

81. D0 Collaboration. Search for charged Higgs bosons decaying to top and bottom quarks in $p\bar{p}$ collisions. *Phys. Rev. Lett.* **102,** 191802. arXiv: `0807.0859 [hep-ex]` (2009).

82. D0 Collaboration. Search for Charged Higgs Bosons in Top Quark Decays. *Phys. Lett. B* **682,** 278–286. arXiv: `0908.1811 [hep-ex]` (2009).

83. ATLAS Collaboration. Search for a multi-Higgs-boson cascade in $W^+W^-b\bar{b}$ events with the ATLAS detector in pp collisions at $\sqrt{s} = 8$ TeV. *Phys. Rev. D* **89,** 032002. arXiv: `1312.1956 [hep-ex]` (2014).

84. OPAL Collaboration. Two Higgs doublet model and model independent interpretation of neutral Higgs boson searches. *Eur. Phys. J. C* **18,** 425–445. arXiv: `hep-ex/0007040` (2001).

85. OPAL Collaboration. Flavor independent h^0A^0 search and two Higgs doublet model interpretation of neutral Higgs boson searches at LEP. *Eur. Phys. J. C* **40,** 317–332. arXiv: `hep-ex/0408097` (2005).

86. OPAL Collaboration. Search for neutral Higgs boson in CP-conserving and CP-violating MSSM scenarios. *Eur. Phys. J. C* **37,** 49–78. arXiv: `hep-ex/0406057` (2004).

87. CLEO Collaboration. Search for Very Light CP-Odd Higgs Boson in Radiative Decays of $\Upsilon(1S)$. *Phys. Rev. Lett.* **101,** 151802. arXiv: `0807.1427 [hep-ex]` (2008).

88. BaBar Collaboration. Search for Production of Invisible Final States in Single-Photon Decays of $\Upsilon(1S)$. *Phys. Rev. Lett.* **107,** 021804. arXiv: `1007.4646 [hep-ex]` (2011).

89. BaBar Collaboration. Search for hadronic decays of a light Higgs boson in the radiative decay $\Upsilon \to \gamma A^0$. *Phys. Rev. Lett.* **107,** 221803. arXiv: 1108.3549 [hep-ex] (2011).

90. BaBar Collaboration. Search for di-muon decays of a low-mass Higgs boson in radiative decays of the $\Upsilon(1S)$. *Phys. Rev. D* **87.** [Erratum: Phys.Rev.D 87, 059903 (2013)], 031102. arXiv: 1210.0287 [hep-ex] (2013).

91. BaBar Collaboration. Search for a low-mass scalar Higgs boson decaying to a tau pair in single-photon decays of $\Upsilon(1S)$. *Phys. Rev. D* **88,** 071102. arXiv: 1210.5669 [hep-ex] (2013).

92. BaBar Collaboration. Search for a light Higgs boson decaying to two gluons or $s\bar{s}$ in the radiative decays of $\Upsilon(1S)$. *Phys. Rev. D* **88,** 031701. arXiv: 1307.5306 [hep-ex] (2013).

93. Mangano, M. L. & Nason, P. Radiative quarkonium decays and the NMSSM Higgs interpretation of the hyperCP $\Sigma^+ \to p\mu^+\mu^-$ events. *Mod. Phys. Lett. A* **22,** 1373–1380. arXiv: 0704.1719 [hep-ph] (2007).

94. CMS Collaboration. Search for a Light Pseudoscalar Higgs Boson in the Dimuon Decay Channel in *pp* Collisions at $\sqrt{s} = 7$ TeV. *Phys. Rev. Lett.* **109,** 121801. arXiv: 1206.6326 [hep-ex] (2012).

95. CMS Collaboration. Search for a Low-Mass Pseudoscalar Higgs Boson Produced in Association with a $b\bar{b}$ Pair in *pp* Collisions at $\sqrt{s} = 8$ TeV. *Phys. Lett. B* **758,** 296–320. arXiv: 1511.03610 [hep-ex] (2016).

96. CMS Collaboration. Search for a light pseudoscalar Higgs boson produced in association with bottom quarks in pp collisions at $\sqrt{s} = 8$ TeV. *JHEP* **11,** 010. arXiv: 1707.07283 [hep-ex] (2017).

97. Spira, M. QCD effects in Higgs physics. *Fortsch. Phys.* **46,** 203–284. arXiv: hep-ph/9705337 (1998).

98. Larios, F., Tavares-Velasco, G. & Yuan, C. P. A Very light CP odd scalar in the two Higgs doublet model. *Phys. Rev. D* **64,** 055004. arXiv: hep-ph/0103292 (2001).

99. Gunion, J. F. & Haber, H. E. The CP conserving two Higgs doublet model: The Approach to the decoupling limit. *Phys. Rev. D* **67,** 075019. arXiv: hep-ph/0207010 (2003).

100. Ma, S., Wang, K. & Zhu, J. Higgs decay to light (pseudo)scalars in the semi-constrained NMSSM. *Chin. Phys. C* **45,** 023113. arXiv: 2006.03527 [hep-ph] (2021).

101. CMS Collaboration. Search for a very light NMSSM Higgs boson produced in decays of the 125 GeV scalar boson and decaying into τ leptons in pp collisions at $\sqrt{s} = 8$ TeV. *JHEP* **01,** 079. arXiv: 1510.06534 [hep-ex] (2016).

102. CMS Collaboration. A search for pair production of new light bosons decaying into muons. *Phys. Lett. B* **752,** 146–168. arXiv: 1506.00424 [hep-ex] (2016).

103. CMS Collaboration. Search for light bosons in decays of the 125 GeV Higgs boson in proton-proton collisions at $\sqrt{s} = 8$ TeV. *JHEP* **10,** 076. arXiv: 1701.02032 [hep-ex] (2017).

104. ATLAS Collaboration. Search for new phenomena in events with at least three photons collected in *pp* collisions at $\sqrt{s} = 8$ TeV with the ATLAS detector. *Eur. Phys. J. C* **76,** 210. arXiv: 1509.05051 [hep-ex] (2016).

105. ATLAS Collaboration. Search for Higgs bosons decaying to *aa* in the $\mu\mu\tau\tau$ final state in *pp* collisions at $\sqrt{s} = 8$ TeV with the ATLAS experiment. *Phys. Rev. D* **92,** 052002. arXiv: 1505.01609 [hep-ex] (2015).

106. LHC Design Report Vol.1: The LHC Main Ring (eds Bruning, O. S. *et al.*) (June 2004).

107. LHC Design Report. 3. The LHC injector chain (eds Benedikt, M., Collier, P., Mertens, V., Poole, J. & Schindl, K.) (Dec. 2004).

108. Evans, L. & Bryant, P. LHC Machine. *JINST* **3,** S08001 (2008).

109. CMS Collaboration. *CMS Luminosity - Public Results* https://twiki.cern.ch/twiki/bin/view/CMSPublic/LumiPublicResults. 2016.

110. CMS Collaboration. Cutaway diagrams of CMS detector (2019).

111. CMS Collaboration. Precise Mapping of the Magnetic Field in the CMS Barrel Yoke using Cosmic Rays. *JINST* **5,** T03021. arXiv: 0910.5530 [physics.ins-det] (2010).

112. CMS Collaboration. The CMS Experiment at the CERN LHC. *JINST* **3,** S08004 (2008).

113. The CMS hadron calorimeter project: Technical Design Report (1997).

114. CMS Collaboration. Performance of the CMS muon detector and muon reconstruction with proton-proton collisions at $\sqrt{s} = 13$ TeV. *JINST* **13,** P06015. arXiv: 1804.04528 [physics.ins-det] (2018).

115. Sauerburger, F. *LHC cross section plot* https://lhc-xsecs.org/. 2023.

116. CMS Collaboration. Performance of the CMS Level-1 trigger in proton-proton collisions at $\sqrt{s} = 13$ TeV. *JINST* **15,** P10017. arXiv: 2006.10165 [hep-ex] (2020).

117. CMS Collaboration. Precision luminosity measurement in proton-proton collisions at $\sqrt{s} = 13$ TeV in 2015 and 2016 at CMS. *Eur. Phys. J. C* **81,** 800. arXiv: 2104.01927 [hep-ex] (2021).

118. Van der Meer, S. *Calibration of the effective beam height in the ISR* tech. rep. (CERN, Geneva, 1968).

119. Rubbia, C. *Measurement of the luminosity of $p\bar{p}$ collider with a (generalized) Van der Meer Method* tech. rep. (CERN, Geneva, 1977).

120. Barschel, C. *et al.* Results of the LHC DCCT Calibration Studies (2012).

121. Belohrad, D., Jensen, L., Jones, O., Ludwig, M. & Savioz, J. *The LHC Fast BCT system: A comparison of Design Parameters with Initial Performance* tech. rep. (CERN, Geneva, 2010).

122. Nason, P. A new method for combining NLO QCD with shower Monte Carlo algorithms. *JHEP* **11,** 040 (2004).

123. Frixione, S., Nason, P. & Oleari, C. Matching NLO QCD computations with parton shower simulations: the POWHEG method. *JHEP* **11,** 070 (2007).

124. Alioli, S., Nason, P., Oleari, C. & Re, E. A general framework for implementing NLO calculations in shower Monte Carlo programs: the POWHEG BOX. *JHEP* **06,** 043 (2010).

125. Melia, T., Nason, P., Röntsch, R. & Zanderighi, G. W^+W^-, WZ and ZZ production in the POWHEG BOX. *JHEP* **11,** 078 (2011).

126. Grazzini, M., Kallweit, S., Rathlev, D. & Wiesemanna, M. $W^{\pm}Z$ production at hadron colliders in NNLO QCD. *Phys. Lett. B* **761,** 179 (2016).

127. Grazzini, M. *et al.* ZZ production at hadron colliders in NNLO QCD. *Phys. Lett. B* **735,** 311 (2014).

128. Alwall, J., Frederix, R., Frixione, S., *et al.* The automated computation of tree-level and next-to-leading order differential cross sections, and their matching to parton shower simulations. *JHEP* **07,** 079 (2014).

129. Mangano, M. L., Moretti, M., Piccinini, F. & Treccani, M. Matching matrix elements and shower evolution for top-pair production in hadronic collisions. *JHEP* **01,** 013 (2007).

130. Frederix, R. & Frixione, S. Merging meets matching in MC@NLO. *JHEP* **12,** 061 (2012).

131. Artoisenet, P., Frederix, R., Mattelaer, O. & Rietkerk, R. Automatic spin-entangled decays of heavy resonances in Monte Carlo simulations. *JHEP* **03,** 015 (2013).

132. Frixione, S., Laenen, E., Motylinski, P. & Webber, B. R. Angular correlations of lepton pairs from vector boson and top quark decays in Monte Carlo simulations. *JHEP* **04,** 081 (2007).

133. Yanyan, G. *et al.* Spin determination of single-produced resonances at hadron colliders. *Phys. Rev. D* **81,** 075022 (2010).

134. Particle Data Group. Review of Particle Physics. *Phys. Rev. D* **98,** 030001 (2018).

135. NNPDF Collaboration. Parton distributions for the LHC run 2. *JHEP* **04,** 040 (2015).

136. Sjöstrand, T. An introduction to PYTHIA 8.2. *Comput. Phys. Commun.* **191,** 159 (2015).

137. CMS Collaboration. Event generator tunes obtained from underlying event and multiparton scattering measurements. *Eur. Phys. J. C* **76,** 155. arXiv: 1512.00815 [hep-ex] (2016).

138. GEANT4 Collaboration. GEANT4: A Simulation toolkit. *Nucl. Instrum. Meth. A* **506,** 250 (2003).

139. CMS Collaboration. Description and performance of track and primary-vertex reconstruction with the CMS tracker. *JINST* **9,** P10009. arXiv: 1405.6569 [physics.ins-det] (2014).

140. Rose, K. Deterministic annealing for clustering, compression, classification, regression, and related optimization problems. *Proceedings of the IEEE* **86,** 2210–2239 (1998).

141. CMS Collaboration. Particle-flow reconstruction and global event description with the CMS detector. *JINST* **12,** P10003. arXiv: 1706.04965 [physics.ins-det] (2017).

142. Bethe, H. A. & Maximon, L. C. Theory of Bremsstrahlung and Pair Production. 1. Differential Cross Section. *Phys. Rev.* **93,** 768–784 (1954).

143. Cacciari, M., Salam, G. P. & Soyez, G. The anti-k_{T} jet clustering algorithm. *JHEP* **04,** 063. arXiv: 0802.1189 [hep-ph] (2008).

144. CMS Collaboration. Electron and photon reconstruction and identification with the CMS experiment at the CERN LHC. *JINST* **16,** P05014. arXiv: 2012.06888 [hep-ex] (2021).

145. CMS Collaboration. Identification of heavy-flavour jets with the CMS detector in pp collisions at 13 TeV. *JINST* **13,** P05011. arXiv: 1712.07158 [physics.ins-det] (2018).

146. CMS Collaboration. Performance of missing transverse momentum reconstruction in proton-proton collisions at $\sqrt{s} = 13$ TeV using the CMS detector. *JINST* **14,** P07004. arXiv: 1903.06078 [hep-ex] (2019).

147. CMS Collaboration. Identification of b-Quark Jets with the CMS Experiment. *JINST* **8,** P04013. arXiv: 1211.4462 [hep-ex] (2013).

148. Cowan, G., Cranmer, K., Gross, E. & Vitells, O. Asymptotic formulae for likelihood-based tests of new physics. *Eur. Phys. J. C* **71.** [Erratum: Eur. Phys. J. C 73 (2013) 2501], 1554. arXiv: 1007.1727 [physics.data-an] (2011).

149. Delaunay, B. Sur la sphère vide. *Bulletin de l'Académie des Sciences de l'URSS. Classe des sciences mathématiques et naturelles,* 793 (1934).

150. Shewchuk, J. R. Delaunay refinement algorithms for triangular mesh generation. *Computational Geometry* **22,** 21 (2002).

151. Shewchuk, J. R. in *Applied Computational Geometry: Towards Geometric Engineering* (eds Lin, M. C. & Manocha, D.) From the First ACM Workshop on Applied Computational Geometry, 203 (Springer-Verlag, May 1996).

152. CMS Collaboration. Search for new physics in same-sign dilepton events in proton–proton collisions at $\sqrt{s} = 13\,\text{TeV}$. *Eur. Phys. J. C* **76,** 439. arXiv: 1605.03171 [hep-ex] (2016).

153. Burkhardt, H., Kelner, S. R. & Kokoulin, R. P. Monte Carlo generator for muon pair production (May 2002).

154. CMS Collaboration. *CMS luminosity measurement for the 2016 data-taking period* CMS Physics Analysis Summary CMS-PAS-LUM-17-001 (2017).

155. Butterworth, J. *et al.* PDF4LHC recommendations for LHC Run II. *J. Phys. G* **43,** 023001. arXiv: 1510.03865 [hep-ph] (2016).

156. CMS Collaboration. Measurement of the WZ production cross section in pp collisions at $\sqrt{s} = 13$ TeV. *Phys. Lett. B* **766,** 268–290. arXiv: 1607.06943 [hep-ex] (2017).

157. CMS Collaboration. Measurement of the ZZ production cross section and $\text{Z} \to \ell^+\ell^-\ell'^+\ell'^-$ branching fraction in pp collisions at $\sqrt{s}$=13 TeV. *Phys. Lett. B* **763.** [Erratum: Phys.Lett.B 772, 884–884 (2017)], 280–303. arXiv: 1607.08834 [hep-ex] (2016).

158. Junk, T. Confidence level computation for combining searches with small statistics. *Nucl. Instrum. Meth. A* **434,** 435. arXiv: hep-ex/9902006 [hep-ex] (1999).

159. Read, A. L. Presentation of search results: the CL_s technique. *J. Phys. G* **28,** 2693 (2002).

160. ATLAS and CMS Collaborations & LHC Higgs Combination Group. *Procedure for the LHC Higgs boson search combination in summer 2011* tech. rep. CMS-NOTE-2011-005, ATL-PHYS-PUB-2011-11 (2011).

Appendix A

Acceptance Interpolation

In this appendix section, the validity of linear interpolation of mass window acceptance is discussed. For the purpose, the analytic shape of dimuon invariant mass of muon pairs from A decays are modeled in each simulation point. The parameters of the p.d.f. are fit to obtain those values at any mass values in between simulation points. The events used are required to pass the baseline signal selection of the search, except the Z-veto cut. The functional form of the resonance is considered to be the double-sided Crystal Ball function,

$$f(M; M_0, \sigma, a_1, n_1, a_2, n_2) = N \cdot \begin{cases} A_1(B_1 - \frac{M-M_0}{\sigma})^{-n_1} & \text{for } \frac{M-M_0}{\sigma} \leq -a_1 \\ \exp(-\frac{(M-M_0)^2}{2\sigma^2}) & \text{for } -a_1 < \frac{M-M_0}{\sigma} < a_2 \\ A_2(B_2 + \frac{M-M_0}{\sigma})^{-n_2} & \text{for } a_2 \leq \frac{M-M_0}{\sigma} \end{cases} \tag{A.1}$$

where $A_i = (\frac{n_i}{|a_i|})^{n_i}\exp(-\frac{a_i^2}{2}), \quad B_i = \frac{n_i}{|a_i|} - |a_i| \quad (i = 1, 2)$.

Binned maximum likelihood fit is performed in the range of $m_{\mathrm{A}} \pm 20\,\mathrm{GeV}$ to extract shape parameters. Then these parameters at simulation points are fitted to linear functions with smallest χ^2 values, shown in Fig. A.1. For the result, the signal p.d.fs are parameterized at an arbitrary m_{A} value.

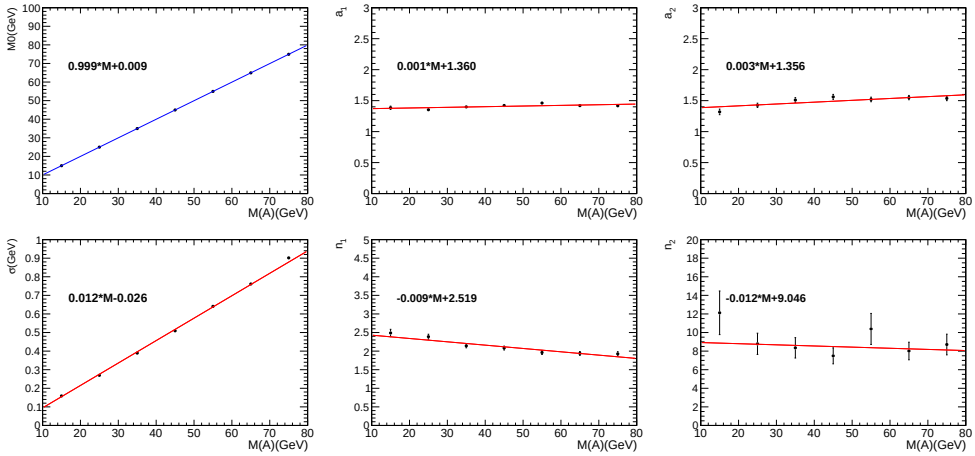

Figure A.1: Parameters of signal p.d.f. at simulated points (dots) and the fit functions for these (line).

As a closure test, χ^2/dof of this signal p.d.f. for dimuon mass distribution at each simulation points are checked, as examples shown in Fig. A.2. The χ^2/dof of p.d.f. with original fit function is overlaid in the figure for comparison. As can be seen in the figure, the shape parameters along the linear fit function produces p.d.f. very close to original p.d.f., from actual fitting of mass distribution, and well describes the dimuon mass distribution.

Then the mass window acceptance obtained by direct interpolation of acceptance values from nearby simulation points is compared with integration of signal p.d.f. within the mass windows. Those values from two approaches agreed within relative difference of 1%, as shown in Fig. A.3). This result verifies that

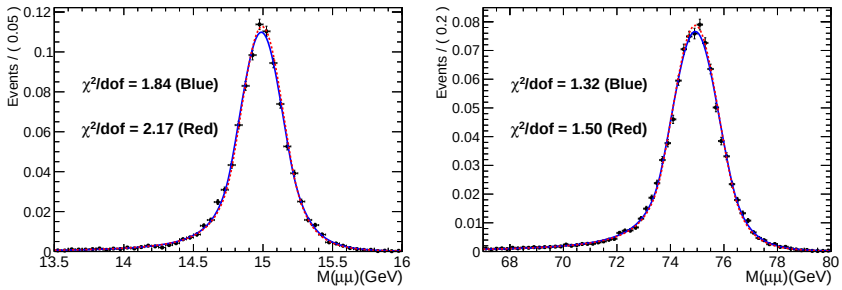

Figure A.2: Distribution of original fit function from fitting mass distribution (blue) and fitted parameters (red).

the mass window acceptance between simulation points varies slow enough to be estimated with a linear interpolation.

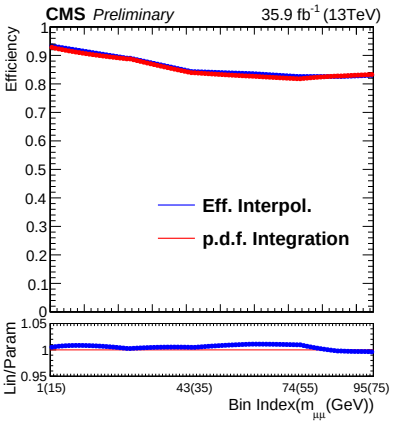

Figure A.3: Mass window acceptance calculated from linear interpolation from nearby simulation points and the integration of signal p.d.f..

Appendix B

Fake Rate: Closure Test

This appendix section includes supplemental materials for the Section 4.7.1. The $m_{\mu\mu}$ distributions of the simulated $t\bar{t}$ sample with the baseline signal selection are compared with those estimated from the application region of the same sample. For a limited sample size, the jet and Z veto cuts are not applied.

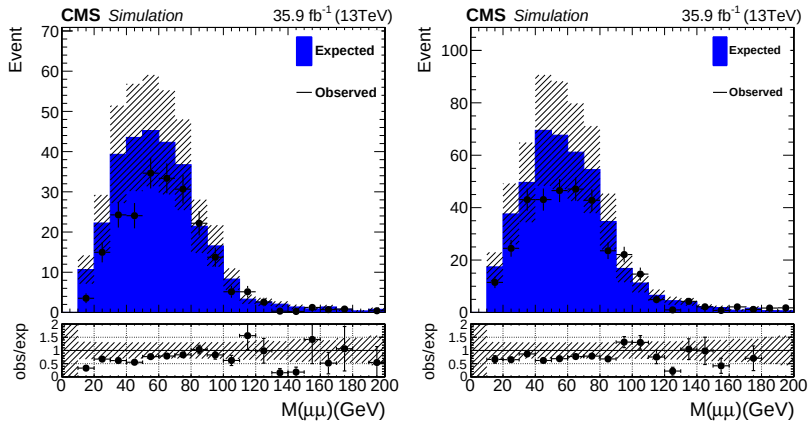

Figure B.1: Comparison of $m_{\mu\mu}$ distributions in $t\bar{t}$ simulated sample and the estimation with the fake rate method in 1e2μ (left) and 3μ (right) final states.

Appendix C

Dimuon Mass Distributions

This appendix section includes supplemental materials for the result section. The two figures in this section represent dimuon invariant mass distribution of each of 1e2μ and 3μ final states at the baseline signal selection of the search.

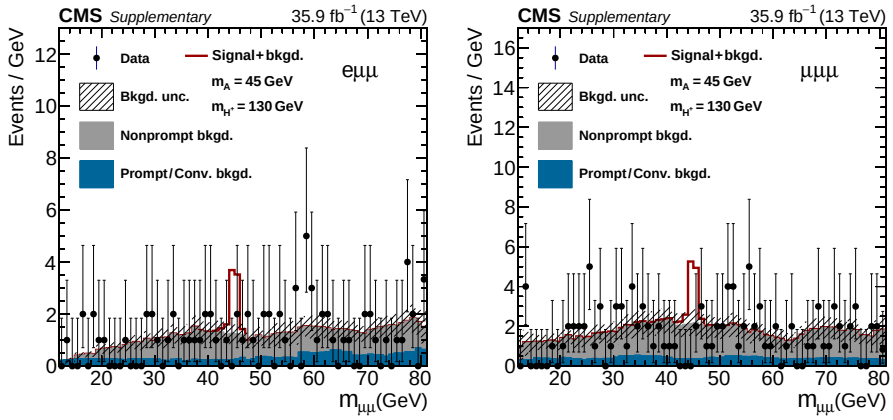

Figure C.1: Dimuon invariant mass distribution in the baseline signal selection of the search for 1e2μ (left) and 3μ (right) final states.

Appendix D

Upper Limits on Signal Rates

This appendix section consists of supplemental materials for the result section. The 95% CL upper limits on the signal cross section, defined in Section 4.1.2, are shown for all m_{H^+} values considered in the search.

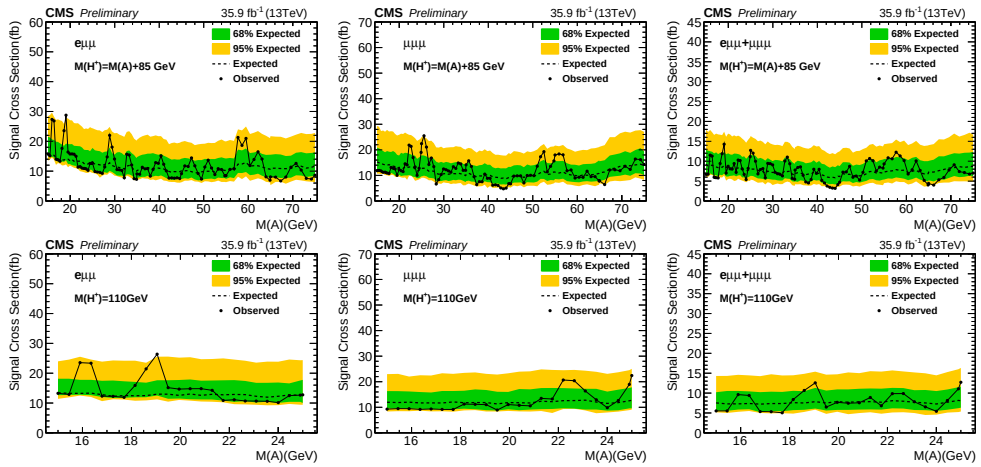

Figure D.1: 95% CL upper limits on the signal cross section for each m_{H^+} and m_{A} values from 1e2μ (left), 3μ (center), and both final states (right).

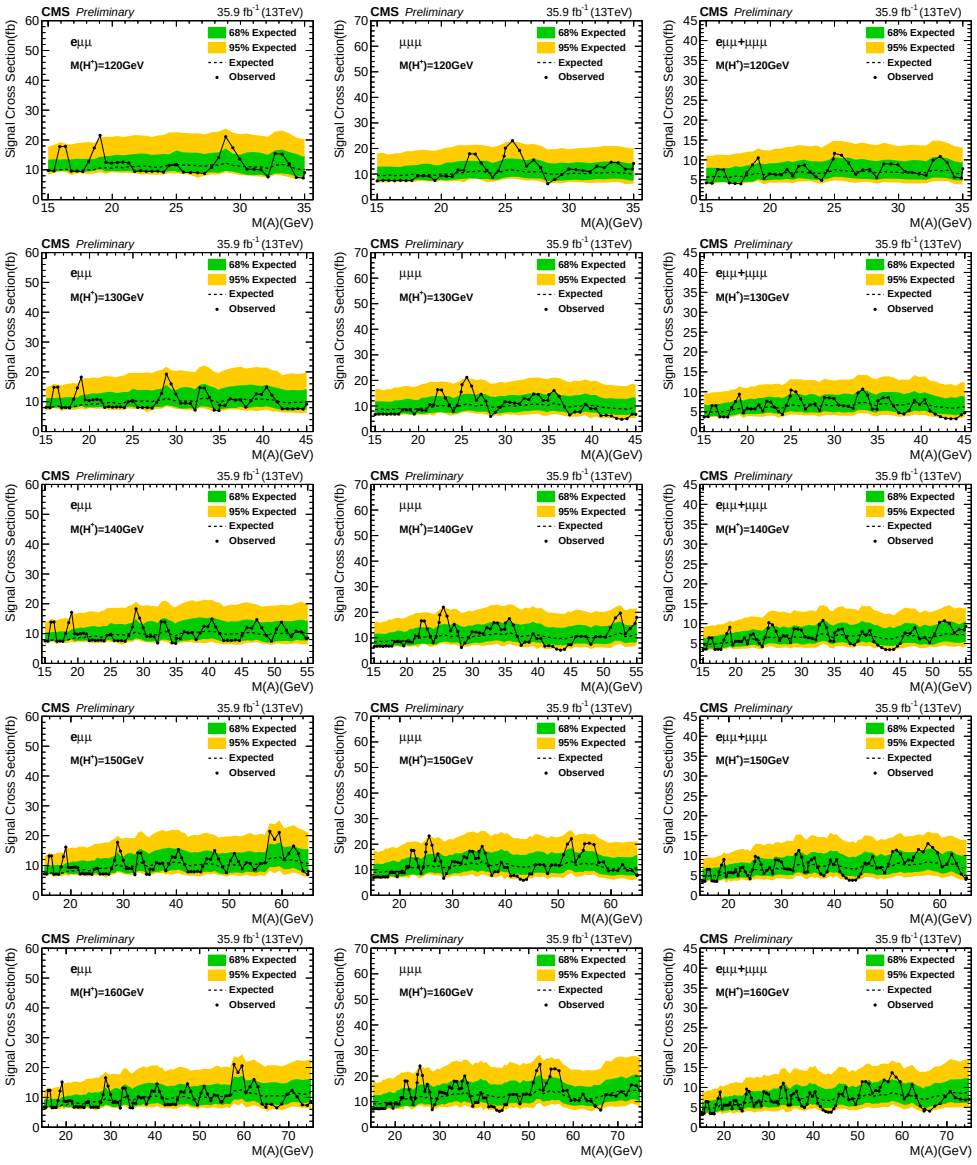

Figure D.2: 95% CL upper limits on the signal cross section for each m_{H^+} and m_{A} values from 1e2μ (left), 3μ (center), and both final states (right).

초록

이 논문은 탑 쿼크의 희귀 붕괴에서 유래하는 하전 힉스 보존 (H^+)에 대한 탐색 연구로 이루어져 있다. 이 분석은 2016년에 유럽 핵입자 물리 연구소 (CERN)의 대형 강입자 충돌기 (LHC) 내에 위치한 소형 뮤온 솔레노이드 (CMS) 검출기를 이용해 얻어진 질량중심 에너지 13 TeV 에서의 양성자-양성자 충돌 실험 결과를 바탕으로 얻어졌다. 사용된 데이터의 적분 광도는 $35.9\,\mathrm{fb}^{-1}$ 에 해당한다. LHC 에서 탑 쿼크의 주 생성 방식인 탑 쿼크 쌍생성 사건에서 생성되는 하전 힉스를 찾아서, 입자물리학의 표준모형에서 확장된 힉스 영역이 있는지 확인하고자 했다. 이 H^+ 보존은 상당한 붕괴율로 W와 CP-홀수 힉스 (A) 보존쌍으로 붕괴할 수 있으며, A 보존의 연쇄 붕괴 모드, $A \to \mu^+\mu^-$, 를 이용하여 이 H^+ 보존의 보존형 붕괴 모드의 유무를 조사하였다. 전자-두 뮤온 또는 세 뮤온, 그리고 b-표지 제트를 포함한 두 개 이상의 제트들이 있는 최종 상태들을 분석하여, A 보존 질량 15에서 75 GeV 사이와 H^+ 보존 질량 100에서 160 GeV 사이 영역에서 이 가설적 과정을 찾아보았다. 통계적으로 유의미한 추가적인 힉스 보존의 증거는 발견되지 않았으며, 이 연쇄 붕괴의 ($t \to bH^+ \to bW^+A \to bW^+\mu^+\mu^-$) 종합 붕괴율에 95% 신뢰수준의 상한을 최초로 1.9×10^{-6}와 8.6×10^{-6} 사이에서 세웠다.

주요어: 하전 힉스 보존, CP-홀수 힉스 보존, 탑 쿼크, CMS

학번: 2015-20329

Acknowledgements

The work in the thesis would not have been possible without so many people during the Ph.D period. I would like to express my gratitude in these pages.

Firstly, I would like to thank my supervisor Un-ki Yang. He has provided me an opportunity to work in the field of particle physics. In retrospect, the reason why I chose the area was curiosity about the fundamental structure underlying the world we are living in. A glimpse of the field from his introductory lectures on particle physics and the internship experience of the research project on the electron EDM at the ICL have strongly attracted my attention and made me eager to learn the knowledge. The life wasn't always easy in many ways, but I believe that the academic earnings were definitely worth for it. Still, I do not regret my decision in the slightest.

The next person I would like to appreciate is Dr. John L. Almond. He was practically the second advisor in my early years at the SNU CMS, especially while I studied the Higgs physics. Although he wasn't initially involved in the project and stayed on the opposite side of the earth most of the time, he was kind enough to reply to so many of my Skype messages and discuss all kinds of matters night and day. I am still very grateful to him for all the advice and discussions, from silly programming issues in the first year to academic writing

and peer-review procedures later on. Also I will miss the pints of beers we had together with Benjamin, Jaesung, and many other students.

I also want to thank my colleague Ph.D students. Jaesung Kim, my old friend who shared the same life trajectory with me for 14 years since the high school, helped me settle in the group and was the greatest partner in physics discussions for such a long time. The discussions often led to insights and solutions for difficulties I had, and fix flaws found in the analysis. Kyeongpil Lee, another old friend with incredible correlations with me, also helped me a lot, especially in the trigger issues, in which he was the expert. Hyunsan Seo, the magician of programming and server management, and a man of bright mind with personality of a living Buddha, always had solutions for any problems with grid computings. I am still amazed at how he could build up and manage a machine that can match a high-tier computing center from scratch by himself. I also appreciate his sharp comments and new ideas on my neutrino project.

I want to mention other current or former SNU CMS members as well, for any assistance, discussions, or the nice office atmosphere during the period. Kyungwook, a reincarnation of the Coca-Cola bear, Sungbin, a man of humor, football, and computer games, Joonbin, an artist, Sihyun, the 'Simpson', Jin, a gym-goer and machine teacher, Inseok, an athlete and tank-driver, and all the others, Benjamin, Byunghun, Won, Youngwan, two Junho's and Jihun's, Yeonjoon, Yeonjae, and Taehee - I will miss you all.

At last, but most importantly, I wish to thank my parents, Sang Yun Bhyun and Hee Kyung Do, who have been supporting me for all my life. Without their devotion, none of my career would have been accomplished. There will not be any words of gratitude that can be enough for them.